**DISSERTATION**

# DESIGN, FABRICATION, AND CHARACTERIZATION OF THREE-DIMENSIONAL CHIRAL PHOTONIC CRYSTALS

Zur Erlangung des akademischen Grades eines
DOKTORS DER NATURWISSENSCHAFTEN
von der Fakultät für Physik des
Karlsruher Instituts für Technologie (KIT)

genehmigte

DISSERTATION

von

Dipl.-Phys. Michael Thiel
aus Wadern

---

Tag der mündlichen Prüfung: 05.02.2010
Referent: Prof. Dr. Martin Wegener
Korreferent: Prof. Dr. Kurt Busch

# Publications

Parts of this thesis have already been published

**... in scientific journals:**

- G. von Freymann, A. Ledermann, M. Thiel, I. Staude, S. Essig, K. Busch, and M. Wegener, "*Three-Dimensional Nanostructures for Photonics*," Adv. Funct. Mater., accepted (2009).
- M. Thiel, H. Fischer, G. von Freymann, and M. Wegener, "*Three-dimensional chiral photonic superlattices*," Opt. Lett., accepted (2009).
- M. Thiel, M. S. Rill, G. von Freymann, and M. Wegener, "*Three-Dimensional Bi-Chiral Photonic Crystals*," Adv. Mater. **46**, 4680 (2009).
- M. Thiel, M. Wegener, and G. von Freymann, "*Three-dimensional chiral photonic crystals by direct laser writing*," Proc. SPIE **6883**, K8830 (2008).
- M. Thiel, M. Hermatschweiler, M. Wegener, and G. von Freymann, "*Thin-film polarizer based on a one-dimensional–three-dimensional–one-dimensional photonic crystal heterostructure*," Appl. Phys. Lett. **91**, 123515 (2007).
- M. Thiel, G. von Freymann, and M. Wegener, "*Layer-by-layer three-dimensional chiral photonic crystals*," Opt. Lett. **32**, 2547 (2007).
- M. Thiel, M. Decker, M. Deubel, M. Wegener, S. Linden, and G. von Freymann, "*Polarization Stop Bands in Chiral Polymeric Three-Dimensional Photonic Crystals*," Adv. Mater. **19**, 207 (2007).

**... in patents:**

- M. Thiel, G. von Freymann, and M. Wegener, "*Optical element, method for production thereof, and usage thereof*," WO 2008/049475 A1.

**... at conferences (only own presentations):**

- M. Thiel, G. von Freymann, and M. Wegener, "*Towards complete polarization band gaps in 3D chiral photonic crystals*," poster 107 (awarded, 1st RAITH poster prize), International Symposium on Photonic and Electromagnetic Crystal Structures (PECS-VIII), Sydney, Australia, April 5–9, 2009.

- M. Thiel, S. Wong, M. Wegener, and G. von Freymann, "*Layer-by-Layer Three-Dimensional Chiral Photonic Crystals*," talk CWO4, Conference on Lasers and Electro-Optics (CLEO), San Jose, USA, May 4–9, 2008.
- M. Thiel, G. von Freymann, and M. Wegener, "*Three-Dimensional Chiral Photonic Crystals*," **invited talk**, Progress In Electromagnetics Research Symposium (PIERS), Hangzhou, China, March 24–28, 2008.
- M. Thiel, S. Wong, M. Wegener, and G. von Freymann, "*Chiral 3D Photonic Crystals as Compact Optical Isolators*," talk CTuG7, Conference on Lasers and Electro-Optics (CLEO), Baltimore, USA, May 6–11, 2007.
- M. Thiel, M. Decker, M. Deubel, M. Wegener, S. Linden, and G. von Freymann, "*Strong Circular Dichroism from Chiral 3D Photonic Crystals*," poster B-60, International Symposium on Photonic and Electromagnetic Crystal Structures (PECS-VII), Monterey, USA, April 8–11, 2007.
- M. Thiel, M. Decker, M. Wegener, S. Linden, and G. von Freymann, "*Strong Circular Dichroism from Chiral 3D Photonic Crystals*," talk HL 18.6, Spring Meeting of the Deutsche Physikalische Gesellschaft, Regensburg, Germany, March 26–30, 2007.

Additional work on related topics has been published

**... in scientific journals:**

- I. Staude, M. Thiel, S. Essig, C. Wolff, K. Busch, G. von Freymann, and M. Wegener, "*Fabrication and characterization of silicon woodpile photonic crystals with a complete band gap at telecom-wavelenghts*," submitted (2009).
- J. K. Gansel, M. Thiel, M. S. Rill, M. Decker, K. Bade, V. Saile, G. von Freymann, S. Linden , and M. Wegener, "*Gold Helix Photonic Metamaterial as Broadband Circular Polarizer*," Science **325**, 1513 (2009).
- C. E. Kriegler, M. S. Rill, M. Thiel, E. Müller, S. Essig, A. Frölich, G. von Freymann, S. Linden, D. Gerthsen, H. Hahn, K. Busch, and M. Wegener, "*Transition between corrugated metal films and split-ring-resonator arrays*," Appl. Phys. B **96**, 749 (2009).
- M. S. Rill, C. E. Kriegler, M. Thiel, G. von Freymann, S. Linden, and M. Wegener, "*Negative-index bianisotropic photonic metamaterial fabricated by direct laser writing and silver shadow evaporation*," Opt. Lett. **34**, 19 (2009).
- S. Wong, O. Kiowski, M. Kappes, J. K. Lindner, N. Mandal, F. C. Peiris, G. A. Ozin, M. Thiel, M. Braun, M. Wegener, and G. von Freymann, "*Spatially Localized Photoluminescence at 1.5 Micrometers wavelength in Direct Laser Written Optical Nanostructures*," Adv. Mater. **20**, 4097 (2008).

- M. S. Rill, C. Plet, M. Thiel, I. Staude, G. von Freymann, S. Linden, and M. Wegener, "*Photonic metamaterials by direct laser writing and silver chemical vapour deposition*," Nature Mater. **7**, 543 (2008).
- S. Wong, M. Thiel, P. Brodersen, D. Fenske, G. A. Ozin, M. Wegener, and G. von Freymann, "*Highly Selective Wet Etch for High-Resolution Three-Dimensional Nanostructures in Arsenic Sulfide All-Inorganic Photoresist*," Chem. Mater. **19**, 4213 (2007).

# Contents

**Publications** i

**Deutschsprachige Zusammenfassung** vii

**1. Introduction** 1

**2. Fundamentals** 5
2.1. Chirality . . . 5
2.1.1. What is chirality? . . . 5
2.1.2. Brief history of chirality . . . 8
2.2. Polarization optics . . . 10
2.2.1. Eigenstates of polarization . . . 10
2.2.2. Basic interactions of polarized light with matter . . . 14
2.3. Photonic crystals . . . 20
2.3.1. Theoretical description . . . 20
2.3.2. Basic properties of photonic crystals . . . 23

**3. Photonic nanostructures with a twist** 31
3.1. Structural color in nature . . . 31
3.2. Blue phase of liquid crystals . . . 33
3.3. Artificial chiral materials . . . 35
3.3.1. Periodic nanostructures for photonics . . . 35
3.3.2. Fabrication methods . . . 38
3.3.3. Applications . . . 40

**4. Direct laser writing** 43
4.1. Concept of direct laser writing . . . 43
4.2. Advanced setup for three-dimensional laser lithography . . . 45
4.3. Photoresists and applications . . . 52

**5. Optical characterization and numerical calculations** 57
5.1. Polarization-resolved spectroscopy tools . . . 57
5.1.1. Setup for measurements in the near-infrared spectral range . . . 58
5.1.2. Setup for measurements in the mid-infrared spectral range . . . 59
5.2. Numerical methods . . . 60
5.2.1. Scattering-matrix approach . . . 60

**6. Uniaxial three-dimensional chiral photonic crystals** **69**
6.1. Layer-by-layer chiral photonic crystals . . . . . 69
6.2. Circular-spiral chiral photonic crystals . . . . . 78
6.3. Thin-film optical devices based on chiral photonic-crystal heterostructures 84
6.4. Three-dimensional chiral photonic superlattices . . . . . 89

**7. Triaxial three-dimensional chiral photonic crystals** **95**
7.1. Three-dimensional bi-chiral photonic crystals . . . . . 95

**8. Conclusions and outlook** **101**

**A. Chiral twist defect in layer-by-layer photonic crystals** **105**

**B. Supplementary data of chiral circular-spiral photonic crystals** **109**

**C. First studies of angle dependence of bi-chiral photonic crystals** **113**

**D. Reproducibility of the fabricated samples** **117**

**Bibliography** **121**

**Acknowledgments** **131**

# Deutschsprachige Zusammenfassung

*"Was kann wohl meiner Hand oder meinem Ohr ähnlicher, und in allen Stücken gleicher sein, als ihr Bild im Spiegel?"*

Immanuel Kant, 1783

Die Polarisation einer Lichtwelle ist eine ihrer grundlegendsten Eigenschaften. Dementsprechend werden viele Wechselwirkungen von Licht und Materie maßgeblich vom Verlauf des elektrischen Feldvektors bestimmt, welcher den Polarisationszustand einer elektromagnetischen Welle festlegt. Beispielsweise entdeckte Dominique François Jean Arago bereits 1811, dass sich die Polarisationsebene des Lichts bei der Propagation durch bestimmte Substanzen dreht. Im Jahre 1848 folgte Louis Pasteurs bahnbrechender Befund, dass diese optische Aktivität eine intrinsische Charakteristik jener Medien ist, die sich durch eine bestimmte Asymmetrie auszeichnen — Chiralität.

Das Wort *Chiralität* ist vom griechischen Wortstamm $\chi\epsilon\iota\rho\sim$ (*hand*$\sim$) abgeleitet und beschreibt Objekte, die nicht allein durch räumliche Drehung und Translation mit ihrem Spiegelbild (Enantiomer) zur Deckung gebracht werden können — also genau wie unsere beiden Hände. Bemerkenswerterweise formulierte der preußische Philosoph Immanuel Kant bereits vor über 200 Jahren diese Kernaussage über die Chiralität: "Und dennoch kann ich eine solche Hand, als im Spiegel gesehen wird, nicht an die Stelle ihres Urbildes setzen ..."

In unserer Natur ist die Chiralität allgegenwärtig. Die Händigkeit mancher chiraler Aromastoffe kann man sogar durch bloßes Riechen unterscheiden. Optische Materialien zeichnen sich hingegen dadurch aus, dass zirkular polarisierte Wellen unterschiedlich durch die links- und rechtshändige Variante der chiralen Elemente propagieren. Dies äußert sich insbesondere in optischer Aktivität und/oder zirkularem Dichroismus, d.h. unterschiedlichen Ausbreitungsgeschwindigkeiten und/oder Absorptionskoeffizienten für links- und rechtszirkulares Licht.

In der Optik und Photonik beschäftigt man sich in jüngster Zeit zunehmend mit der Frage, ob und wie man Chiralität auch mit maßgeschneiderten, künstlichen Nanostrukturen nachbilden kann. Besondere Beachtung wird natürlich denjenigen optischen Effekten geschenkt, die aufgrund des Drehsinns dieser Materialien entstehen. Durch gezielte Konstruktion zeigen diese Strukturen starke optische Effekte, die jene von natürlichen chiralen Materialien um viele Größenordnungen übersteigen können.

Diese Dissertation befasst sich mit der Rolle der *Chiralität* in einer besonderen Klasse optischer Materialien: Der Klasse der *Photonischen Kristalle*. Nanostrukturen werden als chirale Photonische Kristalle bezeichnet, wenn ihre periodisch angeordneten Bausteine eine helikale Windung in der Größenordnung der Lichtwellenlänge besitzen. Im Gegensatz dazu wird die optische Aktivität natürlich vorkommender chiraler Moleküle meist mit einer Wellenlänge aus dem sichtbaren Bereich des Spektrums untersucht, d.h. die schraubenartigen Moleküle sind viel kleiner als die Wellenlänge der interagierenden elektromagnetischen Welle.

Unsere Studien von künstlichen chiralen Kristallen erforderte (i) die Möglichkeit, Dielektrika in alle Raumrichtungen auf einer Sub-Mikrometerskala zu strukturieren. Weiterhin mussten (ii) die kleinen, dreidimensionalen chiralen Bausteine entworfen und (iii) mit geeigneten Simulationsprogrammen optimiert werden. Zum Vergleich mit den theoretischen Blaupausen benötigten wir im letzten Schritt (iv) umfassende Charakterisierungswerkzeuge für die hergestellten Strukturen.

Zur Herstellung (i) benutzten wir das Direkte Laserschreiben (DLW, Direct Laser Writing), welches die Fabrikation von beliebig geformten, dreidimensionalen Nanostrukturen mit Detailgrößen kleiner als 100 nm ermöglicht. Diese Technik hat sich mittlerweile als Standard der dreidimensionalen Mikrofabrikation für verschiedene Anwendungen durchgesetzt — von Nanostrukturen für die Photonik bis hin zu Matrizen für Zellwachstumsstudien. Im Großen und Ganzen kann man DLW als das dreidimensionale Analogon der planaren Elektronenstrahllithographie ansehen.

Im Rahmen dieser Promotion haben wir den DLW-Aufbau technisch und konzeptionell erheblich verbessert. In Kooperation mit der Carl Zeiss AG und der Nanoscribe GmbH ist dazu ein erweitertes, modernes DLW entworfen und experimentell umgesetzt worden. Ein kompakter frequenzverdoppelter Erbium-dotierter Faserlaser mit Impulsen von unter 150 fs Dauer ersetzt teure Titan:Saphir-Lasersysteme als stabile Laserquelle bei 780 nm Zentralwellenlänge. Die Laserleistung wird nun mit Hilfe eines akusto-optischen Modulators kontrolliert und kann automatisch geregelt werden. Der Laserstrahl wird über ein abschirmendes Rohrsystem in ein invertiertes Mikroskop eingekoppelt und fokussiert. Ein piezoelektrischer Tisch verschiebt die Probe präzise in alle Raumrichtungen, so dass das Beschreiben eines Photolacks mit beliebigen Trajektorien in einem Volumen von 300 µm×300 µm×300 µm möglich wird. Ein weiteres Novum ist die motorisierte Verschiebebühne, welche die Substrate lateral über eine Fläche von 10 cm×13 cm verfahren kann. Alle wesentlichen Komponenten können per Software adressiert werden.[1]

*Das* Schlüsselelement des neuen Systems ist der Autofokus: Die Grenzfläche zwischen dem Substrat und dem Photolack wird automatisch und reproduzierbar gefunden, so dass die Automatisierung und Effizienz des Aufbaus erheblich gesteigert wurde.

Als Photolack haben wir in unseren Experimenten stets den Negativlack *SU-8* verwendet, der sich durch relativ hohe Auflösung (Linienbreiten $< 150$ nm) und hohe optische

[1] Die Kontrollsoftware wurde von Dr. Georg von Freymann programmiert.

Transparenz im sichtbaren bis zum nahinfraroten Spektralbereich auszeichnet. Zudem führt die Belichtung nur zu einer sehr kleinen Brechzahländerung ($\Delta n < 10^{-3}$). Dieser letzte Aspekt ist wichtig, damit der Laserfokus an den Kreuzungspunkten mit bereits beschriebenen Bereichen nicht stark verzerrt wird.

Zur Untersuchung chiraler Photonischer Kristalle wurden im nächsten Schritt (ii) zwei unterschiedliche Bausteine entworfen: Chiral gestapelte Bauelemente (aufgebaut aus verdrehten Lagen paralleler Stäbe) und zirkular helikale Bauelemente (periodisch angeordnete Helices). Ein Kristall, der aus diesen Bausteinen besteht, kann die Propagation *einer* der beiden zirkularen Polarisationen in einem bestimmten Wellenlängenbereich sehr stark unterdrücken. Dieses sogenannte *Polarisationsstoppband* tritt gerade dann auf, wenn der helikale Baustein in der Größenordnung der Materienwellenlänge des Lichts liegt. Dabei reichen schon wenige Gitterperioden in Propagationsrichtung um die Lichtintensität um mehrere Größenordnungen abzuschwächen. Die zirkulare Polarisation mit einer zur Struktur identischen Händigkeit wird stark reflektiert, obgleich die gegensinnige Polarisation nahezu unbeeinflusst transmittiert wird. Theoretische Rechnungen haben gezeigt, dass man exzellente optische Eigenschaften selbst mit polymeren Strukturen mit kleinem Brechungsindex erhalten kann.

Die Tatsache, dass diese beiden chiralen Elemente selektiv auf *eine* zirkulare Polarisation antworten, ermöglichte es uns, diverse maßgeschneiderte chirale Photonische Kristalle zu konstruieren. Jedoch wurden die optischen Eigenschaften der Blaupausen noch vor dem Herstellungsprozess nummerisch analysiert und optimiert. Für diesen Schritt (iii) konnten wir auf den Streumatrix-Ansatz zur Berechnung von Transmissions- und Reflektionsspektren von endlichen, periodischen Nanostrukturen für die Photonik zurückgreifen.[2]

Mit Hilfe dieser Simulationstechnik verglichen wir die theoretischen Ergebnisse direkt mit den Transmissionsexperimenten. Wir haben dazu zwei Aufbauten zur polarisationsaufgelösten Spektroskopie vorgestellt: Jeweils einen für die Messungen im nahinfraroten und im mittleren infraroten Spektralbereich (Bandbreiten: 600–2200 nm und 2700–7000 nm). Die Charakterisierung der Proben (iv) wird durch elektronenmikroskopische Aufnahmen der hergestellten Strukturen ergänzt.

Die chiral gestapelten Photonischen Kristalle (Abbildung 0.1(a)) zeigten starken zirkularen Dichroismus im Bereich des Polarisationsstoppbandes, welches zentriert um die standardisierte Telekommunikationswellenlänge von 1,55 µm lag. Die theoretische Beschreibung dieser polymeren Kristalle orientiert sich an analytischen Modellen, die bereits für cholesterische Flüssigkristalle aufgestellt worden sind: Die Lagen des Stapels reflektieren je eine Partialwelle, die sich gemeinsam zu einer zirkular polarisierten, reflektierten Welle zusammensetzen. Sofern nun die einfallende Welle den gleichen Drehsinn wie die gestapelte Struktur besitzt, werden die Partialwellen phasengleich und mit zur einfallenden Welle identischer Händigkeit reflektiert. Bei gegensin-

[2] Die Originalversion der Simulationssoftware wurde von Dr. Stefan Linden programmiert.

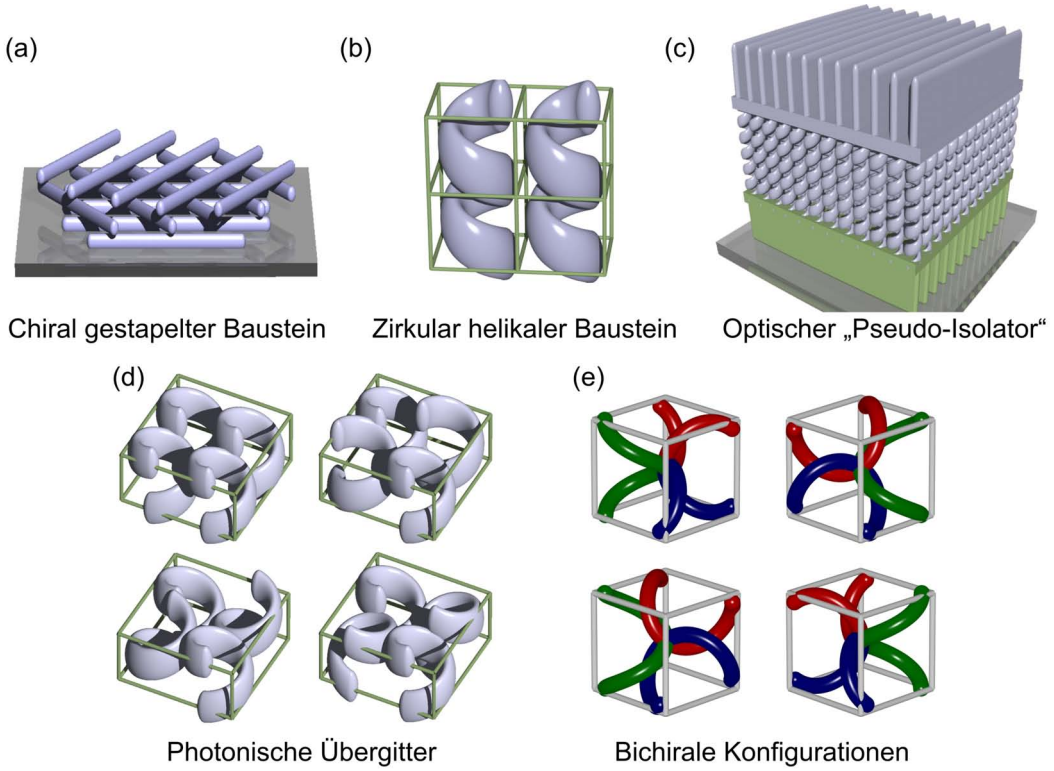


Abbildung 0.1: Leitfaden für die Ergebnisse. Die Abbildungen (a)–(e) zeigen Illustrationen aller chiralen Photonischen Kristalle, die in dieser Thesis untersucht wurden.

niger Händigkeit von Polarisation und Struktur ist die Interferenz der reflektierten Partialwellen destruktiv und das Licht wird transmittiert.

Der Dichroismus des zirkular helikalen Designs (Abbildung 0.1(b)) stellte bei einer Wellenlänge von 1,8 µm ein vergleichbares Ergebnis dar. Bei diesem Photonischen Kristall kann das Polarisationsstoppband intuitiv mit berechneten Feldverteilungen verstanden werden. Falls die einfallende zirkulare Polarisation und der Kristall die gleiche (ungleiche) Händigkeit besitzen, so werden die Lichtmoden stärker (schwächer) im Dielektikum eingeschlossen. Dies führt zu einem erhöhten effektiven Brechungsindex für den gleichsinnigen Fall und damit zu einer relativen spektralen Verschiebung der Reflektionsbänder, die für beide zirkularen Polarisationen im Photonischen Kristall auftreten. In beiden Fällen stimmte die Theorie bemerkenswert mit dem Experiment überein. Insbesondere wurde die relative Händigkeit zwischen Struktur und Licht, die spektrale Position des Stoppbandes und die Tiefe des Transmissionsminimums sehr gut reproduziert. Obwohl beide Ansätze ausgezeichnete experimentelle Ergebnisse erbracht haben, haben wir uns bei der Suche nach möglichen Anwendungen auf das zirkular helikale Bauelement konzentriert.

Eines der großen Ziele in der angewandten Nanophotonik ist es, funktionelle Strukturen für zukünftige Applikationen vorzustellen. Für chirale Photonische Kristalle sind bereits potenzielle Anwendungen entwickelt worden. Beispielsweise können sie als ultrakompakte Polarisationsfilter für zirkular polarisiertes Licht eingesetzt werden. Darüber hinaus funktionieren unsere chiralen Bauelemente in einer Heterostruktur mit zwei gekreuzten Viertelwellenplatten als Dünnfilmpolarisator für linear polarisiertes Licht (Abbildung 0.1(c) mit grüner Viertelwellenplatte). Asymmetrische Kombinationen mit nur einer Viertelwellenplatte auf einer Seite erlauben es uns, sie als linearen Polarisator oder auch als "Pseudo-Isolator" zu benutzen (abhängig von welcher Seite das Licht auf die Optik-Komponente fällt). Ein "Pseudo-Isolator" basiert auf der Umkehrung des Drehsinnes der zirkularen Polarisation bei Fresnel-Rückreflektion an einem Spiegel. Da chirale photonische Strukturen ihre Händigkeit jedoch nicht ändern (egal von welcher Seite man sie betrachtet), wird das Licht bei Rückreflektion geblockt. Die Bezeichnung "Pseudo-Isolator" rührt daher, dass die Optik nur für eine zirkulare Polarisation funktioniert. Dies steht im Gegensatz zu nicht-reziproken optischen Isolatoren, die z.B. auf dem Faraday-Effekt basieren. Die verwendeten Viertelwellenplatten wurden in den Experimenten durch eine einfache Anordnung von periodischen Lamellen realisiert, die zu Formdoppelbrechung im Limes langer Wellenlängen führt. Entsprechende polymere Heterostrukturen wurden hergestellt und ihre Funktionalität mit Transmissionsexperimenten untersucht.

Um ein tieferes Verständnis für den wichtigen zirkular helikalen Baustein zu erlangen, haben wir im Folgenden photonische Übergitter aus polymeren Helices in verschiedenen schachbrettartigen Anordnungen hergestellt (Abbildung 0.1(d)). Überraschenderweise fanden wir verschiedene neue dichroitische Resonanzen, die abhängig von der relativen Phasenverschiebung und Händigkeit der chiralen Elemente auftraten oder unterdrückt wurden. Unsere Experimente bestätigten, dass die chiralen optischen Eigenschaften stark von der lateralen Anordnung der Helices abhängen und nicht allein von den Helixparametern. Damit eröffnen sich neue Optionen, um die optischen Eigenschaften gezielt einzustellen. Darüber hinaus legen diese Beobachtungen die unterschiedlichen Mechanismen der helikalen Photonischen Kristalle im Vergleich mit den cholesterischen Flüssigkristallen dar.

Alle bisher vorgestellten Kristalle besitzen eine uniaxiale Symmetrie, d.h. nur *eine* helikale Achse. Vor diesem Hintergrund erweiterten wir die Dimensionalität unserer Strukturen und stellten eine neue Klasse Photonischer Kristalle vor. Bichirale Photonische Kristalle — die künstlichen, festen Äquivalente der "Blauphasen" in cholesterischen Flüssigkristallen — besitzen zwei Arten von Chiralität, woraus sich vier unterschiedliche Typen von bichiralen Strukturen ergeben (Abbildung 0.1(e)). Eine Händigkeit stammt von dem Motiv (den Helices in unserem Fall), die andere von dem fiktiven Skelett, auf dem das Motiv angeordnet ist. Das Konzept bichiraler dielektrischer Photonischer Kristalle mit kubischer Symmetrie umgeht die starke Richtungsabhändigkeit der uniaxialen Strukturen, während sie jedoch weiterhin starken zirkularen Dichroismus zeigen. Wir haben alle vier bichiralen Kombinationen hergestellt und mit entsprechenden Simulationen verglichen. Erwähnenswert ist hier-

bei die Tatsache, dass alle natürlich vorkommenden “Blauphasen” nur in zwei der vier möglichen Konfigurationen thermodynamisch stabil sind. In unseren Experimenten zeigten gerade die Kombinationen, die nicht in der Natur vorkommen, die stärksten Effekte.

Zusammenfassend haben wir eine faszinierende Klasse von photonischen Nanostrukturen untersucht: Chirale dreidimensionale Photonische Kristalle. Wir konnten mehrere Entwürfe solcher Kristalle mittels DLW herstellen und theoretisch sowie experimentell charakterisieren. Diese Materialklasse zeigt aufgrund ihrer intensiven Wechselwirkung mit zirkular polarisiertem Licht ein großes Potenzial für zukünftige Anwendungen.

Die Forschungsarbeit an chiralen Nanostrukturen könnte mit der Untersuchung von neuen Materialsystemen eine entscheidende Wendung nehmen. Beispielsweise bleibt es noch zu beweisen, ob eine vollständige Polarisationsbandlücke bei der bichiralen Klasse von Photonischen Kristallen mit hohem Brechzahlkontrast auftreten kann. Eine vollständige Bandlücke für nur *eine* zirkulare Polarisation könnte eine interessante Erweiterung der ursprünglichen Vorschläge darstellen. Des Weiteren sind chirale Metamaterialien, also künstlich hergestellte effektive Materialien, potenzielle Kandidaten für neuartige zirkulare optische Effekte. Es wurden auf diesem Forschungsgebiet schon qualitativ neue Verhalten gezeigt, die aufgrund der Händigkeit entstehen (z.B. eine negative Phasengeschwindigkeit). Magneto-optische oder auch nichtlineare Effekte in chiralen Metamaterialien werden sicherlich noch weitere Überraschungen mit sich bringen.

Solange Forscher auf dem Gebiet der Optik und Photonik den richtigen Dreh heraushaben, werden künstliche chirale Materialien sicherlich ein aktives und dynamisches Gebiet bleiben.

# 1. Introduction

*"What can more resemble my hand or my ear, and be more equal in all points, than its image in the mirror?"*

Immanuel Kant, 1783

Polarization is considered as one of light's fundamental properties. Accordingly, light-matter interactions are often governed by the course of the electric field vector defining the polarization state of an electromagnetic wave. One of the textbook examples is the phenomenon of light being reflected from a surface. At one particular angle of incidence, Brewster's angle, light with one particular polarization cannot be reflected [1]. Based on this effect, Brewster windows are often employed in modern laser systems with the purpose to introduce polarization-dependent reflection losses.

In daily life, we rarely manage to determine the polarization state of a light wave without the help of additional optics. Interestingly, when looking through polarizing sunglasses, many people are able to observe the polarization of light in form of a yellowish, fuzzy bar in the visual field. The perceived bar is perpendicular to the linearly polarized light produced by the glasses. This phenomenon is called Haidinger's brush and was first described by the Austrian physicist Wilhelm Karl von Haidinger in 1844 [2]. Haidinger's brush is mostly unknown because it is a very faint effect rendering the human eye as weakly sensitive to the polarization state of light. Not so with other "evolutionary optics" in animal kingdom, where a remarkable photonic system exists: The circular vision in a species of crustaceans [3]. The eyes of this aquatic animal detect circular polarization by using a complex vision system with an achromatic quarter-wave plate and photoreceptors very sensitive to linearly polarized light. Moreover, certain areas of their tissue are *chiral*. They consist of helical layered proteins reflecting circular polarization. These animals make use of these chiral reflectors to send circularly polarized signals for intricate social interaction.

With quite some astonishment, researchers investigate such biological systems, which were using nanometer-scale architectures to produce striking optical effects millions of years before we began to manipulate the flow of light with artificial materials [4, 5]. Nature's flabbergasting solutions inspired and motivated us to mimic and improve these optical effects by using tailored man-made media. Special devotion concerned the role of *chirality* in the optical properties of the material class of *photonic crystals*.

The word *chirality* is derived from the Greek stem $\chi\epsilon\iota\rho\sim$ (*hand*$\sim$) and refers to objects that cannot be brought into congruence with their mirror image (enantiomers) by mere rotation and translation in space [6] — just like our two hands. Remarkably, the Prussian philosopher Immanuel Kant had already pinpointed the crux of chirality more than 200 years ago [7], "And yet I cannot put such a hand as is seen in the mirror in the place of its original ..."

Chirality has a long history in optics, beginning in 1848 with Louis Pasteur's epoch-making finding that optical activity is a manifestation of chiral media [8]. Generally speaking, in chiral optical materials, circularly polarized waves propagate differently through the left- and right-handed versions, respectively. For example, in the case of the described aquatic animal only one of the two circular polarizations is strongly reflected by their chiral external skeleton.

Chirality in man-made tailored materials is a highly regarded scientific topic for more than 100 years. Acharya J. C. Bose fabricated one of the first artificial chiral materials. In the year 1898, he wrote in the Proceedings of the Royal Society of London [9], "In order to imitate the rotation by liquids like sugar solutions, I made elements or "molecules" of twisted jute, of two varieties, one kind being twisted to the right (positive) and the other twisted to the left (negative)... The twisted structure produces an optical twist of the plane of polarization". Bose twisted bundles of 10 cm long parallel fibers of jute leading to a chiral response at microwave frequencies.

Recently, in the spirit of Bose's first experiments, a dramatic increase of interest in *optical* manifestations of chirality in artificial materials can be registered [10]. The flourishing and dynamic field is driven by the opportunity to achieve optical activity and/or circular dichroism which can be orders of magnitude larger than observed in natural substances, such as milk or a sugar solution. Optical activity in natural chiral molecules is typically investigated with light at visible wavelengths, i.e., the dimensions of the screw-like molecules are by far smaller than the wavelength of the interacting electromagnetic wave. As mentioned above, this manuscript is devoted to chiral photonic crystals, which are periodic arrays of materials with different refractive indices. The attribute "photonic" indicates that the structural periodicity and, hence, the dimensions of the chiral building blocks are on the scale of the wavelength of light.

The research field of photonic crystals has been launched and stimulated by the revolutionary theoretical concept of three-dimensional photonic-band-gap materials. In 1987, Eli Yablonovitch and Sajeev John predicted in their pioneering publications [11, 12] that three-dimensional photonic crystals, properly designed and made of at least two materials showing a high refractive index contrast, may completely prohibit the propagation of light in all crystal directions; this particular frequency region is called complete photonic band gap. Broadly speaking, photonic crystals allow for controlling the photonic density of states by a tailored photonic band structure — in analogy to semiconductors, which allow for controlling electrons by their electronic band structure. Correspondingly, photonic crystals allow for realizing unique electro-

magnetic properties and might play an important role for one of the central goals in the field of photonics: Achieving an all-optical circuitry in a photonic microchip [13].

*Chiral* three-dimensional photonic crystals are a very interesting and distinct subclass of photonic crystals. For example, large complete photonic band gaps have been predicted for high-index-contrast silicon "square-spiral" structures with helical building blocks [14]. Corresponding experiments using glancing-angle deposition [15], interference lithography [16], or direct laser writing [17] have been published. However, a complete photonic band gap does not depend on light's polarization because there are simply *no* photonic states in this frequency region to couple to. Thus, the role of chirality was initially not investigated in the publications given above.

Only recently, in addition to complete gaps, theory also predicts polarization stop bands in "circular-spiral" photonic crystals, i.e., stop bands for just *one* of the two circular polarizations [18, 19]. Along the helical axis, right-handed (left-handed) circularly polarized light is reflected from a right-handed (left-handed) photonic crystal. The unmatching polarization is transmitted virtually unaffected. In terms of polarization optics, such polarization stop bands give rise to strong circular dichroism based on reflection rather than absorption. The resulting selectivity is very interesting for applications: Obviously, chiral photonic crystals serve as polarization filters for circularly polarized electromagnetic waves. Moreover, they can potentially be used for designing compact "thin-film" optical diodes [4] and "poor-man's" optical isolators [20]. Circular emitting laser sources have been reported [21], and the structures might also serve as compact sensors for fluids and gases [22].

To date, the fabrication of complex three-dimensional nanostructures for the telecommunication wavelength of 1.55 µm is still a challenge. Creating the required helical twist in man-made photonic crystals demands the possibility for three-dimensional structuring with feature sizes on the order of few hundred nanometers. In this thesis, we meet the challenge to fabricate polymeric chiral photonic crystals inspired by nature's solutions to create chirality on the nanoscale. Advancements in three-dimensional laser lithography allow for the high degree of precision and versatility necessary to fabricate tailored man-made crystals with a selected handedness.

Chirality represents a fundamental aspect in life. Correspondingly, the role of handedness remains a fascinating topic in several branches of science. In optics and photonics, we can surely expect surprises by giving light yet another twist with chiral nanostructures.

### Outline of this thesis

In chapter 2, we introduce some fundamental aspects of chirality to the reader. A brief overview of important historical events concerning chirality is given. Additionally, we introduce basics of polarization optics that are important to classify the optical effects of chiral nanostructures. The third part of this chapter introduces the material class

of photonic crystals by explaining basic concepts, e.g., the occurrence of the photonic band structure.

The biological and chemical chiral systems which provided inspiration for our work on chiral nanostructures are discussed in chapter 3. Moreover, we review concepts of artificial chiral materials. Possible fabrication methods and applications are discussed.

Chapter 4 is devoted to our fabrication method of direct laser writing. An advanced and compact system has been designed and several experimental setups have been realized. We explain the improvements helping considerably to fabricate chiral photonic crystals. Chapter 5 describes experimental setups for the linear-optical characterization in the near- and mid-infrared spectral range. Furthermore, details of our numerical calculations are given.

The experimental results are split in two chapters 6 and 7. For each blueprint, we explain the underlying physics, present a specific design, fabricate the structures, and compare experimental measurements with theoretical calculations.

In chapter 6, we start by describing two basic designs of chiral photonic crystals with one helical axis: Three-dimensional layer-by-layer chiral photonic crystals (inspired by chiral systems found in nature) and circular-spiral photonic crystals (consisting of periodically arranged helices). Next, we present "thin-film" devices based on circular-spiral photonic crystals. Polarizers, "poor-man's" optical isolators, and optical diodes are proposed and explained. The last section is focused on chiral photonic superlattices, which give additional insight in the physics of circular-spiral photonic crystals. In chapter 7, we introduce the concept of bi-chiral photonic crystals — structures with three helical axes inspired by the so-called blue phase of liquid crystals.

Finally, we summarize the results of this thesis in chapter 8 and give a short outlook to future experiments.

# 2. Fundamentals

The aim of this doctoral thesis is the design, fabrication, and characterization of chiral photonic crystals. In the course of this manuscript, we will point out that the handedness of these periodic dielectrics allows for optical properties distinct from photonic crystals without a handedness.

To understand the physics of chiral materials, however, we first have to learn the fundamentals of chirality, polarization optics, and photonic crystals. Thus, this chapter is divided into three parts: The first section 2.1 deals with basic properties of chirality. Important phenomena of polarization optics are discussed in section 2.2, allowing to classify the optical effects of chiral nanostructures. Section 2.3 is to introduce the material class of photonic crystals. Since the field of photonic crystals has become quite broad, the focus is on aspects relevant to the results of this thesis.

## 2.1. Chirality

Symmetry seems to be everywhere in nature. If one looks at plants and animals, one observes that they often have symmetrical body shapes and patterns. Since symmetry is all around, the absence of a symmetry is often meaningful and sometimes easy to detect.

One distinct asymmetry is chirality. The importance of this asymmetry is tremendous for our existence making chirality a research topic in a lot of disciplines of science — from particle physics to life sciences.

### 2.1.1. What is chirality?

The word *chiral* was first introduced into science by Lord Kelvin (1824–1907), who stated in his "Baltimore Lectures on Molecular Dynamics and the Wave Theory of Light" (published later in [6]),

*"I call any geometrical figure, or group of points, chiral, and say that it has chirality, if its image in a plane mirror, ideally realized, cannot be brought to coincide with itself."*

The term chiral is derived from the Greek name *cheir*, meaning *hand* [23]. Indeed, human hands are perhaps the most universally recognized example of chirality. Just try to shake somebody's left hand with the right hand! It's strange, isn't it? The

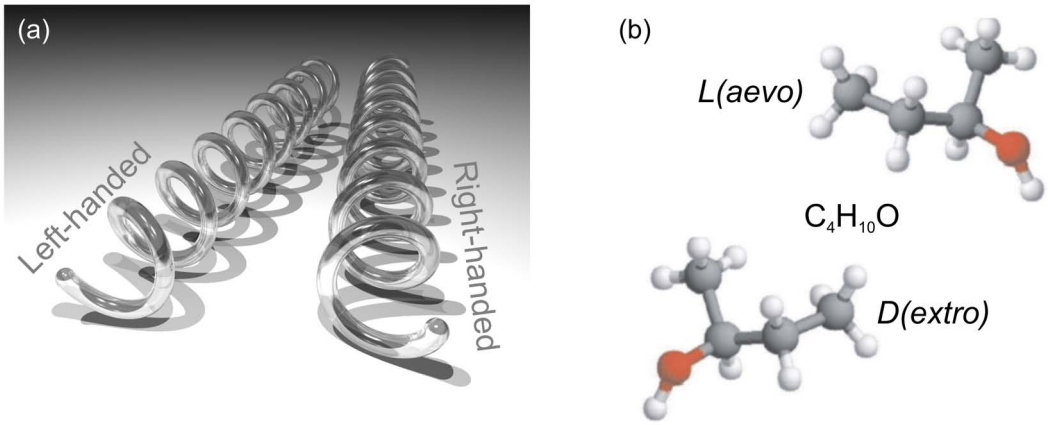


Figure 2.1: (a) The handedness of (enantiomorph) helical objects is quite easy to determine. Clockwise (counterclockwise) rotation results in a right-handed (left-handed) helix. (b) *L*-Butanol is a left-handed chiral molecule, whereas the *D* version is its right-handed mirror image (enantiomer).

left hand is the mirror image of the right hand and, no matter how our hands are oriented, it is not possible to coincide the two objects.

A chiral object and its mirror image are called *enantiomorphs* or, when referring to molecules, *enantiomers*. A non-chiral object is called achiral (or amphichiral) and can be superposed on its mirror image. A mixture of equal amounts of the two enantiomers is said to be a *racemic mixture* [23].

Lord Kelvin's simple geometric definition is accepted to be essential for chirality [24–26]. As a consequence, the pure geometrical statement made chirality a universal concept in very different branches of science. Notably, chirality is, per definition, only observable in three-dimensional (3D) objects. For a two-dimensional (2D) object in a plane, one is always able to mirror the object at this plane. However, there is a mathematical concept of 2D chirality.[1] The reduction to 2D leads to a significant relaxation of the conditions for chirality compared to "normal" chirality. In general, a planar object is chiral if it does not have a symmetry axis in the 2D plane [27]. We will discuss this aspect in chapter 3.

A helical structure is another convenient example of "normal" 3D chirality. In Fig. 2.1(a), a left-handed helix (commonly also called spiral) and its enantiomorph right-handed mirror image are depicted. Clockwise (counterclockwise) rotation results in a right-handed (left-handed) helix. An impressive variety of helical structures can be found in our flora and fauna. It is remarkable that natural chirality exists on macroscopic scale but also on nanoscale. Could we apply these biological methods and

[1] This concept is used for, e.g., adsorbed molecules on surfaces [27] and, recently, for the description of planar chiral metamaterials (see chapter 3.3.1).

systems found in nature to the study and design of artificial chiral photonic crystals? We would like to come back to this exciting aspect in the following chapters.

In (stereo-)chemistry, a lot of studies are devoted to chirality. Usually, for chemists, chirality refers to molecules. Fig. 2.1(b) shows the right-handed and left-handed version of the chiral molecule 2-Butanol. For non-chemists, it seems to be quite hard to determine the handedness. Moreover, there are several naming conventions for chiral molecules. The *R(ectus)/S(inister)* system and the *D(extro)/L(aevo)* system name enantiomers by their atom configuration (see, e.g., [23, 28]). The +/- system takes advantage of the intrinsic optical activity of chiral molecules, i.e., they are characterized by the direction in which the molecules rotate the plane of polarized light. This experimental approach might be more appealing to physicists. We discuss optical activity in more detail in section 2.2.2.

The importance of chirality is magnificently demonstrated in the double-helix structure of deoxyribonucleic acid (DNA). Every living bit on earth carries chiral genotype. Surprisingly, left-handed DNA is completely missing in our nature. This asymmetry that exists if only one enantiomer occurs is named *homochirality* [29]. Interestingly, the vast majority of amino acids, the building blocks of proteins, is left-handed. To date, the evolution of natural homochirality is not understood. However, (homo-)chirality obviously plays a crucial part in the origins of life.

Breaking of mirrorsymmetry is also known from particle physics. For a descriptive understanding of the handedness of a particle, one can use the own hand: The thumb points in direction of the particle motion and the fingers follow the sense of rotation. A particle is right-handed (left-handed) if one can follow the way of motion with the right hand (left hand).[2] A surprising fact in particle physics is that only the left-handed particles and right-handed antiparticles participate in weak interactions. Parity is violated in the weak force in the Standard Model (incorporated in chiral gauge interaction). Parity is a symmetry operation, called point reflection, that is commonly known to flip the signs of all spatial coordinates: $(x,y,z) \rightarrow (-x,-y,-z)$. The remarkable result of parity violation is that the laws of nature are not the same under point reflection — they do distinguish between right and left, between image and mirror image.

Chirality is essential for life and, therefore, turns out to be an exciting topic in science. In the next section, we would like to give a brief overview about historical dates concerning chirality. Structural color in nature took millions of years of evolution and cannot be captured in this history. Nevertheless, we will come back to natural chirality in chapter 3.

[2] Generally, for particles with mass, one has to distinguish between helicity and chirality of a particle and things can get very abstract. For the interested reader, we refer to reference [30].

### 2.1.2. Brief history of chirality

Our timeline of chirality starts with Archimedes of Syracuse (287 BC–212 BC). The famous Greek scientist Archimedes is well known for his contributions to hydrostatics and mathematics but also for the study of spiral structures. He analyzed geometrical forms and arrangements intensively and is also known as the inventor of many mechanical devices. The Archimedean water screw represents an outstanding invention to transfer water to higher levels. However, the chiral screw is just one prominent example of antique age; chirality is certainly still apparent in a lot of man-made mechanical parts.

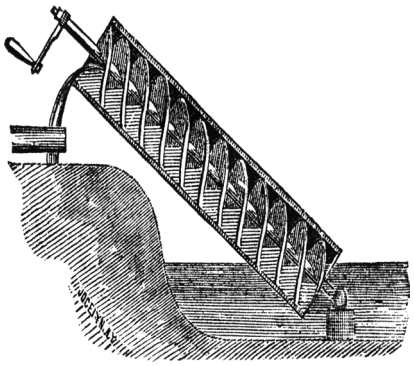

Figure 2.2: The Archimedean water screw [31].

Immanuel Kant (1724–1804), the famous Prussian philosopher, was the first to describe the existence of enantiomorph objects in 1783 [7, 32],

*"What can more resemble my hand or my ear, and be more equal in all points, than its image in the mirror? And yet I cannot put such a hand as is seen in the mirror in the place of its original"*

Kant's analysis of handedness clearly fits in today's understanding of chiral objects. Thus, the "knowledge" of chirality has been around for more than 200 years.

With the ability to polarize light in the early 19th century, systematic studies of light-matter interactions became possible. Natural optical rotation of the plane of linearly polarized light was first observed by Dominique F. J. Arago (1786–1853) in 1811 [33]. In his experiments, he studied the polarization properties of quartz crystals. In 1815, Jean-Baptiste Biot (1774–1862), a French physicist best known for the Biot-Savart law, discovered that this optical rotation is not restricted to crystals [34]. Certain organic liquids or solutions are also optically active — even a simple sugar solution.

With this background, Louis Pasteur (1822–1895) was able to identify optical activity as manifestation of chiral media [8]. In the year 1848, with the age of only 26, he was puzzling why natural tartaric acid is optical active, whereas his synthesis of nominally the "same" acid remained inactive. Under close examination, he could distinguish two different asymmetric molecules in his synthesis. The molecules looked like mirror images of each other, enantiomers. The natural acid only consisted of one of these two molecules. He concluded that one molecule turns the polarization plane to the left; the other to the right. The racemic mixture remains optically inactive. Later, he went even further and postulated,

*"The universe is asymmetric and I am persuaded that life, as it is known to us, is a direct result of the asymmetry of the universe or of its indirect consequences."*

Pasteur also tried to find a link to an optical effect that Michael Faraday (1791–1867) discovered in 1846 [35]. Faraday applied a static magnetic field parallel to a light beam and (also) observed a rotation of linear polarization. Although the Faraday rotation is not restricted to chiral media, Pasteur thought this to be the origin of chirality. He decided to grow chiral crystals in an applied magnetic field but his experiments failed because of the distinctiveness of both effects. Recent work on magneto-chiral dichroism is inspired by Pasteur's unsuccessful experiments [36].

In 1874, Joseph A. LeBel (1847–1930) and Jacobus H. van't Hoff (1852–1911) independently proposed "asymmetric carbon atoms" as basis for molecular chirality [37, 38]. This argumentation also extended the explanation of Pasteur's former experiments with tartaric acid.

14 years later, Friedrich Reinitzer (1857–1927) and Otto Lehmann (1855–1922) collaborated to understand Reinitzer's cholesterol derivatives [39]. Reinitzer observed a color change in cholesteryl benzoate. Moreover, the sample showed the unusual behavior that it melts to a "cloudy" liquid and, at higher temperature, melts again to a clear liquid. In between these phases, the sample turned blue (this *blue phase* will be discussed in chapter 3). He contacted Otto Lehmann for help with the explanation. Later on, this meso-phase between crystals and liquids was called "liquid crystals". They are a prominent example of chiral materials because they can arrange in a helical manner and reflect circular polarization selectively. In the 1970s they became an industrial product because of the possibility to tune their arrangement electrically.

In the year 1893, Lord Kelvin (1824–1907) defined chirality (published later in [6]). Only five years later, in 1898, the first artificial chiral medium was investigated. Acharya J. C. Bose (1858–1937) successfully tried to imitate natural optical activity with twisted jute [9]. Bose's experiments were performed in the microwave regime.

Since 1901, the Nobel Prize is annually awarded for achievements in chemistry, medicine, physics, literature, and peace. In the first three disciplines, the honorable prize has been awarded several times for work connected with chirality. Three examples:

- Nobel Prize 1954 in chemistry for Linus Pauling (1901–1994): "for his research into the nature of the chemical bond and its application to the elucidation of the structure of complex substances" (Discovery of the alpha-helix in protein).
- Nobel Prize 1957 in physics for Tsung D. Lee (*1926) and Chen N. Yang (*1922): "for their penetrating investigation of the so-called parity laws which has led to important discoveries regarding the elementary particles" (Discovery of parity violation in particle physics).
- Nobel Prize 1962 in medicine for Francis Crick (1916–2004), James D. Watson (*1928), and Maurice Wilkins (1916–2004): "for their discoveries concerning the molecular structure of nucleic acids and its significance for information transfer in living material" (Discovery of DNA double-helix).

Chirality is surely a fascinating topic. Recently, it evolved to be a hot topic in optics and photonics because it became possible to artificially create chiral structures with nano- and microfabrication techniques. Structuring on nanoscale allows for new optical technologies, and, as a consequence, a whole research field evolved with the aim to design and fabricate functional chiral media.

## 2.2. Polarization optics

Devices to control the polarization state of light are some of the most important elements in an optical system. Recently, chiral periodic nanostructures have been introduced as thin-film candidates to mold and control the flow of polarized light [14–21, 40–44] (see chapter 3). Characterization of the these new materials demands the knowledge of basic interactions of polarized light with matter. Therefore, the next sections are devoted to polarization optics.

### 2.2.1. Eigenstates of polarization

Polarization of light was discovered by Louis Malus (1775–1812) at the end of the year 1808 [45]. Malus used a doubly refracting crystal to follow the path of light, reflected from a window. In this experiment, he found different intensities for different orientations of the crystal. At a certain angle (Brewster's angle), the reflected light can be completely extinguished. Ever since, polarization is considered as one of light's fundamental properties. First, what is light?

#### Vectorial nature of light

Light can be described as an electromagnetic wave or a stream of discrete photons. In the context of this thesis, the wave character of light is the best choice to explain the underlying physics. Therefore, we describe light as a transverse wave which fulfills the wave equation derived from Maxwell's equations. The vectorial nature of these light waves defines their *polarization* (see, e.g., [46]).

To introduce the eigenstates of polarization to the reader, we investigate the course of the electric field $\vec{E}$ traveling in a linear, non-dispersive, homogeneous, isotropic, and source-free medium.[3] In this case, the electric field $\vec{E}$ satisfies Maxwell's equations if each of the components fulfills the following wave equation:

$$\nabla^2 u - \frac{1}{c^2}\frac{\partial^2 u}{\partial t^2} = 0\,, \tag{2.1}$$

[3] Here, we set the derivation of the wave equation aside because a more general version for photonic crystals is discussed in section 2.3.

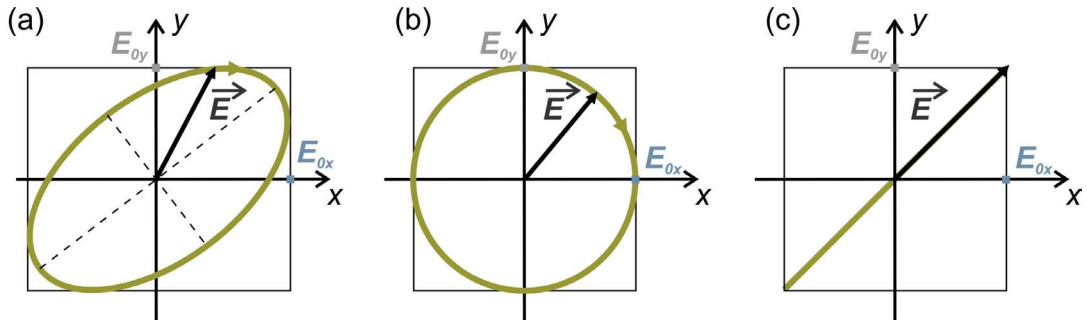


Figure 2.3: (a) Elliptical, (b) circular, and (c) linear polarization (observed by a *receiver*).

where the speed of light in the medium is denoted as $c = (\varepsilon\mu)^{-1/2}$, $\varepsilon$ is the electric permittivity, and $\mu$ is the magnetic permeability of the medium. One well-known solution of the wave equation (2.1) is a monochromatic plane light wave with angular frequency $\omega$ and the $z$-component $k$ of the wave vector that can be written as

$$\vec{E}(z,t) = \hat{x}E_{0x}\cos(kz - \omega t) + \hat{y}E_{0y}\cos(kz - \omega t + \phi)\,, \tag{2.2}$$

where $\hat{x}\cdot\hat{y} = 0$. $\phi$ corresponds to the phase retardation between both field components and $v_{ph} = \omega/k$ to the phase velocity. The wave travels in positive $z$-direction. The vectorial nature of the electric field $\vec{E}$ is directly related to equation (2.2). By choosing different values of amplitudes $E_{0x}$ and $E_{0y}$ and phase retardation $\phi$, we can introduce common cases of polarization (shown in Fig. 2.3).

### Linear and circular expansion basis

Generally, the tip of the electric field vector lies on the ellipse

$$\frac{E_x^2}{E_{0x}^2} + \frac{E_y^2}{E_{0y}^2} - 2\cos\phi\frac{E_x E_y}{E_{0x}E_{0y}} = \sin^2\phi\,. \tag{2.3}$$

This state is called *elliptical* polarization. An important special case of an ellipse is a *circle*. For a circle, the phase difference has to be $\phi = \pm\pi/2$ and, moreover, the amplitudes need to be equal, i.e., $E_{0x} = E_{0y}$. Hence, we obtain:

$$\vec{E}_{\mathrm{CP}}(z,t) = E_0[\cos(kz - \omega t) \mp \sin(kz - \omega t)]\,. \tag{2.4}$$

Here, "CP" indicates *circular* polarization.

If $\phi = -\pi/2$, the field vector at a fixed $z$-position rotates clockwise when observed by a *receiver*.[4] This polarization is called right circular polarization (RCP) (illustrated

[4]We would like to mention that, in a different convention, circular polarization is defined in the opposite way (when observed by the source).

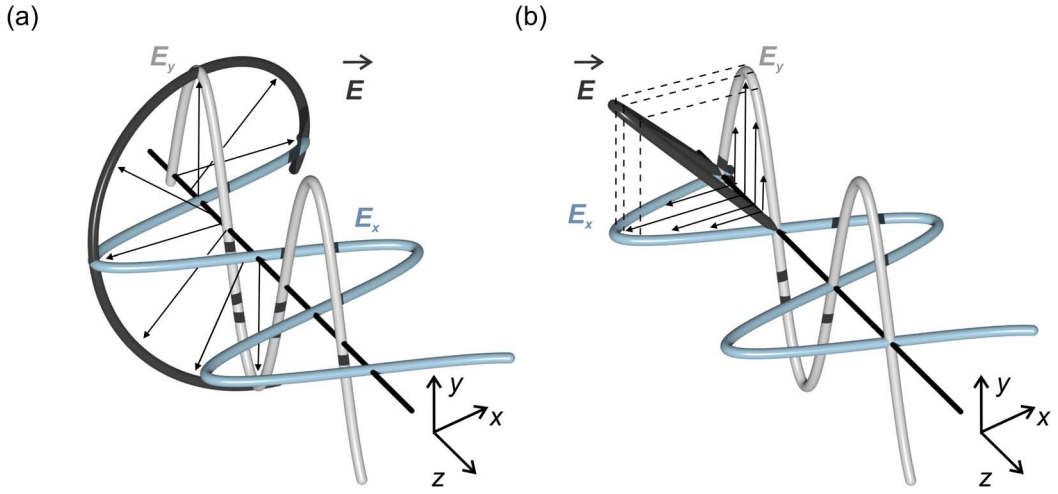


Figure 2.4: (a) Right(-hand) circular polarization (RCP): $E_x$ and $E_y$ have the same amplitude but a phase retardation of $\phi = -\pi/2$. The tip of the electric-field vector follows a right-handed helix. At a fixed $z$-position, one detects a clockwise circle (when observed by a receiver). (b) Linear polarization: The waves have the same amplitude and are in phase.

in Fig. 2.4(a)). For $\phi = +\pi/2$, it rotates counterclockwise and the polarization is said to be left circular (LCP). If one follows the tip of the electric field vector, RCP (LCP) creates a right-handed (left-handed) helix.

The case of *linear* polarization is depicted in Fig. 2.4(b). Both components $E_x$ and $E_y$ are superimposed to the linear polarization state of the electric field, $\vec{E}_{\mathrm{LIN}}$, that reads (for $\phi = 0$)

$$\vec{E}_{\mathrm{LIN}}(z,t) = (\hat{x}E_{0x} + \hat{y}E_{0y})\cos(kz - \omega t)\,. \tag{2.5}$$

It is called linear because the resulting vector will always be on one line (when observed by a *receiver*). Linear polarization also results for $\phi = \pm 2n\pi$ (in-phase) and $\phi = \pm(2n+1)\pi$ (out-of-phase), $n \in \mathbb{Z}$.

Linear and circular polarization are commonly used in polarization optics. First, both are an expansion basis and can always generate arbitrary polarization states by superposition. Secondly, in light-matter interactions, the *eigenstates* of polarization are often connected with the matter structure, and it turns out that linear and circular polarization often fit well to explain the effects. For example, for natural optical activity, circular polarization is typically used as eigenstates because the response can be described by a simple phase retardation of LCP and RCP. In this case, the medium does not convert from the circular to linear basis, i.e., it "provides" circular eigenstates.

Table 2.1.: Examples of Jones vectors representing the polarization state of light.

| Polarization | Jones vector |
|---|---|
| Linear in $x$-direction | $\vec{J} = \begin{pmatrix} 1 \\ 0 \end{pmatrix}$ |
| Linear in $y$-direction | $\vec{J} = \begin{pmatrix} 0 \\ 1 \end{pmatrix}$ |
| Right circularly polarized | $\vec{J} = \frac{1}{\sqrt{2}} \begin{pmatrix} 1 \\ -\mathrm{i} \end{pmatrix}$ |
| Left circularly polarized | $\vec{J} = \frac{1}{\sqrt{2}} \begin{pmatrix} 1 \\ \mathrm{i} \end{pmatrix}$ |

### Jones formalism

Jones calculus is very convenient as mathematical representation for polarization. Jones vectors $\vec{J}$ are denoted as

$$\vec{J} = \begin{pmatrix} E_x \\ E_y \end{pmatrix} \tag{2.6}$$

and are usually normalized such that $|E_x|^2 + |E_y|^2 = 1$ holds. Polarizations $\vec{J_1}$ and $\vec{J_2}$ are orthogonal if their inner product $(\vec{J_1},\vec{J_2}) = E_{x1}E_{x2}^* + E_{y1}E_{y2}^*$ disappears. Orthogonal Jones vectors are an expansion basis and can always generate arbitrary polarization vectors by superposition. Table 2.1 contains some examples for Jones vectors. Obviously, RCP and LCP form an expansion basis.

If light passes through a linear optical system, matrix optics allows us to determine the Jones vector behind the system. The matrix is called Jones matrix $\hat{\mathcal{T}}$ (2×2 matrix), and the input and output waves are connected by the relationship (2.7):

$$\vec{J_2} = \hat{\mathcal{T}}\vec{J_1} = \begin{pmatrix} T_{11} & T_{12} \\ T_{21} & T_{22} \end{pmatrix} \vec{J_1}\,. \tag{2.7}$$

As an example, we consider an optical system that has circular eigenstates. This system should be transparent for LCP but completely opaque for RCP. Corresponding optics might be called “circular polarizer” and are associated with Jones matrix (2.8):

$$\hat{\mathcal{T}} = \frac{1}{\sqrt{2}} \begin{pmatrix} 1 & -\mathrm{i} \\ \mathrm{i} & 1 \end{pmatrix}. \tag{2.8}$$

More polarizing systems, as well as wave retarders, can easily be described with Jones matrices. Other approaches to represent polarization like the Poincaré sphere, Stokes parameters, or Mueller matrices will not be discussed here (for details see, e.g., [46]).

### 2.2.2. Basic interactions of polarized light with matter

The geometrical structure of an optical system can affect the polarization of light as it passes through. These effects are named linear if the linear basis of polarization is chosen as the eigenstate; and circular if circular polarization is the best choice for the description. The most simple example for a system which can be described by a linear basis of polarization is a crystal with one optical axis. For chiral media, circular polarization is used as expansion basis.

#### Linear dichroism and birefringence

The term *dichroism* is derived from the Greek word *dichroos* and means *two colors*. Linear dichroitic materials selectively absorb one of the two orthogonal linear eigenstates of light. One of the best known examples is the linear dichroitic semi-precious stone tourmaline. Some forms of tourmaline change their color when viewed in different crystal directions. One optical axis of the stone absorbs an incident light wave strongly when the electric field plane is parallel. In comparison, the component perpendicular to this axis is absorbed very weakly. This optical asymmetry allows for using dichroitic substances as linear polarizers.

Absorption bands in the visible spectral region obviously lead to different colors for different crystal directions, explaining why the effect has been named dichroism.[5] However, this optical property is neither restricted to the visible region nor to natural crystals. A *wire-grid polarizer* is a man-made dichroitic device. Here, the relevant axis is along the metallic wires. If the electric field is parallel to the wires, a current can be induced and light is absorbed. Obviously, one expects less absorption for an electric field perpendicular to the wires. Such wire-grid polarizers have been used by Heinrich Hertz (1857–1894) for his epoch-making experiments on electromagnetic waves (in Karlsruhe, 1887). Nowadays, commercial wire-grid polarizers cover wavelengths from 2 µm to 30 µm, have high transmission and high extinction ratios.

Dichroism is just one side of the medal. Generally, a substance which possesses two different refractive indices is said to be *birefringent*.[6] Birefringence and dichroism can be described with the Lorentz oscillator model. This simplest picture of atom-field interactions is schematically shown in Fig. 2.5(a). The Lorentz oscillator model allows for the derivation of the refractive index, which reads in case of non-magnetic dielectric material (e.g., tourmaline or calcspar)

$$n(\omega) = \sqrt{\epsilon(\omega)} = \sqrt{1 + \frac{n_0 q_e^2}{\varepsilon_0 m_e} \frac{1}{\omega_0^2 - \omega^2 - \mathrm{i}\gamma\omega}}\,. \tag{2.9}$$

Here, $n_0$ corresponds to the oscillator density, $q_e$ to the elementary charge, $m_e$ to the electron mass, $\gamma$ to the factor of attenuation, and $\omega_0$ to the resonance frequency of the

[5] For crystals with two relevant optical axes, the effect is called trichroisms.
[6] Biaxial birefringence is also called trirefringence.

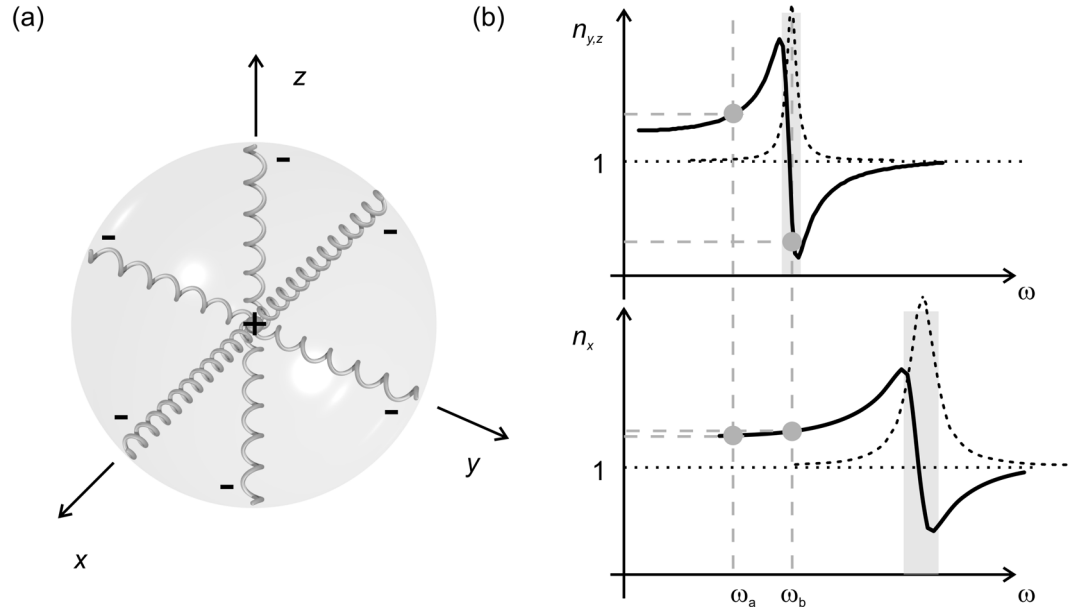


Figure 2.5: (a) Lorentz oscillators serve as model to derive the refractive index of birefringent media. (b) Schematic plots of the refractive index in different directions. The solid lines show the real part of the refractive index, whereas the dotted lines correspond to the imaginary part. Adapted from [46].

mass-spring system [46]. We model a birefringent system with springs which have the same oscillator strengths and attenuations in $y$- and $z$-direction, but different values in $x$-direction. Therefore, the response will dependent on the spatial direction resulting in different refractive indices, i.e., $n_y = n_z \neq n_x$. According to Fig. 2.5(b), frequency $\omega_a$ corresponds to a region where the material is purely birefringent. Whereas at frequency $\omega_b$, the imaginary part of the refractive index for the $y$- and $z$-direction is not negligible anymore. Since the absorption band for the other direction is at higher frequencies, a material with this property is said to be dichroitic.

When $x$ is the axis of anisotropy, one also names the parallel refractive index $n_x$ extraordinary. $n_y$ and $n_z$ are the indices perpendicular to the axis of anisotropy and are called ordinary. Consequently, if an unpolarized light wave impinges onto birefringent material in an oblique angle to the axis of anisotropy, light can be separated in two polarized waves: The ordinary and the extraordinary wave. The first experiences one refractive index and is just transmitted. However, due to different wave velocities perpendicular and parallel to the *slanted* optical axis, the light wave can also experience both refractive indices. Therefore, this extraordinary wave will be refracted in another direction compared to the ordinary wave. This leads to a beam displacement which can potentially be used to create polarized light.

### Circular dichroism and birefringence

When dealing with chiral media, circular eigenstates of light are usually used for the description of the effects. Chiral materials provide different (complex) refractive indices and, therewith, different propagation speeds for LCP and RCP. This phenomenon is called *circular birefringence*. In analogy to the case of linear effects, circular dichroism and circular birefringence can occur separately or at the same time.

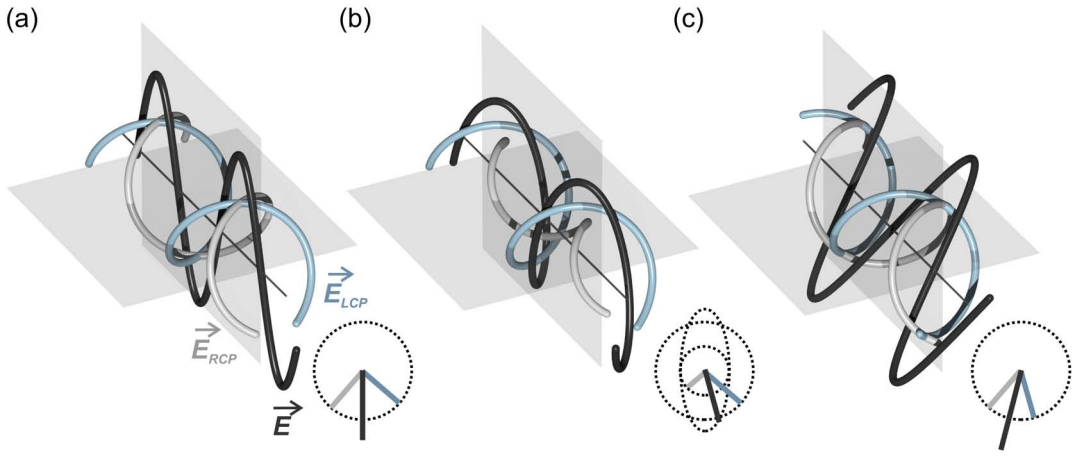


Figure 2.6: (a) Linear polarization (dark gray) is superimposed by RCP (light gray) and LCP (cyan blue). (b) Circular dichroism: Half of RCP is absorbed resulting in elliptically polarized light. (c) Circular birefringence: The phases of LCP and RCP are retarded relatively to each other because of different propagation speeds. Linear polarization is rotated when passing through a birefringent media.

If light impinges on a chiral medium and one of the circular polarizations is more absorbed than the other, this medium is said to be *circular dichroitic*. If linear polarization impinges circular dichroitic media, the transmitted wave is generally elliptically polarized. As depicted in Fig. 2.6(b), the amplitudes of RCP and LCP are different because of different absorption (here, 100% LCP is transmitted but only 50% RCP). The shorter (longer) semi-axis of the resulting ellipse corresponds to the amplitude of RCP (LCP).

How do we observe circular birefringence? We expect a rotation (gyration) of the plane of polarization of linearly polarized light due to different propagation velocities of RCP and LCP. Fig. 2.6(c) shows the corresponding case. Here, right-handed light (shown in light gray) propagates faster than left-handed light (cyan blue) because the refractive index $n_{\mathrm{RCP}}$ is smaller than $n_{\mathrm{LCP}}$. Accordingly, the rotation of the plane is clockwise. In this case the absorption is completely neglected.[7]

[7] The combination of both effects, circular dichroism and birefringence, manifests in a rotation of the semi-axis of the resulting ellipse.

Gyration or rotation is linked with the structural arrangement of the material. Therefore, chiral media can be characterized by the rotation of linear polarization. Optical activity has a long history in optics as manifestation of chiral molecules and is discussed in the next section.

### Optical activity

The origin of optical gyration is the (molecular) asymmetry of the optical active materials. Parity symmetry is broken in chiral molecules. Therefore, a measurement of optical active media can be used to characterize properties of chiral substances. In a typical experiment, chiral media are classified by the direction one has to turn a previously crossed analyzing polarizer to obtain minimal transmittance again. A substance that turns left, as seen from a receiver, is called left-handed. Right-handed media turn the plane to the right.

The theoretical description of natural optical activity is complex and has to be explained with quantum mechanics. However, we want to give some simple equations that will be helpful for later chapters of this thesis. Incident linear polarization can be written as superposition of the electric fields, $\vec{E}_{\mathrm{RCP}}$ and $\vec{E}_{\mathrm{LCP}}$,[8] that read

$$\vec{E}_{\mathrm{RCP}}(z,t) = \frac{E_0}{2}[\hat{x}\cos(k_{\mathrm{RCP}}z-\omega t)+\hat{y}\sin(k_{\mathrm{RCP}}z-\omega t)]\,, \tag{2.10}$$

$$\vec{E}_{\mathrm{LCP}}(z,t) = \frac{E_0}{2}[\hat{x}\cos(k_{\mathrm{LCP}}z-\omega t)-\hat{y}\sin(k_{\mathrm{LCP}}z-\omega t)]\,. \tag{2.11}$$

For a fixed frequency $\omega$, it holds: $k_{\mathrm{RCP}} = k_0 n_{\mathrm{RCP}}$ and $k_{\mathrm{LCP}} = k_0 n_{\mathrm{LCP}}$. Trigonometric theorems allow for the following derivation:

$$\begin{aligned}\vec{E}(z,t) &= \vec{E}_{\mathrm{RCP}}(z,t)+\vec{E}_{\mathrm{LCP}}(z,t)\\ &= E_0[\cos((k_{\mathrm{RCP}}+k_{\mathrm{LCP}})\frac{z}{2}-\omega t)]\\ &\quad\cdot\left[\hat{x}\cos((k_{\mathrm{RCP}}-k_{\mathrm{LCP}})\frac{z}{2})+\hat{y}\sin((k_{\mathrm{RCP}}-k_{\mathrm{LCP}})\frac{z}{2})\right]\,.\end{aligned} \tag{2.12}$$

Suppose a linearly polarized light wave enters the material ($z=0$) and is polarized in $x$-direction. By looking at the equations (2.10)–(2.12), it is clear that the time dependence of both components is not changing along the way. The resulting wave remains linearly polarized all the time. However, it is dependent on the spatial coordinate. The oscillation plane rotates proportional to the distance $d$, which corresponds to the material thickness. If the rotation angle $\beta$ is positive (negative), the medium is right-handed (left-handed). By analyzing equation (2.12), one can derive the turning angle:

$$\begin{aligned}\beta &= -(k_{\mathrm{RCP}}-k_{\mathrm{LCP}})\frac{z}{2}\\ &= (n_{\mathrm{LCP}}-n_{\mathrm{RCP}})\frac{\pi d}{\lambda_0}\,.\end{aligned} \tag{2.13}$$

[8] Note the different normalization in section 2.2.1.

If $n_{\mathrm{LCP}} > n_{\mathrm{RCP}}$, the medium is right-handed; and if $n_{\mathrm{RCP}} > n_{\mathrm{LCP}}$, the medium is left-handed. An example for optical active material which does not show linear birefringence is $NaClO_3$. The rotation angle is typically given per mm of sample thickness and reaches a value of $\beta = 3.1°/\mathrm{mm}$ for $NaClO_3$. Values are usually measured by using yellow light of a sodium lamp (e.g., D-line: $\lambda = 589\,\mathrm{nm}$) and atmospheric pressure.

### Faraday effect

The *Faraday effect* allows achiral structures to act as if they were chiral. More generally, this is possible under the influences of external fields (mechanical, magnetic, electric etc.). If rotating effects take place (without absorption), the following material equation can be derived:

$$\frac{1}{\varepsilon_0} D_i = \varepsilon'_{ij} E_j + \mathrm{i}(\vec{E} \times \vec{g})_i \,. \tag{2.14}$$

External fields, like an electrical field $E^0$, a magnetic field $H^0$, or a mechanical tension field $e^0$ are responsible for the gyration vector $\vec{g}$, for which the components can be written [47]:

$$\begin{aligned} g_i = \quad & \gamma_{ij} k_j && \text{(Optical activity)} \\ + \quad & \zeta_{ij} H^0_j && \text{(Faraday effect)} \\ + \quad & \gamma_{ijk} \kappa_j E^0_k && \text{(Electro-gyration)} \\ + \quad & \gamma_{ijkm} \kappa_j E^0_k H^0_m && \text{(Magneto-electro-gyration)} \\ + \quad & \gamma_{ijkm} \kappa_j e^0_{km} && \text{(Elasto-gyration)}\,, \end{aligned} \tag{2.15}$$

where $k_j$ is $j$th component of $\vec{k}$-vector and $\kappa_j$ is equal to $\frac{k_j}{|\vec{k}|}$. The material parameters are summarized with $\zeta$ and $\gamma$.

As an implication, substances without natural chirality can also turn the polarization plane. Importantly, the magneto-optical Faraday effect breaks *time-reversal* symmetry (i.e., reciprocity). In contrast, natural optical activity origins in the breaking of *parity* symmetry.

The convention of the Faraday effect is that a positive constant of a diamagnetic material rotates linear polarization in the direction of a right-handed screw if the propagation of the light field is parallel (antiparallel) to the magnetic induction [48].

The theoretical description of the Faraday effect is again complicated. However, we want to give a descriptive classical explanation: Suppose, electrons are bound elastically, and the electric field vector moves on its helical trajectory. Because of the magnetic field, a force affects the movement of the electrons. This force will point to the helix axis or away from it, depending on the magnetic field and the polarization. This will lead to different polarizabilities and, thus, to different refractive indices for

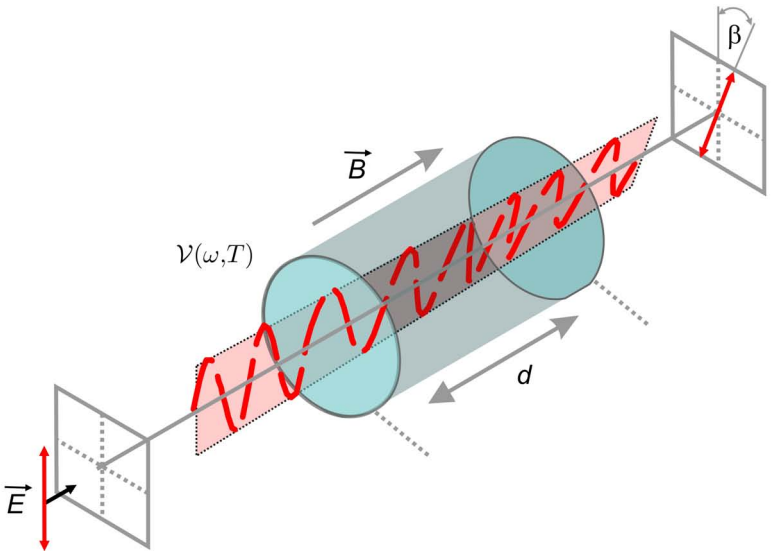


Figure 2.7: Illustration of the Faraday effect: The plane of linear polarization is rotated while passing the medium. A parallel magnetic field and a positive Verdet constant lead to a rotation in the direction of a right-handed screw.

circular polarization. For an applied magnetic induction $B$ and a travel distance $d$, the rotation angle is given by

$$\beta = \mathcal{V}(\omega,T)Bd\,. \tag{2.16}$$

The Verdet constant $\mathcal{V}(\omega,T)$ is a material parameter and depends on frequency and temperature. An example: With a given magnetic induction $B$ of 1 Tesla, water can rotate linear polarization about an angle of 2°/cm.

Nevertheless, the induced circular birefringence in the Faraday effect is clearly governed by the direction of the magnetic field. Double-passing through Faraday material results in the doubled rotation angle, whereas in natural circular birefringent media, the rotation is effectively canceled. The non-reciprocal character of the Faraday effect originates from the static magnetic field that points always in a tagged direction, i.e., parallel or antiparallel to the propagation of light. This aspect is distinct to natural optical active substances that are reciprocal. The reason for the reciprocal response is that the handedness of a helix is fixed if observed by a receiver *or* by the source.

There is a set of applications for magneto-optical effects. One important example is the Faraday optical isolator. Typically, commercial Faraday isolators will suppress light on the way back by 4 orders of magnitude and are employed to reduced feedback in a laser cavity. Its first component, a linear polarizer, is followed by a Faraday element and an analyzer. If light is horizontally polarized, it is rotated by 45°. The analyzer should be adjusted so that transmission is maximum (i.e., 45° with respect to the polarizer). Since on the way back, the plane of polarization is turned by another 45°, the polarizer will block the light and reduce feedback.

## 2.3. Photonic crystals

Light-matter interaction is of fundamental importance in physics. Accordingly, possible manipulation of *light with matter* and *matter with light* has been investigated by many research groups all over the world [49]. This effort has lead to numerous scientific advances. Lasers, fiber optics, DVDs, and the entire field of photonics are just some of the everyday uses based on these principles.

Many scientists have contributed to the research on the control and manipulation of these interaction processes. More than 20 years ago, an intellectual milestone has been reached: The proposal of photonic crystals to mold the flow of light. The vision is to design and modify the density of states of the radiation field to control, e.g., the spontaneous emission of materials embedded within the photonic crystal.

Ever since the pioneering work of Eli Yablonovitch and Sajeev John has been published [11, 12], extensive theoretical investigations have revealed unique optical properties of photonic crystals. Modern micro- and nanofabrication methods meet the high demands on quality and uniformity. The field of photonic crystals is mature but still evolving rapidly. The status is reviewed in more comprehensive articles [50].

In the next section, a basic theoretical description of photonic crystals is presented. In order to understand the fascination of this class of materials, basic optical properties are discussed in section 2.3.2. Methods used for fabrication are presented later in chapter 3.

### 2.3.1. Theoretical description

Periodic arrays of materials with different refractive indices are called *photonic crystals*. The attribute "photonic" indicates that the structural periodicity is on the scale of the wavelength of the radiation field. For visible light, for example, the lattice constant does not exceed a few hundred nanometers explaining the high demands on fabrication techniques.

As depicted in Fig. 2.8, photonic crystals can be classified in three groups: One-dimensional (1D), two-dimensional (2D), and three-dimensional (3D); depending on how many spatial coordinates are structured in a periodic manner. In analogy to ordinary crystals, we characterize them with their lattice constant $a$. Note that ordinary crystals have lattice constants on the order of Ångströms. Photonic crystals need to consist of at least two materials with different refractive indices (A and B in Fig. 2.8). A simple example for a 1D photonic crystal is a dielectric mirror consisting of multiple layers of different materials.

In order to gain more understanding on how the radiation field in a photonic crystal can be controlled, we have to derive the eigenvalue problem.[9]

[9] There are already several textbooks on photonic crystals. For theoretical details, we refer to [51,52].

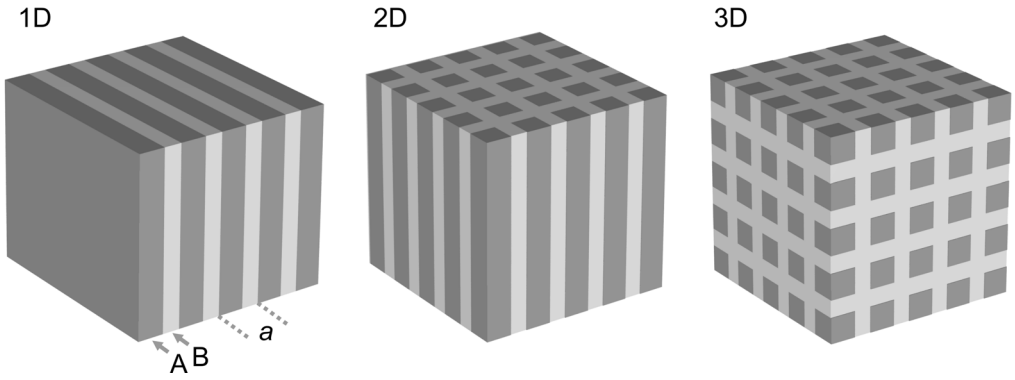


Figure 2.8: The dimensionality of the structural periodicity plays a crucial role for the optical properties. Therefore, photonic crystals are classified in 1D, 2D, and 3D specimens.

### Eigenmodes of photonic crystals

The starting point for theoretical considerations are the macroscopic Maxwell equations in SI units:

$$\nabla \cdot \vec{D} = \varrho \tag{2.17}$$

$$\nabla \cdot \vec{B} = 0 \tag{2.18}$$

$$\nabla \times \vec{E} = -\frac{\partial \vec{B}}{\partial t} \tag{2.19}$$

$$\nabla \times \vec{H} = \vec{j} + \frac{\partial \vec{D}}{\partial t}\,. \tag{2.20}$$

The free electric charge density $\varrho$ and the free electric current density $\vec{j}$ are associated with the charge conservation law (2.21):

$$\nabla \cdot \vec{j} + \frac{\partial \varrho}{\partial t} = 0\,. \tag{2.21}$$

However, we can assume that free charges and electric current are absent in dielectric photonic crystals, hence: $\vec{j} = 0$ and $\varrho = 0$. Furthermore, it is reasonable (in our case) to restrict the discussion on isotropic, non-dispersive, and transparent materials; and on linear optics. Accordingly, the dielectric tensor $\underline{\underline{\varepsilon}}(\vec{r},\omega)$ is a real scalar and reads

$$\underline{\underline{\varepsilon}}(\vec{r},\omega) = \varepsilon(\vec{r})\,. \tag{2.22}$$

As a result, the electric field $\vec{E}$ and the dielectric displacement $\vec{D}$ fulfill the relationship (2.23):

$$\vec{D}(\vec{r}) = \varepsilon_0 \varepsilon(\vec{r}) \vec{E}(\vec{r})\,. \tag{2.23}$$

Because we assume non-magnetic materials, the magnetic induction $\vec{B}$ and the magnetic field $\vec{H}$ are related like in free space resulting in equation (2.24):

$$\vec{B}(\vec{r}) = \mu_0 \vec{H}(\vec{r})\,. \tag{2.24}$$

The time dependency of the fields is given by:

$$\vec{H}(\vec{r},t) = \vec{H}_\omega(\vec{r})\mathrm{e}^{-\mathrm{i}\omega t} \tag{2.25}$$
$$\vec{E}(\vec{r},t) = \vec{E}_\omega(\vec{r})\mathrm{e}^{-\mathrm{i}\omega t}\,. \tag{2.26}$$

With the relationships (2.23)–(2.26), the set of equations (2.17)–(2.20) changes to:

$$\nabla \cdot \vec{D}_\omega(\vec{r}) = 0 \tag{2.27}$$
$$\nabla \times \vec{E}_\omega(\vec{r}) = \mathrm{i}\omega\mu_0\vec{H}_\omega(\vec{r}) \tag{2.28}$$
$$\nabla \cdot \vec{B}_\omega(\vec{r}) = 0 \tag{2.29}$$
$$\nabla \times \vec{H}_\omega(\vec{r}) = -\mathrm{i}\omega\varepsilon_0\varepsilon(\vec{r})\vec{E}_\omega(\vec{r})\,. \tag{2.30}$$

The constants $\mu_0$ and $\varepsilon_0$ are related to the vacuum velocity of light $c_0 = (\mu_0\varepsilon_0)^{-1/2}$. $w$ corresponds to the eigenangular frequency.

To derive the eigenvalue problem, equation (2.30) has to be divided by $\varepsilon(\vec{r})$ and the rotation $\nabla\times$ has to be multiplied on both sides. Finally, equation (2.28) needs to be inserted to find the master equations of the magnetic field:

$$\mathcal{L}_H\vec{H}_\omega(\vec{r}) = \nabla \times \left(\frac{1}{\varepsilon(\vec{r})}\nabla \times \vec{H}_\omega(\vec{r})\right) = \left(\frac{\omega}{c_0}\right)^2 \vec{H}_\omega(\vec{r})\,. \tag{2.31}$$

Along these lines, we can also derive the master equation of the electric field:

$$\mathcal{L}_E\vec{E}_\omega(\vec{r}) = \frac{1}{\varepsilon(\vec{r})}\nabla \times \left(\nabla \times \vec{E}_\omega(\vec{r})\right) = \left(\frac{\omega}{c_0}\right)^2 \vec{E}_\omega(\vec{r})\,. \tag{2.32}$$

(2.31) and (2.32) are the essential equations for the theoretical description of photonic crystals.

Solutions of the electromagnetic wave in a photonic crystal can be derived and understood if we compare known results from solid state physics. Electronic waves in a periodic potential of ordinary crystals are expanded in Bloch waves. Electronic waves are scalar, however, the Bloch-Floquet theorem also holds true when dealing with photonic crystals [51, 52], i.e.:

$$\vec{E}_\omega(\vec{r}) = \vec{E}_{\vec{k}n}(\vec{r}) = \vec{u}_{\vec{k}n}(\vec{r})e^{\mathrm{i}\vec{k}\cdot\vec{r}} \tag{2.33}$$
$$\vec{H}_\omega(\vec{r}) = \vec{H}_{\vec{k}n}(\vec{r}) = \vec{v}_{\vec{k}n}(\vec{r})e^{\mathrm{i}\vec{k}\cdot\vec{r}}\,. \tag{2.34}$$

$\vec{u}_{\vec{k}n}$ and $\vec{v}_{\vec{k}n}$ are periodic vectorial functions which are characterized by the wave vector $\vec{k}$ and the band index $n$ and satisfy the equations

$$\vec{u}_{\vec{k}n}(\vec{r}+\vec{a}_i) = \vec{u}_{\vec{k}n}(\vec{r}) \tag{2.35}$$
$$\vec{v}_{\vec{k}n}(\vec{r}+\vec{a}_i) = \vec{v}_{\vec{k}n}(\vec{r}) \quad ; i = 1,2,3\,. \tag{2.36}$$

The periodic "potential" in photonic crystals originates from the periodic dielectric function $\varepsilon(\vec{r})$,

$$\varepsilon(\vec{r}) = \varepsilon(\vec{r}+\vec{a}_i)\,, \tag{2.37}$$

where $\vec{a}_i$ are the elementary lattice vectors of the photonic crystal. Next, we adopt the concept of reciprocal lattice vectors $\vec{G}$:

$$\vec{G} = l_1\vec{b}_1 + l_2\vec{b}_2 + l_3\vec{b}_3 \tag{2.38}$$

$$\vec{a}_i \cdot \vec{b}_j = 2\pi\delta_{ij}\,. \tag{2.39}$$

$l_i$ correspond to arbitrary integers and $\delta_{ij}$ to the Kronecker delta.

Because of the spatial periodicity of the functions, they can be expanded in Fourier series:

$$\vec{E}_{\vec{k}n}(\vec{r}) = \sum_{\vec{G}} \vec{E}_{\vec{k}n}(\vec{G}) \cdot \exp(\mathrm{i}(\vec{k}+\vec{G})\cdot\vec{r}) \tag{2.40}$$

$$\vec{H}_{\vec{k}n}(\vec{r}) = \sum_{\vec{G}} \vec{H}_{\vec{k}n}(\vec{G}) \cdot \exp(\mathrm{i}(\vec{k}+\vec{G})\cdot\vec{r}) \tag{2.41}$$

$$\frac{1}{\varepsilon(\vec{r})} = \sum_{\vec{G}} \kappa(\vec{G}) \cdot \exp(\mathrm{i}\vec{G}\cdot\vec{r})\,. \tag{2.42}$$

These expansions (2.40)–(2.42) are inserted in the master equations (2.31) and (2.32) which results in

$$-\sum_{\vec{G}'} \kappa(\vec{G}-\vec{G}')(\vec{k}+\vec{G}) \times \left\{(\vec{k}+\vec{G}') \times \vec{H}_{\vec{k}n}(\vec{G}')\right\} = \left(\frac{\omega_{\vec{k}n}}{c_0}\right)^2 \vec{H}_{\vec{k}n}(\vec{G}) \tag{2.43}$$

$$-\sum_{\vec{G}'} \kappa(\vec{G}-\vec{G}')(\vec{k}+\vec{G}') \times \left\{(\vec{k}+\vec{G}') \times \vec{E}_{\vec{k}n}(\vec{G}')\right\} = \left(\frac{\omega_{\vec{k}n}}{c_0}\right)^2 \vec{E}_{\vec{k}n}(\vec{G})\,, \tag{2.44}$$

where $\omega_{\vec{k}n}$ denotes the eigenangular frequency of the fields.

These are the sets of equations that are solved numerically to derive the dispersion relation of the eigenmodes — the *photonic band structure*. These band structures can been viewed as an analogue to the electronic band structure, i.e., a lot of known properties can be transfered from solid state physics to photonics.

In the early days, the field of photonic crystals was mainly driven by excellent theoretical work. Experimentalists had to deal with the high demands on the fabrication side — for the communication market, the properties of the fabricated structures should be at the near-infrared spectral range (1.55 µm) leading to lattice constants well below 1 µm. Fabrications methods are discussed in the context of artificial chiral materials in chapter 3.

### 2.3.2. Basic properties of photonic crystals

Photonic crystals allow to design the electromagnetic vacuum. The density of states of the radiation field $D(w)$ is the parameter which is accessible by tailoring the dielectric structure in man-made crystals. As derived in the previous section, photonic

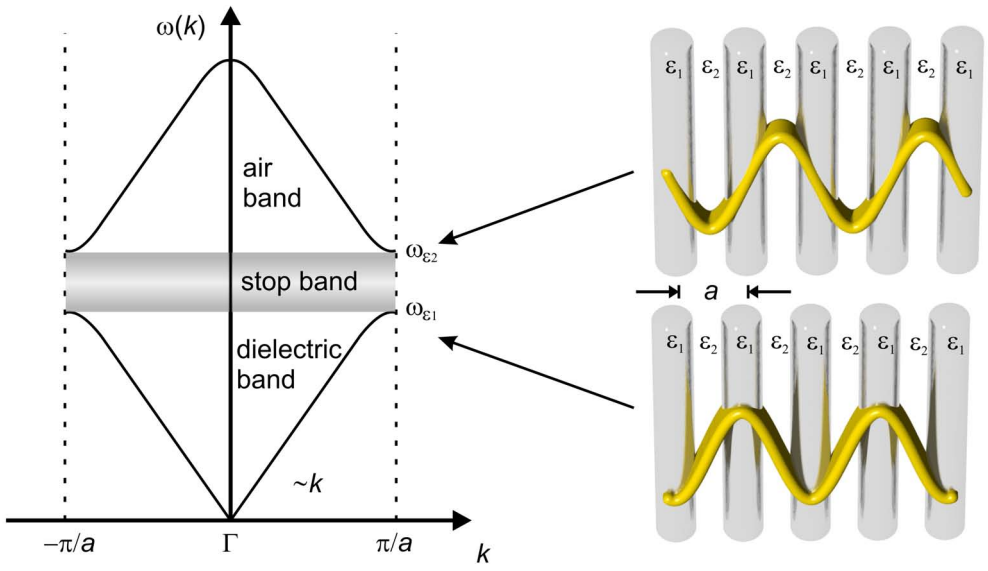


Figure 2.9: The first bands of the dispersion relation $\omega(k)$ of a 1D Bragg stack. The gray region corresponds to the reflection band (or stop band). At the edge of the Brillouin zone, the group velocity is zero and standing waves occur leading to higher or lower energy of the modes.

crystals provide a dispersion relation $\omega_{\vec{k}n}$ for photons, in strong analogy to semiconductors. This band structure depends on the periodic dielectric constant $\varepsilon(\vec{r})$, hence, will change for different designs. Certainly, the dimensionality of the photonic structures also plays a crucial role. Photonic crystals can be considered as "semiconductors for light" and possess a variety of fascinating properties presented in the next sections.

### Photonic band gap

Lord Rayleigh (1842–1919) was the first who theoretically studied dielectric multilayer systems in 1887 [53]. These 1D photonic crystals are often called distributed Bragg reflectors, having a reflection band at

$$2na = m\lambda\,, \quad m \in \mathbb{Z} \tag{2.45}$$

where $a$ the lattice constant, $n$ the effective refractive index of the 1D system, and $\lambda$ the wavelength of the electromagnetic radiation.

The dispersion relation can be easily derived for the 1D case [51]. In Fig. 2.9, a sketch of the first two bands of $\omega(k)$ is shown. Reflection occurs at the gray spectral region, which is also called *stop band*. Light waves in this region will exponentially decay when entering the photonic crystal. In an easy-to-understand description, the standing waves at the edge of the Brillouin zone peak in the high-index material $\varepsilon_1$

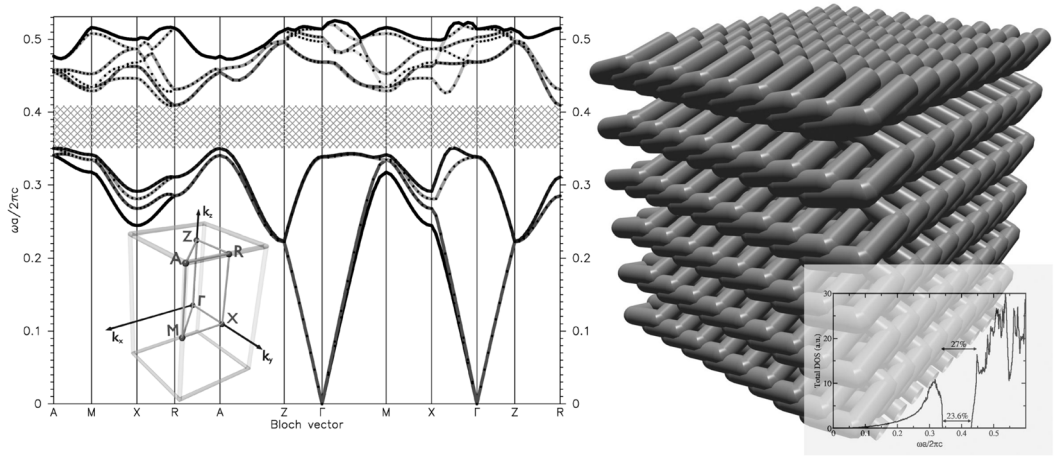


Figure 2.10: The square-spiral architecture is depicted as an example for photonic-band-gap materials. A complete gap with gap-to-midgap ratio of 15.2% (23.6%) for the direct (inverted) structure has been predicted (assumed dielectric contrast $\Delta\varepsilon = 11.9$). Reproduced with permission from reference [54].

or in the low-index material $\varepsilon_2$, leading to a lower or higher energy. The width of the stop band is obviously a function of the dielectric contrast ($\Delta\varepsilon = \varepsilon_2 - \varepsilon_1$).

However, full control over the dispersion relation can only be achieved by tailored 3D photonic crystals. 3D architectures can possess a *complete photonic band gap* — a frequency region without photonic states for *all* crystal directions. Its bandwidth correlates with the dielectric contrast that has to be relatively high. Light in this spectral band is not able to enter the crystal, as there are no photonic states available.

Over the years, several photonic-band-gap materials have been proposed. The famous layer-by-layer woodpile structure [55] (necessary index contrast $\Delta n \geq 1.9$) or the circular-spiral structure are just two examples of several architectures [56]. In Fig. 2.10, Sajeev John's proposal of square spirals is illustrated [54]. This design consists of helices with a square cross section arranged on a tetragonal lattice. The band structure has been calculated with the plane wave expansion method (just explained in the previous section) and is depicted in Fig. 2.10. The dispersion $\omega(k)$ is given in units of the lattice constant $a$ and plotted over the relevant Bloch vectors. The gap-to-midgap ratio is 15.2% (23.6%) for the direct (inverted) structure made of silicon. We have picked that example because of the chirality of the square-spiral structure. Importantly, the complete photonic band gap is not depending on the polarization. The handedness of the crystals has *so far* no influence on the photonic gap.

### Band structure calculations

Today, commercial or free simulation software is often used to compare experiments and theory. A prominent example is the MIT Photonic-Bands (MPB) package. In 2001, these block-iterative algorithms for computing eigenstates for periodic dielectric systems using a plane-wave basis was published by Johnson and Joannopoulos [57]. The authors provide a free program code on the web and many groups use it to describe and design their structures. Photonic band gaps can be predicted with band structure calculations and the mode profile can give a good hint for the functionality of the investigated structure. However, there is still a huge demand for new theoretical work. High-index structures or dispersive materials like metals are very hard to handle numerically and the convergence of results has to be approved.

### Interfaces of photonic crystals

If one is interested in a real transmittance experiment with finite photonic crystals, interfaces must always be taken into account. Interfaces give rise to refraction, diffraction, and to surface waves. The symmetry of the Bloch modes is determining if a wave can couple into the crystal or not.

Therefore, calculating the band structure alone is not sufficient for the comparison with experiments. Fortunately, there is a variety of approaches allowing for calculation of transmittance and reflectance spectra of finite structures. In this thesis, a scattering-matrix approach has been used (explained later in section 5.2).

### Scaling law

The band structure is usually given in units of the lattice constant $a$. This is because Maxwell's equations are scalable. The proof can be performed via a relatively simple scale transformation [51].

The scaling law tells us that the properties of a photonic crystal with a lattice constant of 1 mm are essentially the same compared to the structure with lattice constant of 1 µm but on a different frequency scale. Experimentally, the scaling is very helpful. Proof-of-principle experiments can clearly be easier realized on larger scales.

Note that materials are always dispersive and, strictly speaking, the scaling law might not be applicable. However, there are methods to calculate band structures with frequency-dependent dielectric constants [51].

### Slow light

As in the case of semiconductors, the group velocity of the eigenmodes can be derived from the dispersion relation. The group velocity is given by the slope

$$\vec{v}_g = \frac{\partial \omega}{\partial \vec{k}} \,. \tag{2.46}$$

A small group velocity can lead to large interaction times between the radiation modes and the matter system. Optical processes can be enhanced, e.g., stimulated emission or nonlinear interactions.

### Time reversal symmetry

The wave equations are invariant if one changes the sign of the time variable. This leads to time reversal symmetry of the dispersion relation:

$$\omega_{-\vec{k}n} = \omega_{\vec{k}n} \,. \tag{2.47}$$

This fact even holds true if the photonic crystal lacks inversion symmetry. This is an important statement for chiral photonic crystals, properties of which are distinct from non-reciprocal effects (e.g., the Faraday effect). Optical isolation in Faraday isolators is only possible because of the applied magnetic field.[10]

### Defects

Semiconductors are doped to tailor their properties. To achieve functionality in a photonic-band-gap material, defects can be introduced. Defects may permit localized modes to exist if they are properly designed to have frequencies inside the photonic band gap.

For example, point defects can generate a cavity with high $Q$-factors. The quality factor $Q$ of the defect mode is defined as:

$$Q = \frac{\text{central frequency}}{\text{full width half maximum}} = \frac{\omega_0}{\Delta\omega} \,. \tag{2.48}$$

Higher $Q$ indicates a lower rate of energy loss relative to the stored energy of the oscillator, i.e., light is trapped in the gap. However, well-chosen (line-)defects can guide the light through the crystal. 90° bends in (2D) photonic crystal waveguides are possible with remarkable 98% transmittance [58].

Defects have to be properly designed, and the input and output to photonic-band-gap materials (especially in 3D) are still very challenging tasks. Nevertheless, from a theoretical point of view, 3D photonic crystals are a nice playground for new optical technologies. Hopefully, progresses in fabrication techniques will soon allow to realize the most promising theoretical proposals.

[10] Reciprocity is discussed again in chapter 3.

### Examples of 1D, 2D, and 3D photonic crystals

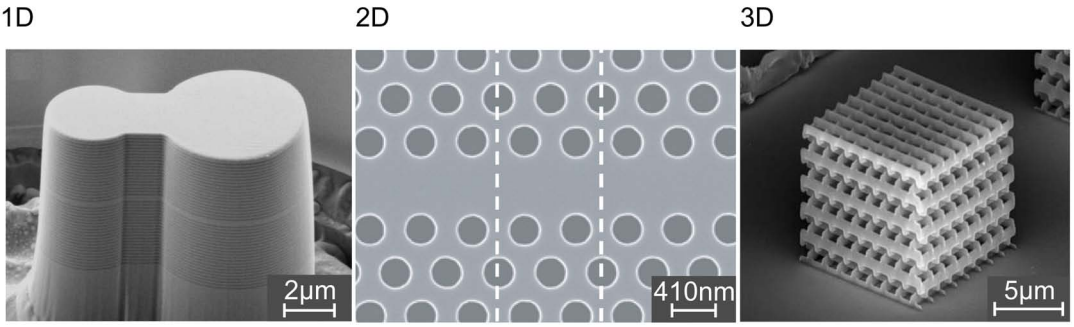


Figure 2.11: Experimental realizations of 1D, 2D, and 3D photonic crystals (corresponding to Fig. 2.8). The 1D example is a coupled micropillar Bragg cavity system which has been realized experimentally by means of focused-ion-beam cutting [59]. The 2D case is exemplified by a high-Q nanocavity structure fabricated by using electron-beam lithography and subsequent etching [60]. The woodpile structure is a prominent example of 3D photonic crystals [61]. Replicated in high-index dielectrics, the woodpile structure can possess a complete photonic band gap. Reproduced with permission from given references.

In recent years, fabrication methods have become more and more advanced. In chapter 3, we want to give an overview of fabrication methods capable to realize chiral nanostructures. However, in Fig. 2.11, we show one fabricated sample of each crystal class.

The group of Prof. Kalt in Karlsruhe made use of 1D photonic crystals, also known as distributed Bragg reflectors [59]. The alternating layers of AlAs (81.6 nm, dark layer) and GaAs (68.4 nm, bright layer) are disturbed by a $\lambda$-cavity (273 nm) with quantum dots. Molecular beam epitaxy techniques allow for this precision in layer thickness. In combination with FIB cutting, the group could fabricate successfully coupled pillar structures and study spectroscopically the coupling behavior in these systems.

In Kyoto, the group of Prof. Noda has fabricated 2D photonic crystals employing a silicon-on-insulator ($SiO_2$) material system [60]. The photonic-crystal slab is produced by a combination of electron-beam lithography and plasma etching. With a lattice constant of around 400 nm, the group was able to achieve a cavity quality factor of 600,000 at around 1.55 µm wavelength. The proposal of this ultra-high-Q photonic double-heterostructure nanocavity is widely used ever since.

Our group in Karlsruhe has fabricated 3D photonic crystals using direct laser writing (DLW). This versatile fabrication technique allows for arbitrary 3D structuring and is described in detail in chapter 4. The structure in Fig. 2.11 shows the well-known woodpile structure. These polymeric templates can be replicated in silicon by employing

an atomic-layer-depostion and a subsequent chemical-vapor-deposition process [62]. Woodpile structures made of silicon can possess a complete photonic band gap.

### Conclusions

The field of photonic crystals has grown and an impressive progress in the fabrication methods has been achieved. Theoretical understanding and computations have led to remarkable advances. Moreover, concepts and methods are transfered and widely used in different departments. Recent review articles give more insight in this exciting field of photonic nanostructures [50]. In the next chapter, we discuss a very interesting subgroup of photonic materials, namely chiral photonic nanostructures.

# 3. Photonic nanostructures with a twist

Biological systems are using nanometer-scale architectures to produce striking optical effects since millions of years [63]. In comparison, the history of man-made structures is short. A. J. C. Bose fabricated one of the first artificial or synthetic chiral materials by twisting parallel fibers of jute. In 1898, he reported on the "rotation of plane of polarization of electric waves by a twisted structure" [9].

Today, modern micro- and nanofabrication methods, advanced chemistry of chiral molecules, and theoretical understanding contribute to a rapidly evolving research topic — photonic nanostructures with a twist. The field is driven by observations of strong optical activity and circular dichroism [10]. Moreover, the possibility to achieve negative refraction [64, 65] or other unusual properties has led to a flourishing and dynamic field in photonics.

In this chapter, we introduce concepts and methods for architectures with a handedness on sub-micron scale. Structural color in biological systems is a very appealing starting point. Later in this thesis, we will give a new twist to "nature's solutions" and fabricate artificial chiral nanostructures mimicking and improving these "evolutionary optics" (compare chapter 6).

In section 3.2, a specific chemical system is presented; the *blue phase* of cholesteric liquid crystals that has been the inspiration for our results in chapter 7.

Last but not least, a short overview of artificial chiral structures is given in order to draw comparisons later on. Furthermore, possible fabrication methods and applications are discussed.

## 3.1. Structural color in nature

Nature is very colorful. Pigments and bioluminescence have long received scientific attention. However, *structural* coloration in biological systems can also be origin of iridescence in nature. The evolution of structural color escalated contemporaneously with the evolution of animal eyes in cambrian age (more than 500 million years ago).

Scientific studies of structural color have been around since Robert Hooke's famous book "Micrographia" (1665) [66]. Recently, modern imaging techniques have led to amazing insights in nature's way to either camouflage or to irradiate, reviewed in references [63, 66–69].

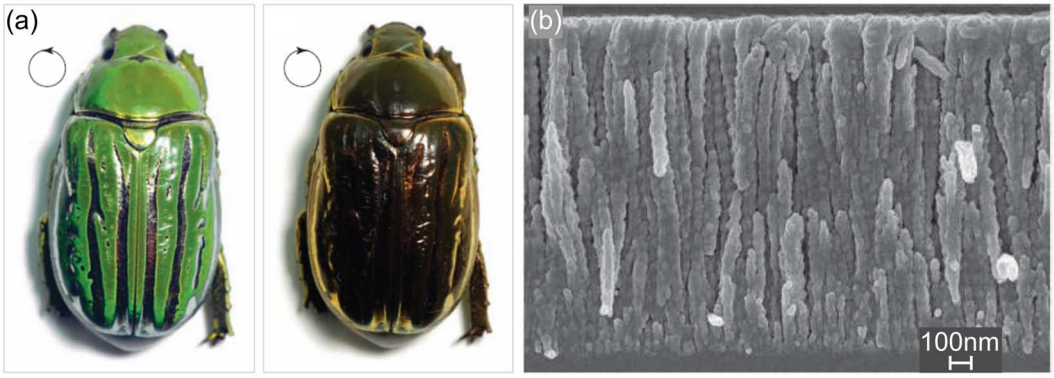


Figure 3.1: (a) Photographs of the beetle *Plusiotis gloriosa*. Left-hand side: Observed with unpolarized or left-handed light, the beetle shines in a brilliant green. Right-hand side: Right-handed light is not reflected. (b) Scanning electron micrograph of the left-handed chiral nanostructure responsible for the reflection. Reproduced with permission from reference [5] and [71].

Natural photonic structures are providing inspiration for technological applications: One can either use the biological system themselves as templates [70] or apply engineering methods to make direct analogues [5]. The variety of natural functional nanostructures is rather impressive — 1D multilayer reflectors, 2D diffraction gratings, or even 3D photonic-crystal structures have been evolved naturally.

In this thesis, we are devoted to chirality in optics and photonics. It is flabbergasting that flora and fauna provide chiral building blocks as blueprints. Especially animal structures show potential as functional chiral optics. In flora, however, there are fruits that shine blue because of a 1D multilayer photonic crystals [72]. Moreover, cell walls in plants are made of cellulose (50% of their mass). Cellulose is an optical active molecule and is able to form parallel microfibrils. In a lot of cell walls a helicoidal arrangement of these fibrils on sub-micron scale (comparable to liquid crystals) is mechanically supporting tissues [67].

A very similar helical structure is depicted in Fig. 3.1, where the scarab *Plusiotis gloriosa* is shown [71]. The same beetle has been photographed with different polarization filters. A green beetle can be observed when using unpolarized or left-circularly polarized light. The green color is lost if right-handed light is impinging. Thus, this scarab is a chiral reflector. A scanning electron micrograph reveals the substructure, which is responsible for the reflection [5, 71] — a twisted helical nanostructure. The sense of rotation of the structure is left-handed leading to reflection of left-handed light. There are even beetles which incorporate a birefringent layer in between two different chiral reflectors [73]. This layer acts as half-wave plate and converts left-handed to right-handed light (and vice versa).

Our designs of chiral photonic crystals presented later in chapter 6 can be viewed as engineered complements of these biological systems. “Biomimetics” offers fascinating

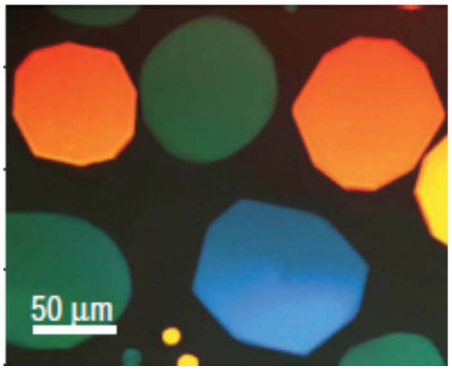


Figure 3.2: Microscopic view on liquid crystals in blue phase II. Due to a 3D arrangement of the chiral molecules, Bragg reflections occur and nearly create an artistic impression. The ability to alter the optical properties of blue-phase liquid crystals by an electric field give rise to industrial applications. Reproduced with permission from reference [75].

possibilities to transfer nature's solution into man-made functional nanostructures. In the next section, the chemical system of the liquid crystal *blue phase* is introduced that are relevant for our results in chapter 7.

## 3.2. Blue phase of liquid crystals

Liquid crystals are a mesophase between liquids and crystals and have been discovered by Friedrich Reinitzer (1857–1927) and Otto Lehmann (1855–1922) in 1888 [39]. They consist of highly anisotropic molecules, which arrange to minimize their free energy. This mesophase carries crystal characteristics like birefringence but still flows like a liquid. A vast variety of thermodynamical stable phases are distinguishable, e.g., nematic, cholesteric, or smectic.[1]

Liquid crystal displays, for example in TV sets and laptops, are known from everyday life. The cigar-shaped molecules can be aligned by an electric field explaining the industrial success story of the display technique. In the most simple liquid crystal display, the nematic phase is twisted by 90° in a helical manner, enclosed in between two pre-structured glass slides. Herewith, linear polarization can be rotated by 90°. By applying a voltage, the helix unfolds and, with the help of polarization filters, any gray level can be adjusted.

Here, we want to focus on the liquid crystal *blue phase* (BP). The blue phase is indeed the phase which caught Reinitzer's attention back in 1888. In Fig. 3.2(a), there is a microscopic view on the so-called BPII.

[1] For a comprehensive story about liquid crystals, we refer to textbook [74].

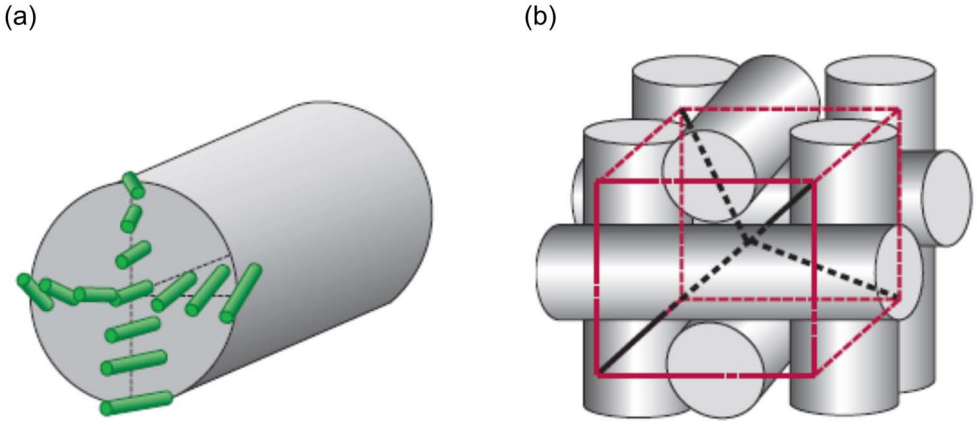


Figure 3.3: The simple cubic BPII. (a) In a narrow temperature range, the anisotropic molecules arrange in double-twist tubes. (b) The tubes align according to thermodynamics, i.e., the three nearest tubes form the corner (here right-handed). As a result, the BPII exhibits a simple cubic symmetry. Reproduced with permission from reference [75].

Over a narrow temperature range ($\leq 2°$), highly chiral liquid crystals can arrange in 3D cubic lattices [75–78]. With characteristic lattice constants on the order of the wavelength of visible light, they give rise to vivid specular reflections (obviously not only blue light is reflected). The BPII, in particular, is a simple cubic arrangement to be seen schematically in Fig. 3.3. Thermodynamically, it is favorable for the chemical system to built up double-twist tubes. Besides the intrinsic chirality of the double-twisted molecules, a certain handedness results along the tube axis. In Fig. 3.3(a), the double-twist of the molecules is right-handed, however, the resulting helix along the tube axis is left-handed. Just try to screw all green molecules into the plane — a left turn is necessary.

The tubes are stacked to a simple cubic unit cell. Three double-twist tubes can, in principle, form a left- or right-handed coordinate system, also called corner [75, 76]. It can be calculated that the free energy is minimized if the corner and the helix along the tube have opposite handedness [76].[2] The lattice constants of these cubic (photonic) crystals are on the order of several hundred nanometers and tunable by an electric field.

Recently, blue-phase liquid crystals have been stabilized to extend the temperature range [77, 78] making them interesting for the industrial market.[3]

[2]Please note that the intrinsic handedness of the molecules is the same compared to the corner.
[3]Samsung started developing blue-phase displays with an advanced rate of 240 Hz, and they will presumably be released in 2011.

## 3.3. Artificial chiral materials

With the ability to structure materials on a sub-micron scale, fabricated periodic nanostructures in photonics enable far-reaching control of light propagation and light-matter interaction [50]. Chiral nanostructures enabled research groups to achieve giant optical activity and/or circular dichroism [14–21, 40–44]. The observed chiral-optical effects can be orders of magnitude larger than observed in natural substances, like sugar solutions.

In what follows, we want to give an overview about concepts and methods in the field of artificial chiral materials.

### 3.3.1. Periodic nanostructures for photonics

Nanostructures with lattice constants $a$ on approximately the scale of the wavelength of the interacting light ($\lambda/a \approx 1$) have already been introduced as photonic crystals [50]. The examples previously given in this chapter, the beetle and blue-phase liquid crystals, belong to this class of photonic materials.

Periodic materials with periods of $\lambda/a \gg 1$ are called metamaterials [50]. They allow to tune the *effective* optical material parameters such that qualitative new effects occur. For example, negative refractive index cannot be found in nature but in this rather new material class of metamaterials [64, 65].

Metamaterials turned out to have a huge impact on the optics community, with revolutionary concepts like perfect lenses or invisibility cloaks [79]. However, the term "metamaterial" is already used in a rather broad context and, sometimes, it is hard to draw a borderline between them and photonic crystals. Here, chiral periodic nanostructures are characterized straightforward by their dimensionality.

#### The role of dimensionality

As a reminder: A 3D object is chiral if its image in a plane mirror cannot be brought to coincide with the original. If we extent Kelvin's definition of chirality to 1D and 2D, a comparison with truly 3D chirality would look like Fig. 3.4.

First, in 1D space, two antiparallel vectors are chiral because it is not possible to superimpose them by translation [80]. Note that angles and rotations are not defined in 1D, but directions are. Nevertheless, we confess that 1D chiral systems are somehow "uncommon".

In 2D, the original and its mirror image are called chiral if they are not superimposable unless they are lifted from the plane. In a 2D world, this is impossible. Consequently, when applying the 2D parity operator only one spatial coordinate changes $(x,y) \rightarrow (x, -y)$. L-shaped objects are typical examples for 2D chirality.

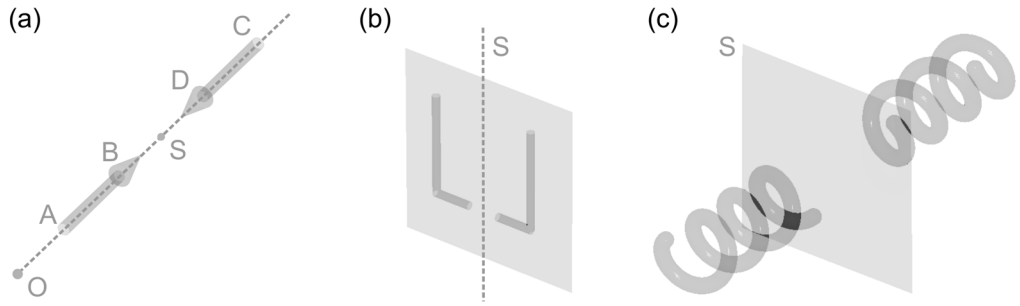


Figure 3.4: 1D, 2D, and 3D chirality. (a) An anti-parallel vector is a chiral object in 1D space. (b) L-shape structures are common examples for 2D chirality. (c) Left-handed helical structures are not superimposable on right-handed helices. Adapted from [80].

However, 1D chiral objects are *a*chiral in a 2D and 3D world. 2D chiral objects are *a*chiral in a 3D world because one can simply turn them around by 180° and match the original. The same holds true for 3D chiral objects in 4D space.[4]

Why is the dimensionality important anyhow?

In recent years, a considerable amount of work has been devoted to planar chirality. Since the vast majority of plano-chiral materials have been fabricated on a glass substrate, they are often called quasi-planar (see also fabrication methods 3.3.2). In contrast to the case of 3D chirality, the "handedness" of a plano-chiral object (without a substrate) changes when viewed from opposite directions with respect to the axis of chirality. In the 2D case, this direction is normal to the plane of the chiral building blocks. Since a helix does not change its handedness, optical phenomena like optical activity do not depend on the direction of the impinging light. In this case, Maxwell's equations are invariant concerning the reversal of time, even though chiral structures lack inversion symmetry (compare to section 2.3).

The change of the "handedness" in plano-chiral objects suggests that electromagnetic phenomena analogous to the Faraday effect would be possible. It has been reported that quasi-planar materials break time-reversal symmetry [81]. Ever since the group of Prof. Zheludev has been published this work, the possibility of non-reciprocity in these structures has been controversially discussed.

[4]For a study of chirality in multi-dimensional space, we refer the reader to the article [80].

### (Non-)reciprocity of artificial chiral materials

In optics, polarization elements are often classified as reciprocal or non-reciprocal. Reciprocity depends on whether their effect on the polarization state of the transmitted light is the same or different for light propagating in the opposite direction. The vast majority of optics is reciprocal.

Absence of reciprocity in photonics is rare. Inelastic light scattering and nonlinear frequency changing in spatially asymmetric media can lead to non-reciprocal optics [82]. Furthermore, magneto-optical rotation of the plane of polarization is depending on the propagation direction. Faraday isolators might be the best known non-reciprocal optical devices. The magnetic field is applied parallel to the propagation direction of light leading to different traveling speeds of circular polarization for forward and backward direction (see section 2.2.2).

This behavior manifests in an asymmetric dielectric tensor with off-diagonal elements proportional to the magnetic field (applied in $z$-direction) [83]:

$$\underline{\underline{\epsilon}} = \begin{pmatrix} \epsilon_a & +i\epsilon_2 & 0 \\ -i\epsilon_2 & \epsilon_b & 0 \\ 0 & 0 & \epsilon_c \end{pmatrix} + \text{anisotropic terms}\,. \tag{3.1}$$

Importantly, $\epsilon_2$ is an odd function of the magnetic field $\vec{H}$ (or the magnetization $\vec{M}$). If the field is applied parallel to the forward direction, the dielectric tensor certainly leads to different propagation speed of light when compared to the backward direction (antiparallel orientation of the field). This results in non-reciprocal behavior from Faraday media. As a consequence, magneto-optical rotation is distinct from natural optical activity in (Pasteur) media that belongs to the wide range of reciprocal effects [82, 83]. Magneto-optical rotation breaks time-reversal symmetry. In contrast, natural optical active substances only break parity symmetry (without an applied magnetic field).

Controversy arose whether plano-chiral material were non-reciprocal (without an external magnetic field) because they change their sense of rotation when seen from the one side of the substrate or the other. In 2009, Tretyakov *et al.* convincingly showed in reference [84] that any 2D system with metal or dielectric inclusions of any shape is reciprocal. In 2D, the cross-coupling term due to the chirality parameter between the electric and magnetic field vanishes. Hence, there is no optical activity for normal incident plane waves in plano-chiral objects. By using a scattering-matrix approach, Tretyakov could further show that the optical activity reported by several different groups was due to coupling with the substrate. The influence of the substrate has been discussed by other groups as well [85, 86]. Essentially, the substrate turns the chirality of the system from 2D (planar) to 3D.

#### Asymmetric transmission

An asymmetric transmission measurement is *not* a sufficient proof for an optical device to be non-reciprocal. Take a simple counter example: A quarter-wave plate followed by a linear polarizer. Everybody will agree that both elements are reciprocal optics. However, linear polarization can be measured to have different transmittances impinging from one direction or the other.

Asymmetric transmission is still a rather mind-boggling optical effect and can also be observed in quasi-planar chiral materials [87]. However, at the moment, the route to chirality in nanophotonics is mainly driven by the design and fabrication of real 3D architectures with high potential for applications.

### 3.3.2. Fabrication methods

Chirality in nanophotonics relies on the possibility to fabricate optics with a nanoscaled twist. Fortunately, the field of optics and photonics has seen tremendous progress of modern fabrication methods throughout the last decades (e.g., thin-film technologies borrowed from electronics). Several techniques that are able to produce the necessary twist will be presented next.

#### Self-assembly of the liquid crystal blue phase

Blue-phase liquid crystals are self-assembled systems. As a mesophase between crystals and liquids, their configuration is strongly dependent on temperature. Cooling down from the isotropic phase to the chiral nematic phase can lead to three thermodynamically stable blue phases (BPI, BPII, and BPIII). Liquid crystals are commercially available for a long time. Recently, special mixtures of liquid crystals [78] have proven to be stable over a wide temperature range (16°C–60°C) making blue-phase LC displays interesting for applications.[5]

#### Chiral fiber gratings

In 2004, Kopp *et al.* published a report on chiral fiber gratings [89]. The authors twist usual glass optical fibers while heating them up in a miniature oven. Their optical properties depend strongly on the pitch of the fibers, which have recently become commercially available with sub-micron accuracy of the feature sizes.

[5] We note that self-assembly mechanisms can produce various chiral systems (e.g., chiral block copolymers [88] or ZnO helices).

### Glancing-angle deposition

Glancing-angle deposition (GLAD) is a combination of oblique thin-film vacuum deposition and computer controlled motion of a pre-structured substrate [90, 91]. Without substrate rotation, shadow evaporation leads to growth of columns, which point to the material flux (birefringent materials result). In combination with a rotating substrate, separated nanoscaled helical structures can be deposited. The lattice constants are a function of the deposition angle, the spacing of growth seeds, and rotation speed. Materials that can be deposited with physical vapor deposition are also suitable for GLAD, and the complete substrate is structured at a time. Nevertheless, pre-patterning of the entire substrate is necessary and the shadow evaporation technique clearly leads to constrictions in possible structural designs.

### Holography

Holographic laser lithography allows for a greater variety of structures. Here, the idea is to create 3D interference patterns to expose a photosensitive material, which is developed afterward. Intensity profiles with a chiral basis and even spirals (helices) have been calculated. Corresponding fabricated polymeric templates were suffering of large distortions due to experimental complexity and photoresist shrinkage [16, 92]. In principle, holography enables fast large-area fabrication but with the *same* intensity pattern on the entire substrate. Since the experimental adjustment of laser intensity and phase is a complicated task, holography lacks of flexibility.

### Electron-beam lithography

Compared to laser holography, electron-beam lithography is a flexible method for rapid prototyping. Feature sizes well below 50 nm are achievable by using an electron beam to expose a thin polymeric resist on a substrate (e.g., 20 nm of PMMA). Evaporation of dielectrics or metals and subsequent lift-off of the polymer is a common process. 2D chiral structures like L-shapes are easily accessible with electron-beam lithography. To enhance chiral effects, a planarization process with a spin-on dielectric has recently been employed for nanostructures [93, 94]. Multiple *different* layers can be stacked on top of each other leading to 3D chirality. This serial process is very time consuming, however, it has been demonstrated with high alignment accuracy. Very large optical activity has been measured, e.g., for twisted crosses [94].

### Direct writing techniques

Direct laser writing is a versatile and flexible method for true 3D lithography [95]. We will explain pros and cons of this technique in the following chapter 4 since it has been employed as fabrication method in this thesis.

### 3.3.3. Applications

Research in applied physics is intended for a particular technological or practical use. Hence, possible applications are often the motivation for physicists working in the field. With their sensibility to the polarization state of light, chiral nanostructures are potential candidates for several future uses.

#### Photonic-band-gap materials

Photonic crystal research is motivated by the revolutionary concept to design the density of photonic states in 3D photonic-band-gap materials. To gain full control of the flow of light, several architectures with a complete band gap have been proposed. In this context, circular-spiral and square-spiral photonic crystals [14, 41] have been introduced as chiral designs with a full band gap if the refractive index contrast is sufficiently high. Square spirals made of silicon, which come close to the original proposal, have been fabricated by using GLAD [15]. However, functionality comes with incorporated defects. For example, Sajeev John theoretically proposed a (chiral) 3D-2D-3D photonic crystal heterostructure as single-mode, lossless, optical micro-circuitry for integrated optics [43]. All optical micro-circuitry based on light localization in a photonic-band-gap microchip is definitely one of the central goals in the field of photonics [50].[6]

#### Circular polarizers

Theoretically proposed by Prof. Chan, a *polarization stop band* along the helical axis of circular-spiral photonic crystals can occur — a frequency region without photonic states for *one* of the orthogonal circular polarizations [18]. The authors have calculated the band structure and transmittance/reflectance spectra for high-index-contrast spirals. The calculations have characterized the new design as chiral reflector. Left-handed (right-handed) spirals reflect left circular (right circular) polarization. The analysis of the eigenmodes in the gap yields them being predominantly left-handed (right-handed) for a right-handed (left-handed) spiral, leading to high transmittance for left circular (right circular) polarization and rendering the architecture as circular polarization filter. Importantly, circular stop bands also appear in polymeric structures [19].[7]

[6] Prof. Misawa's group has fabricated defective spiral templates in low-index contrast polymers using DLW [17]. Yet, the incorporated waveguides were non-functional.

[7] We note that other chiral structures leading to some form of polarization stop band have also been realized experimentally using cholesteric liquid crystal structures [74], vacuum deposition [90, 91], and chiral optical fibers [89].

### "Poor-man's" optical isolators

An optical isolator is an optical component allowing for the transmission of light in only one direction. It is typically used to prevent unwanted feedback into an optical oscillator, such as a laser cavity. One can consult chiral nanostructures with asymmetric transmittance to serve as "poor-man's" optical isolators for one circular polarization. A back-reflecting mirror (e.g., the output coupler of a laser cavity) changes the sign of the polarization and cannot pass the isolator on the way back. As we have fabricated a "poor-man's" optical isolator, we discuss results in chapter 6.

### Sensors

The porosity of chiral photonic crystals makes them attractive for optical sensing. Detecting and quantifying various chemical and biological fluids or gases is made possible by exploring the shift of the polarization stop band. By introducing a planar defect or a phase defect, one could also detect the shift of the defect mode [42].

A very interesting application could be the sensing of chiral molecules. If the handedness of the chiral nanostructures interfered with the chiral molecules, such a device would serve as chromatograph.

### Chiral negative-index metamaterials

Sir John Pendry proposed a chiral route to negative refraction [44]. The theoretical concept demands an isotropic chiral metamaterial combined with an electric resonance. Pendry has shown that the introduction of an additional chiral resonance leads to negative refraction of one polarization. To date, microwave experiments [64,65] have been demonstrated but the concept waits for realization with nanoscaled metamaterials.

### Luminescent and lasing devices

Band-edge lasing and defect-mode lasing have been observed in chiral liquid crystals [42]. At the edges of the stop band, standing waves occur and the interaction with, e.g., lasing dyes is increased. For defect modes, the suppression of the density of states is the beneficial factor for lasing action. Corresponding experiments with solid state GLAD samples have been carried out [21]. Because of the chiral eigenmodes of these devices, they emit left circular (right circular) if they are left-handed (right-handed). Clearly, electric pumped lasing with a defined circular polarization can be considered as major future goal for chiral photonic crystals.

### Inverse Faraday effect and magneto-optical effects

The inverse Faraday effect is the magnetization of matter by circularly polarized light. The strength of this magnetization is proportional to the intensity explaining the common use of ultra-fast lasers in literature (e.g., [96]). Chiral photonic crystals and/or metamaterials (e.g., a metal nanohelix) could also lead to very strong magnetization, which might depend on light's handedness.

Recently, magneto-chiral dichroism has been observed [36]. Magneto-chiral dichroism is a link between the broken parity symmetry of chiral objects and the broken time reversal symmetry of the Faraday effect: Absorption of an enantiomorph pair of chiral molecules is different if a magnetic field is applied. Although the effects are supposed to be weak, a ferromagnetic nickel helix might be a candidate to investigate magneto-optical effects.

### Displays

Driven by the display industry, an enormous research effort has been put in the development of new types of liquid crystals [97]. The chiral types are role models for the research on chiral nanostructures since their application as displays has such an immense impact on everyday life.

# 4. Direct laser writing

In this chapter, we introduce direct laser writing (DLW), which can be considered as 3D analogue of planar electron-beam lithography. DLW is based on two-photon absorption in photosensitive materials allowing for the fabrication of arbitrary 3D nanostructures with feature sizes smaller than 100 nm [95, 98, 99]. Computer-aided exposure of a multitude of available photoresists turns DLW to a powerful microfabrication technique for a variety of applications — from photonic nanostructures to scaffolds for biological systems.

In section 4.1, we start by explaining the basic principles of DLW. In the course of this thesis, we have considerably improved the 3D laser lithography system technically and conceptionally. In cooperation with Carl Zeiss AG and Nanoscribe GmbH, an advanced and compact DLW setup has been designed, and several experimental setups have been realized. The features of these advanced lithography systems are discussed in section 4.2.

DLW was successfully employed as fabrication method for 3D chiral photonic crystals (see chapters 6 and 7). Furthermore, we have also collaborated with other students of our group on several other topics, e.g., on photonic metamaterials. Therefore, we show some results from different photoresists and present some possible applications in section 4.3. Finally, we draw conclusions concerning the fabrication of chiral photonic crystals.

## 4.1. Concept of direct laser writing

Simultaneous absorption of two (or more) photons provides 3D resolution in microscopy and lithography. While the concept of two-photon absorption has already been described theoretically by Göppert-Mayer in 1931 [100], the first experimental observation of two-photon excitation in $CaF_2$:$Eu^{2+}$ crystals has been made by Kaiser in 1961 [101], shortly after the invention of the ruby laser. In the early nineties, pioneering experiments on two-photon fluorescence microscopy [102] and 3D optical data storage [103, 104] paved the way to modern 3D lithography systems. It was in 1997, when Maruo *et al.* took the step forward and experimentally demonstrated 3D microfabrication using photopolymers [95] — now known as DLW based on two-photon polymerization.

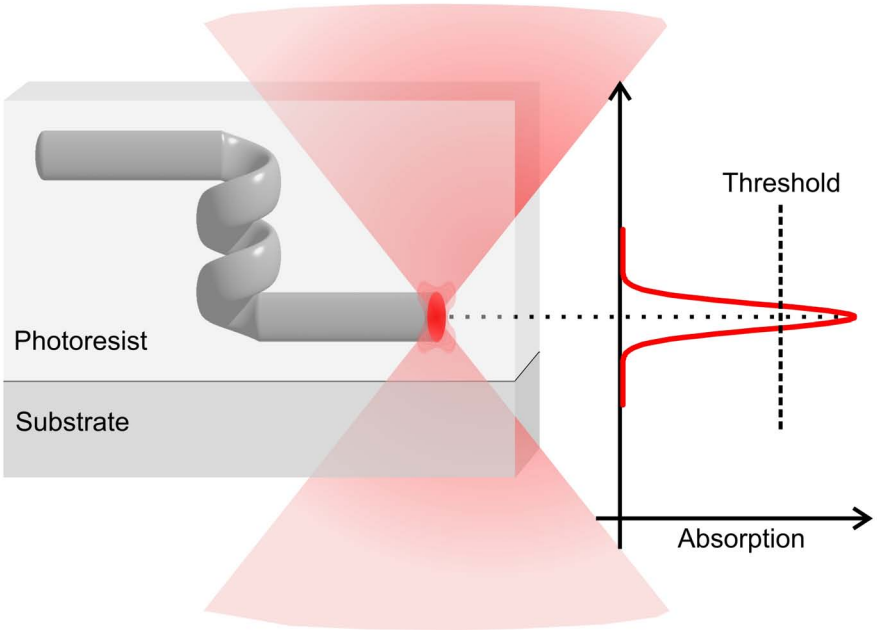


Figure 4.1: A pulsed near-infrared (near-IR) laser is tightly focused into a photoresist sensitive to near-ultraviolet (near-UV) radiation. The resist shows high optical transparency at the laser wavelength, which is usually around 800 nm. Precisely in the focal volume, the photoresist is exposed by two-photon absorption when exceeding the polymerization threshold of the material. Scanning the sample relative to the focus enables the polymerization of arbitrary trajectories.

The general idea is to tightly focus a pulsed near-IR laser into a photoresist, which is sensitive to near-UV radiation while showing very high optical transparency at the laser wavelength, i.e., one-photon absorption is very improbable. However, in the very focal volume, the intensity is high enough to induce the simultaneous absorption of two (or more) photons. By exceeding the exposure threshold of the photosensitive material, a volume pixel (voxel) is exposed and used as writing tip for arbitrary trajectories (illustrated in Fig. 4.1).

The shape of the voxel clearly depends on the intensity distribution in the laser focus, which is determined by several parameters, e.g., the laser mode, the numerical aperture (NA) of the objective, or the refractive-index mismatch between the resist and the immersion system. In our case, we typically focus with a high-NA objective ($\mathrm{NA} = 1.4$) into nearly index-matched photoresists. The focus (voxel) has ellipsoidal shape with an axial aspect ratio of about 2.7 [61], and the size of the exposed volume depends on the laser intensity distribution, i.e., the size does change with the applied laser power.

The number of absorbed photons $n_a$ per molecule per pulse is given by:

$$n_a \approx \frac{p_0^2 \delta}{\tau_p f_p^2} \left( \frac{\mathrm{NA}^2}{2\hbar c \lambda} \right)^2 , \tag{4.1}$$

where $p_0$ corresponds to the time-averaged laser power, $\delta$ to the two-photon-absorption cross section, $\tau_p$ to the laser pulse duration, $f_p$ to the pulse repetition rate, $\lambda$ to the excitation wavelength, $c$ to the speed of light, and $\hbar$ is the Planck quantum [102].

150 fs pulses of a laser source with 100 MHz repetition rate and a central wavelength of about 800 nm are typically focused with a high-NA objective (NA = 1.4) to expose the resist. The laser power is set to few milliwatts. The cross section $\delta$ depends on the wavelength and is on the order of 20 Göppert-Mayer (GM) at 800 nm wavelength for commercial photoinitiator molecules ($1\,\mathrm{GM} = 10^{-58}\,\mathrm{m}^4\,\mathrm{s}$).

Notably, a one-photon absorption process of a UV laser could also expose a voxel. In comparison to one-photon absorption, the great advantage of two-photon microfabrication lies in the strongly reduced proximity effect, i.e., out-of-focus regions are less likely to exceed the threshold of the resist for two-photon absorption. This is of utter importance when complex 3D architectures with intersections or small lattice constants are written.

The voxel is used as writing tip, i.e., by moving the resist relative to the focus, arbitrary trajectories can be exposed. Later on, the polymerization process due to exposure to the laser light leads to a chemical selectivity between unexposed and exposed volumes inside a developer bath (sometimes a post-exposure thermal treatment is necessary). Depending on the photoresist, either exposed (positive-tone resist) or unexposed regions (negative-tone resist) are removed.

Since the introduction of two-photon microfabrication, a flourishing field of research has evolved. The flexibility and resolution makes DLW attractive for fabricating, e.g., 3D photonic structures, scaffolds for biology, or micro- and nanofluidic circuitry. Review articles have recently discussed the materials used for multiphoton fabrication and their applications [98, 99]. The progress has been immense over the last decade turning DLW into a standard of 3D microfabrication.

## 4.2. Advanced setup for three-dimensional laser lithography

In 2007, a cooperation of Carl Zeiss AG and our group was formed in order to improve the laboratory DLW setups that have successfully been developed in our group [61]. Fortunately, this work has led to the foundation of Nanoscribe GmbH, a young spin-off of the Karlsruhe Institute of Technology.

Still better, this cooperation was also a scientific success. In the course of this thesis, we have built up several prototype systems and have extensively used them for a

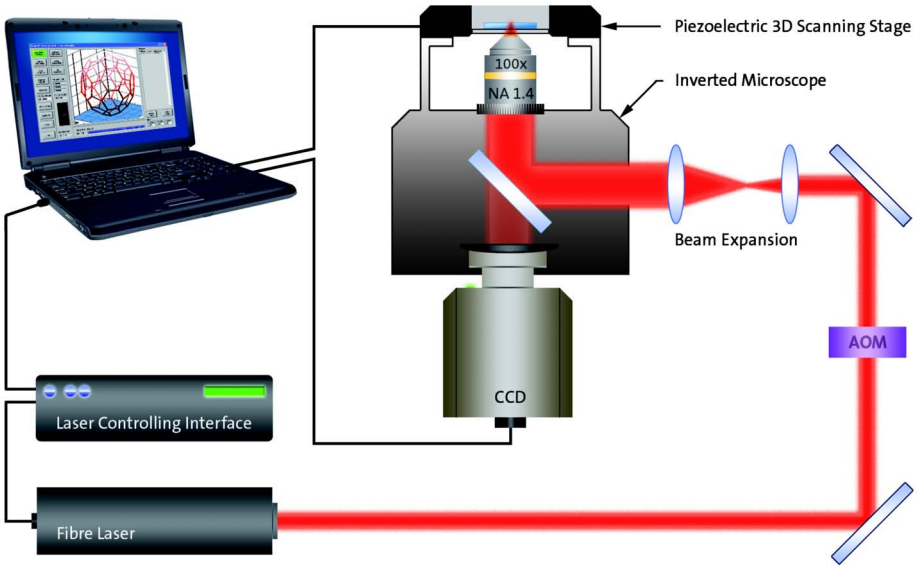


Figure 4.2: Scheme of the advanced setup for 3D laser lithography. This blueprint has been implemented in a compact table-top DLW system (see the photograph 4.3 on the next page).

multitude of scientific projects [40, 105–113]. Here, we present the advanced system that took the reproducibility and automatization to the next level.

### Experimental realization of direct laser writing

The scheme of our DLW setup is shown in Fig. 4.2. A compact frequency-doubled erbium-doped fiber laser at fixed 100 MHz repetition rate and sub-150 fs pulses is used as robust laser source at a central wavelength of 780 nm. The laser power of around 60 mW is attenuated with help of an acousto-optical modulator (AOM). In order to take advantage of the high NA of the objective, the beam has to be expanded before it enters the backport of an inverted microscope. Next, the beam is reflected by a beamsplitter and focused into the resist (NA = 1.4). The beamsplitter is necessary for the use of the CCD camera port enabling observation of the writing process.

*The* key feature of the system is the autofocus. The interface between the substrate and photoresist can be determined exactly and automatically (accuracy $\pm 40$ nm). This is very important to ensure that structures are anchored properly to the substrate. Moreover, a tilt correction is possible being essential for 2D structures and large area structuring. Usually, extensive energy series of the desired structures are programmed. Therefore, the autofocus is also used to account for tilt or drift. Further-

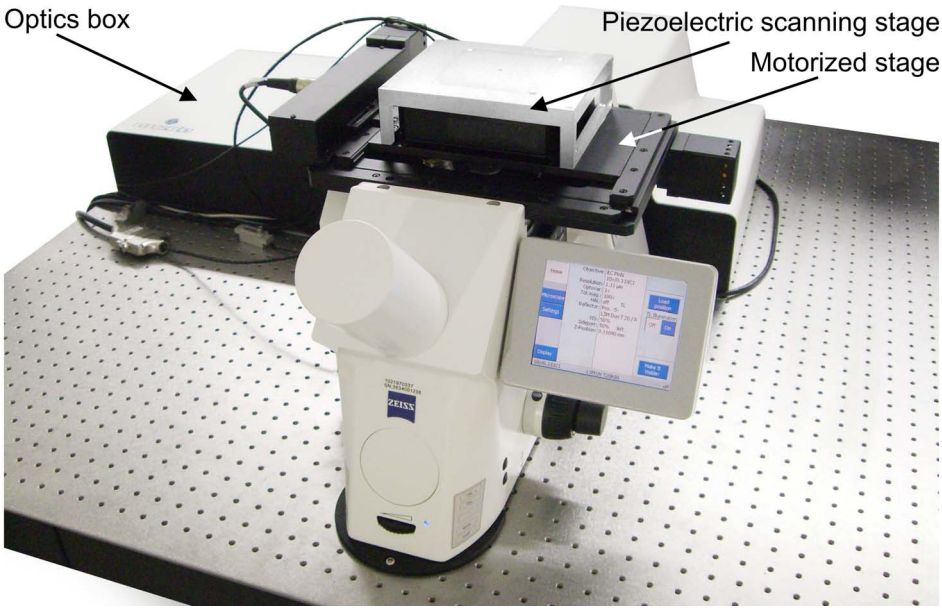


Figure 4.3: Photograph of the DLW setup showing the optics box (hiding all optical components inclusive of the laser) and the inverted microscope. The entire setup fits on a 90 cm×90 cm breadboard. Such a system has been employed for the fabrication of 3D chiral photonic crystals (see results in chapter 6 and 7).

more, the laser power is recalibrated and/or adjusted automatically. All important features and electric components are addressed by a control software.[1]

A photograph of the realized advanced DLW setup is depicted in Fig. 4.3. In the background, there is the optics box which includes the laser and all the optic components necessary to guide the laser light to the inverted microscope (in the foreground). The microscope is modified to ensure laser security class 1, and the stages for positioning are mounted on top of the microscope.

A piezoelectric scanning stage provides the accuracy for patterning the resist with arbitrary 3D trajectories in a volume of 300 µm×300 µm×300 µm. Additionally, a different motorized scanning stage can be moved laterally in an area of 10 cm×13 cm. Using both stages in combination enables fine-structuring with the piezo stage and subsequent stitching of these volumes with the large-area stage.

In order to pattern larger areas without stitching, the motorized scanning stage can also be used for the structuring. In this mode, the third dimension can be addressed by the $z$-drive of the microscope and/or the piezo allowing for 3D patterning with a precision within the specifications of the large-area stage.

[1]The control software has been programmed by Dr. Georg von Freymann.

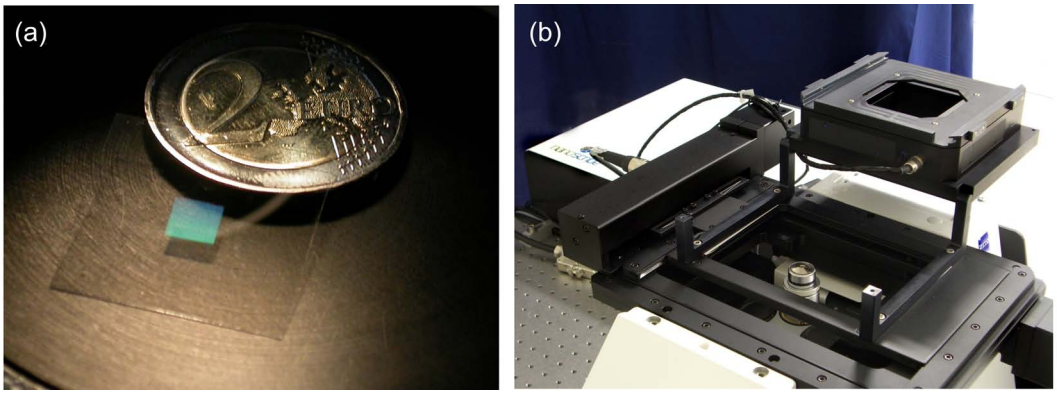


Figure 4.4: (a) An area of 4 mm×4 mm has been exposed on a 170 µm thick glass substrate by stitching with the motorized stage. Finer features have been patterned by the piezo (oil immersion, NA = 1.4, photoresist: SU-8). (b) Both positioning stages can be addressed independently. The piezo is mounted on top of a motorized stage and swung open to reveal the interior of the "writing head" with the objective.

### Typical writing process/Computer-aided manufacturing

The choice of a substrate is the next step. To achieve highest resolution, the usual route is to employ 170 µm thick glass substrates because NA = 1.4 objectives are immersion systems and corrected to 170 µm cover slips. The glass slides and the immersion oil have a refractive index of $n = 1.518$.

The interface between the substrate and the piezo stage is a special designed substrate holder on which up to 16 glass slides (22 mm×22 mm) are reversibly fixed. The piezo system moves the substrates relative to the focus as explained earlier. In this serial process, a volume of 300 µm×300 µm×300 µm can be stitched together.[2] Fig. 4.4(a) shows a test structure which has been written in this manner. The area of 4 mm×4 mm has been structured with a grating, i.e., with parallel lines with a pitch of 10 µm from one center of the voxel to the other. The writing speed of the piezo can be 2 mm/s or even faster. However, for complex 3D structures, it is usually set to about 150 µm/s.

To extend the volume and to increase the writing speed, air objectives with NA≤1 are used. Fig. 4.4(b) reveals the interior of the "writing head" with the objective. By moving the motorized stage, we have patterned a 20 µm-pitch phase grating with 2 mm/s in an area of 1 cm×1 cm (not shown). Notably, opaque substrates (like, e.g., a silicon wafer) have to be flipped, i.e., the resist has to point to the objective.

The programming of the trajectories is usually done with *Labview* or *Matlab*. The software of the system works with the script language "GWL" (General Writing Language), in which the trajectories can intuitively been programmed in *xyz* coordinates, i.e., data sets like $(x_1,y_1,z_1),(x_2,y_2,z_2),...,(x_j,y_j,z_j)$ are delivered to the piezo stage.

[2]The maximum axial working distance of the oil objective is 160 µm.

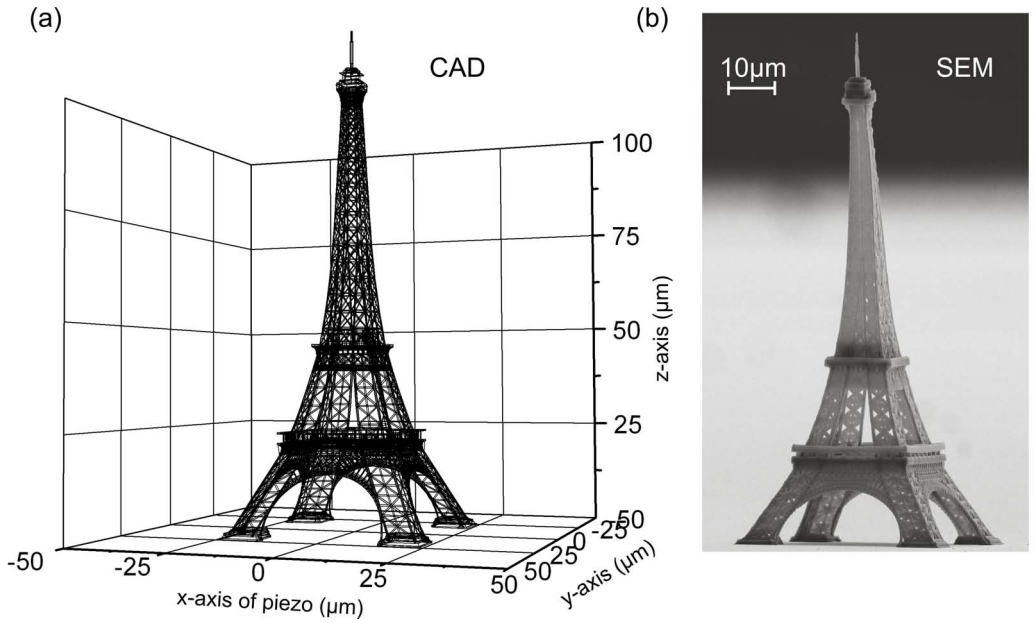


Figure 4.5: Computer-aided design (CAD) versus scanning electron micrograph (SEM) of a fabricated miniaturized Eiffel tower (scale of 1:3,400,000).

Computer-aided design (CAD) formats, like "STL" (Standard Triangulation Language) and "DXF" (Drawing Exchange Format), can also be imported directly into the software.

In Fig. 4.5, a miniaturized Eiffel tower at a scale of 1:3,400,000 is shown as example. The original CAD file has been converted from DXF to GWL and has been written without any corrections. Nearly all of the fine features of this rather complex architecture have been reproduced. The DLW photoresist IP-G has been used for this example. Details of photoresists and their applications are discussed in section 4.3.

### Limits to feature sizes

DLW offers both real 3D control in the fabrication process and sub-100 nm feature sizes right below the diffraction limit. How is it possible to achieve such a "resolution" with a DLW system?

The resolution of a conventional imaging system is defined by the diffraction limit [48]. Abbe stated that the minimum distance between two distinguishable point-spread functions is given by

$$\Delta r_{\parallel} = 0.6098 \frac{\lambda}{\mathrm{NA}} \,. \tag{4.2}$$

As a consequence, the resolution $\Delta r$ is laterally limited to 340 nm when assuming a wavelength of 780 nm and $\mathrm{NA} = 1.4$.

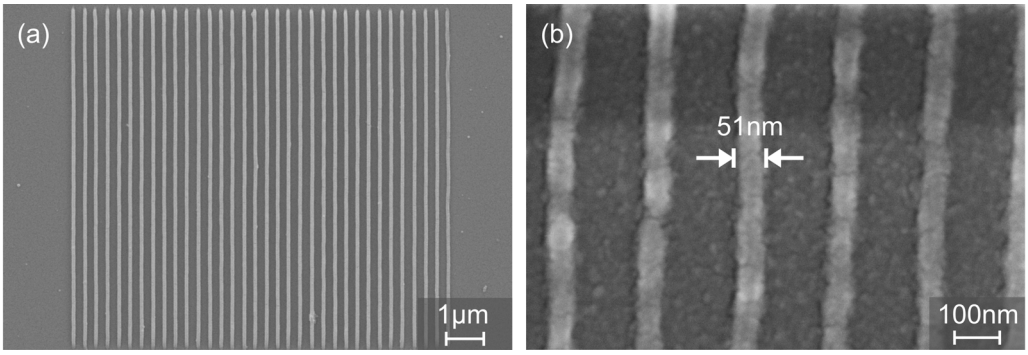


Figure 4.6: 2D resolution tests (oil immersion, NA = 1.4, photoresist: IP-G). (a) 300 nm-pitch grating with a linewidth of about 95 nm. (b) 200 nm-pitch grating with a linewidth of about 51 nm.

The axial limit can be estimated by

$$\Delta r_{\perp} = 2\frac{n\lambda}{\mathrm{NA}^2}\,, \tag{4.3}$$

to be 1208 nm (for a refractive index $n = 1.518$). These criteria serve as a rule of thumb to determine the resolution limit.[3]

For DLW, the intensity distribution obviously plays a crucial role and high-NA objectives are employed to achieve highest resolution. However, the "resolution" of the system is determined by the fabricated structures, i.e., the photoresist itself is of vivid importance. The material is exposed when the polymerization threshold is exceeded. To find the smallest features possible, the laser power has to be reduced to the point where it exceeds the exposure threshold only slightly. The sensitivity of the developer might also play a role. Moreover, DLW is a serial process and the question arises if the resist "stores" the dose when two voxels are exposed side by side but with a time delay. Therefore, besides the diffraction limit, there are also other factors determining the "resolution" of our DLW system:

- The laser stability at the edge of the exposure threshold might lead to inhomogeneities. The use of fiber laser technology is a step towards better stability of the light source.
- The proximity effect can play a crucial role at crossing points and depends on the "memory" of the photoresist in our serial process.
- Photoresists usually undergo stress and shrinkage during writing and/or development. Therefore, mechanical stability of ultra-fine features is necessary in complex 3D nanostructures.

[3] The focal intensity distribution for very similar parameters has been calculated with vector diffraction theory in reference [61]. The lateral and axial minimum of this distribution is comparable to $\Delta r_{\parallel}$ and $\Delta r_{\perp}$, respectively.

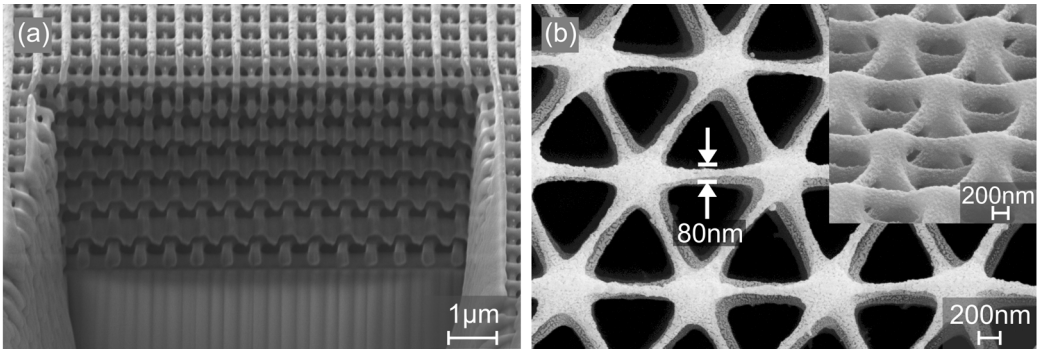


Figure 4.7: 3D resolution tests. (a) Woodpile structure with lateral lattice constant of $a = 600\,\text{nm}$. For each 200 nm rod, three trajectories have been written with 65 nm distance (oil immersion, NA = 1.4, photoresist: IP-L). (b) 80 nm rod in a 3D chiral photonic crystal (oil immersion, NA = 1.4, photoresist: SU-8).

To check the resolution of the system, we investigate both 2D gratings and 3D woodpiles. Results are shown in Figs. 4.6 and 4.7, respectively.[4] In any case, we have to connect the structure to the glass surface. For a 2D grating, the focus has to be close to the interface of glass and resist. The exposed volume and, hence, the actual linewidth clearly depends on how much of the focus intensity is lost in the non-exposable glass substrate. The autofocus system of our DLW setup provides the accuracy ($\pm\,40\,\text{nm}$) for reproducible 2D patterning near the glass interface. A special designed photoresist IP-G is employed to write a 300 nm-pitch grating with lines of around 95 nm width (compare Fig. 4.6(a)). IP-G has been developed as side project of this thesis (see also section 4.3). So far, the smallest 2D features in IP-G are found to be 51 nm in a 200 nm-pitch grating. We note that most of the intensity was focused into the glass in this second 2D example. The lines of the 200 nm grating are also pretty wavy after development.

To determine the 3D resolution, we consult the woodpile structure [55, 114]. The lateral lattice constant is set to $a = 600\,\text{nm}$. One axial lattice constant consists of 4 layers: The second layer is perpendicular to the first layer, the third is parallel to the first layer but laterally shifted by $a/2$, and the forth layer is again perpendicular to the first layer but laterally shifted by $a/2$ compared to second layer.

These four layers are stacked with a layer distance of only 212 nm resulting in an axial period $c = \sqrt{2}a$ for a face-centered-cubic (fcc) woodpile. To achieve roundish rods, three trajectories (with a distance of 65 nm) have been written for each 200 nm rod. The resulting structure is cut with a focused ion beam (FIB) (shown in Fig. 4.6(a)). The FIB cut reveals all 24 layers and good overall homogeneity. Photoresist shrinkage is dominantly axial and measured to be 12.5%. The structure also showed optical spectra which agreed well with the expectations (compare appendix D).

[4] Results of other groups can be found in recent reviews [98, 99].

The smallest features in a 3D geometry have been found in a chiral woodpile (the design is discussed in chapter 6). Here, the used photoresist is SU-8 and rods with features on the order of 80 nm have been exposed. We note that this structure was not optically characterized because we have designed its optical properties assuming a larger filling fraction. It is also doubtful if one could simply scale down the lattice constants to achieve a proper filling fraction with 80 nm lines because the proximity effect for very small lattice constants is rather large in SU-8.

In summary, the resolution of DLW is dependent on several factors and can only be determined by characterization of the resulting structures. To date, for 2D structures, we consider 90 nm lines with 300 nm spacing as a convincing result. In 3D, the story is even more complicated because very small features do not necessarily mean that we can build a structure with very small spacings. In our tests, 600 nm woodpiles have been fabricated in good quality by building up each 200 nm rod with 3 closely spaced rods. The right choice of the photoresist is necessary for best results. Therefore, photoresists and their possible application are presented next.

## 4.3. Photoresists and applications

The freedom of flexible structuring in all three dimensions on a sub-micrometer scale is valuable for a variety of research fields:

- In photonics, periodic nanostructures like photonic crystals and metamaterials mold and control the flow of light. For photonic crystals, the importance of the third dimension was clear from the beginning [11, 12]. The fabricated polymeric photonic crystals often serve as template for infiltration processes with high-index materials [62]. The younger field of metamaterials has just started to explore the new possibilities of 3D architectures. For metallic metamaterials, the 3D templates have to be metalized [40, 107]. Other applications in optics and photonics are, e.g., distributed feedback lasers, photonic ring resonators, optical interconnects, diffractive optics, or mask manufacturing.
- In life sciences, cell studies have long been restricted to 2D templates. Two-photon absorption allows for fabricating extra-cellular matrices for stem-cell differentiation or cell-growth studies [115]. Moreover, examination of the Gecko or Lotus effect need the ability to structure the third dimension.
- Microfluidic devices control confined fluids on sub-millimeter scale and enable flow control (pumps and valves) or sensors. Recently, lab-on-a-chip devices for microfluidics received considerable interest integrating several functions on a chip of some square centimeters. DLW can provide patterning of the gratings for distributed feedback lasers [116] or a tailored 3D environment with sub-micron resolution for functional devices on commercial glass chips.

Table 4.1.: Important parameters of commercially available resists have been evaluated. "Resolution" denotes the lateral linewidth we found to be necessary that fabricated structure and 3D-CAD match. Nevertheless, this linewidth only holds approximately for arbitrary 2D/3D architectures as discussed in subsection 4.2.

| Resist | Type | Tone | "Resolution" | Typical thickness | Remark |
|---|---|---|---|---|---|
| SU-8 | Cationic | Neg | 150 nm | 5-100 µm | Allrounder |
| IP | Radical | Neg | 120 nm | drop cast | Low proximity |
| $As_2S_3$ | VAP | Neg | 200 nm | 10 µm | High $n = 2.45$ |
| Ormocere | Radical | Neg | 250 nm | drop cast | Biocompatible |
| AZ 5214E | Cationic | Neg | 300 nm | 1 µm | 2D resist |
| AZ MiR 701 | DNQ | Pos | 300 nm | 1 µm | 2D resist |
| AZ 9260 | DNQ | Pos | 350 nm | 10 µm | Galvanization |

Having a certain application in mind, the right choice of the photoresist is of vital importance. Basic properties like, e.g., thermal and chemical resistance, etch rates, mechanical stability, and, importantly, optical transparency must be taken into account. For chiral photonic crystals, the demands on resolution are intense. Therefore, we have tested several commercial and self-made photoresists during this thesis to reduce feature sizes while maintaining structural quality. In the case of metallic metamaterials, we have fabricated polymeric templates for metalization with advanced deposition techniques [40, 107]. Results from these metalized templates are discussed in the theses of my colleagues.

Here, we present an overview of some of the tested photopolymers and of the photosensitive semiconductor $As_2S_3$ (compare tabular 4.1 and Fig. 4.8).[5] The basic idea is to change the resist locally in a way that a developer solves the exposed material at a very different rate compared to unexposed material. Clearly, two types of resist are possible: Negative-tone resists having a smaller development rate for exposed material, and positive-tone resists having a higher development rate for exposed material.

### Basic mechanisms of polymerization

Even though we have tested numerous resists, there are only three underlying exposure mechanisms.[6] The negative-tone photopolymers are based on chain-growth polymerization (radical or cationic), the negative-tone chalcogenide glass $As_2S_3$ undergoes a photo-induced bond rearrangement [117, 118], and the positive-tone resists

[5] All processing steps can be found in the corresponding data sheets of the distributors.
[6] Notably, other groups have used different resists and/or different photoinitiators [98, 99].

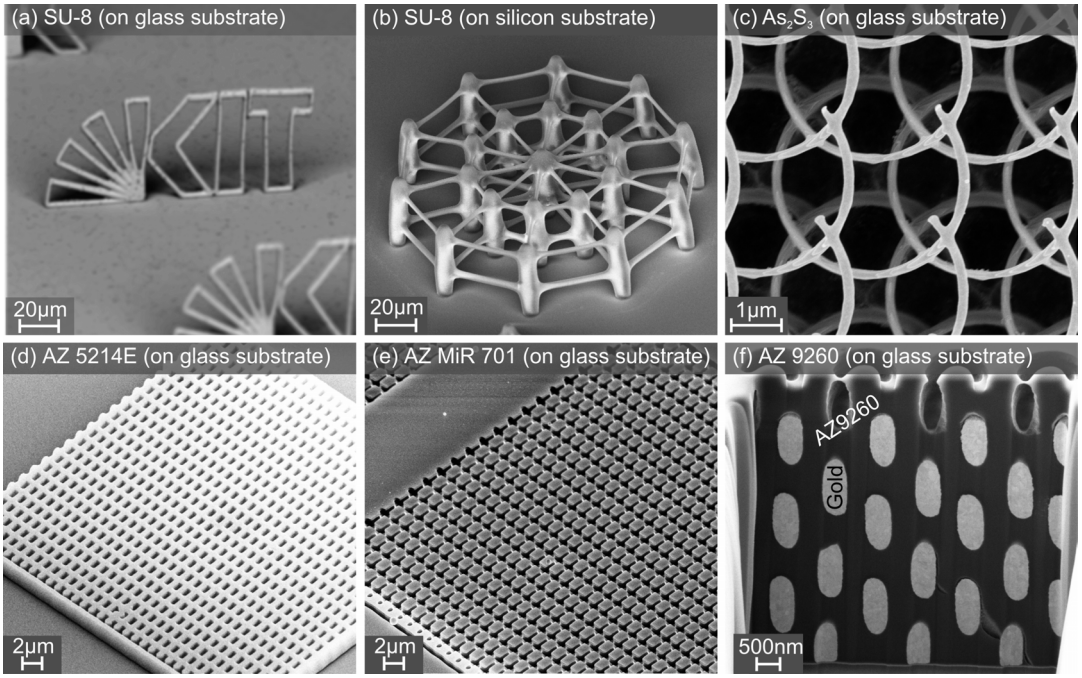


Figure 4.8: Gallery of electron micrographs of some of the tested photoresists (negative- and positive-tone). Part (f) is reproduced with kind permission of J. K. Gansel.

work with diazonaphthoquinone-(DNQ-)sulfonate inhibitors [40]. We want to give a small description for each of these mechanisms:

- Chain-growth polymerization is the exposure mechanism of the majority of DLW resists. Breaking of internal bonds (such as rings) in unsaturated monomers leads to a chain reaction and subsequent cross-linking of the final polymer. The chain initiation is the first step, followed by the chain propagation and termination. This reaction can be started by either radical or cationic photoinitiators (PI), which are excited by the nonlinear two-photon-absorption process. For *radical* polymerization, the excitation leads to radicals beginning the chain-reaction by breaking the bonds of the monomer. The process is terminated when the radicals react with themselves to a single molecule. Oxygen can also quench the polymerization process. An alternative mechanism to radical polymerization is *cationic* polymerization. Upon excitation, a cationic PI generates a strong acid. This photoacid breaks the bonds of the monomers and leads to a catalytic chain reaction. To accelerate the slow chain propagation, baking of the cationic resists is common. Cationic PIs are often used for polymerizing of epoxides and vinyl ethers. The unpolymerized parts are dissolved by developers, e.g., isopropanol.
- Photo-induced bond rearrangement in chalcogenide glass $As_2S_3$ is explained by valence-alteration pair (VAP) theory [118]. Two-photon absorption leads to the generation of a localized exciton. Coupling effects of the exciton and the lattice

phonons allow for a meta-stable charged defect called VAP. Rearrangement of the bonds between the atoms during the exciton lifetime leads to the insolubility of exposed $As_2S_3$ in a selective wet etch [105].

- The tested positive resists are based on DNQ-sulfonate inhibitors solved in a resin matrix (Novolak). DNQ lowers the solubility of the unexposed resist by one or two orders of magnitude compared to the pure resin. Upon exposure, a carboxylic acid is generated converting exposed regions into products soluble in aqueous alkaline. Since Novolak is also soluble, a positive-tone resist results.

It is in fact not surprising that so many resists can be employed for DLW because the exposure lines of standard UV-lithography resists are around the half of our laser wavelength (e.g, "i-line" (365 nm) or "g-line" (436 nm)). In the next years, more reports on DLW resists with superior resolution can surely be expected.

#### Considerations concerning the fabrication of chiral photonic crystals

Producing a twist on nanoscale requires ultra-high structuring precision for all spatial coordinates while structural footprints must be large enough for optical transmittance spectroscopy. To date, these requirements still represent enormous challenges for nanotechnology. Helical pitches of 1.3 µm and below must be achieved to tune the chiral resonances in the technological interesting region of about 1.55 µm. Fortunately, we meet these challenges with DLW as flexible method concerning the fabrication of chiral photonic crystals.

In order to achieve the necessary precision and rapid production speed, the system with immersion oil objective and 170 µm glass substrates has been chosen for the experiments. Next, the cationic negative-tone resist SU-8 is spun onto a glass slide reaching a thickness of about 100 µm. This photoresist has been found to be a right choice[7] because of good resolution (lateral: 150 nm, axial: 400 nm) and high transparency from the visible to the near-infrared spectral range. Furthermore, a great advantage of SU-8 is the low change of the refractive index upon exposure, i.e., the perturbation of the laser focus at crossing points is very small (important for the results in chapter 7). The refractive index of the polymer is nearly index-matched to the glass slide ($n_{SU8} = 1.57$, $n_{Glass} = 1.518$). The photonic crystals are programmed to have typical footprints of about 60 µm×60 µm. In energy series, the deposited energy and the position on the substrate is changed automatically by using the AOM and the motorized stage, respectively.

In summary, the degree of automatization and the good resolution of the photoresist allows for reproducible rapid prototyping of chiral photonic crystals. The next logical step is the optical characterization of the fabricated crystals explained in the next chapter.

[7] The IP-series showed superior resolution due to a small proximity effect. So far, we have not written chiral crystals into IP resist but smaller features shall be possible in the future.

# 5. Optical characterization and numerical calculations

In the last chapter, DLW has been rendered as an ideal fabrication method for chiral nanostructures. Electron micrographs have confirmed this statement. Furthermore, focused-ion-beam cutting has given information about the interior of the 3D samples. Nevertheless, as this thesis deals with *photonic* crystals, the characterization is only complete with the evaluation of their optical properties.

In the first section of this chapter, we therefore present two setups for linear-optical transmittance spectroscopy to further investigate the quality and functionality of the fabricated structures. Analyzing the chiral-optical properties demands the control of the impinging polarized light. Hence, both setups are modified to be ready for broadband polarization-resolved spectroscopy. Moreover, the comparison of measured optical transmittance spectra and calculated data of ideal photonic crystals is valuable. We have chosen the well-established scattering-matrix approach as computational method for the theoretical characterization and design of the crystals. Principles of the scattering matrix are explained in section 5.2.

## 5.1. Polarization-resolved spectroscopy tools

The optical characterization tools have to meet several requirements. First of all, our photonic crystals have typical footprints of 60 µm×60 µm demanding for appropriate imaging optics in the setups. Secondly, the detectors of the setups need to be sensitive to near- and/or mid-infrared radiation because the fabricated chiral photonic crystals have lattice constants between 1 µm and 4 µm (see chapters 6 and 7). Last, we want to probe the fabricated crystals with circular polarization, i.e., super-achromatic polarizing optics are necessary in order to record the entire frequency region of interest at once.

In the following two sections, we explain spectroscopy tools which meet these requirements. The first is a home-built setup for the near-infrared spectral range and the second a commercial Fourier-transform (FT) microscope-spectrometer for the mid-infrared spectral range.

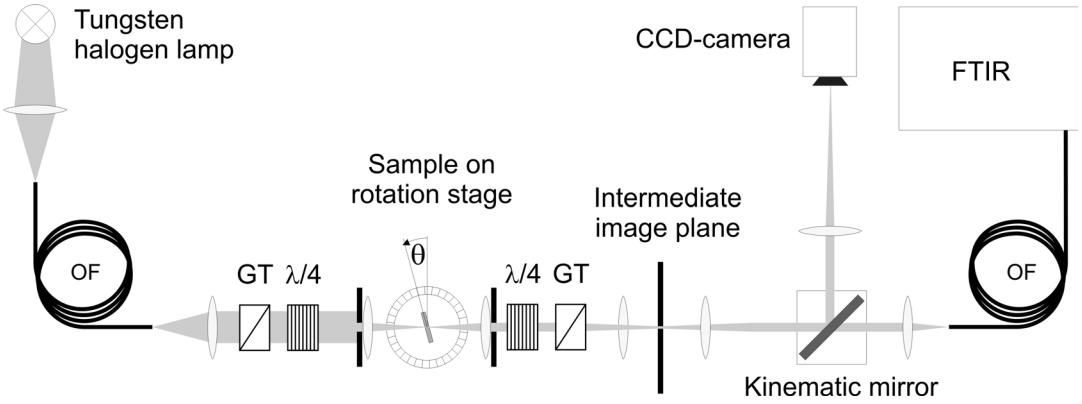


Figure 5.1: Scheme of the home-built setup for linear-optical transmittance measurements. The heart of this setup is a pair of super-achromatic quarter-wave plates, which convert linear to circular polarization (and vice versa) enabling broadband polarization-resolved spectroscopy of 3D chiral photonic crystals. Adapted from [61].

### 5.1.1. Setup for measurements in the near-infrared spectral range

For measurements in the near infrared, we used a home-built white-light setup in combination with a home-built Michelson interferometer sketched in Fig. 5.1. The setup allows for calibrated transmittance spectroscopy on small-area samples in a spectral range from 500 to 2200 nm.

The white-light source is a standard 100 W halogen lamp, which is coupled into an optical multi-mode fiber (OF, 200 µm core diameter). The output is collimated and sent through a Glan-Thompson (GT) polarizer. To control the polarization state of the incident light completely, we introduce a super-achromatic quarter-wave plate ($\lambda/4$, Bernhard Halle Nachfolger GmbH) which converts linear polarization to circular polarization in a spectral range from 600 to 2700 nm. This retarder consists of three pairs of quartz and $MgF_2$ plates cemented to each other and has a calculated path difference of $\lambda/4 \pm 0.25\%$. The orientation of the optical axis only changes by $\pm 0.1°$ in the entire working range. The polarized light is imaged onto the sample and an aperture ensures an estimated effective half-opening angle of 5°. The sample is mounted on goniometers being themselves mounted on a rotation stage for angle-resolved measurements. The transmitted light is collected, filtered in the intermediate image plane, and a kinematic mirror reflects the light onto a CCD camera in order to select the correct cut-out of the structure. Afterwards, the mirror is taken out and light is imaged onto a second multi-mode OF connected to a home-built FT spectrometer. The nitrogen-cooled InSb detector is sensitive in the spectral range of 600–2200 nm. Alternatively, the fiber can be connected to a commercial optical spectrum analyzer (Ando AQ-6315B) reducing the range of the setup to 500–1750 nm wavelength.

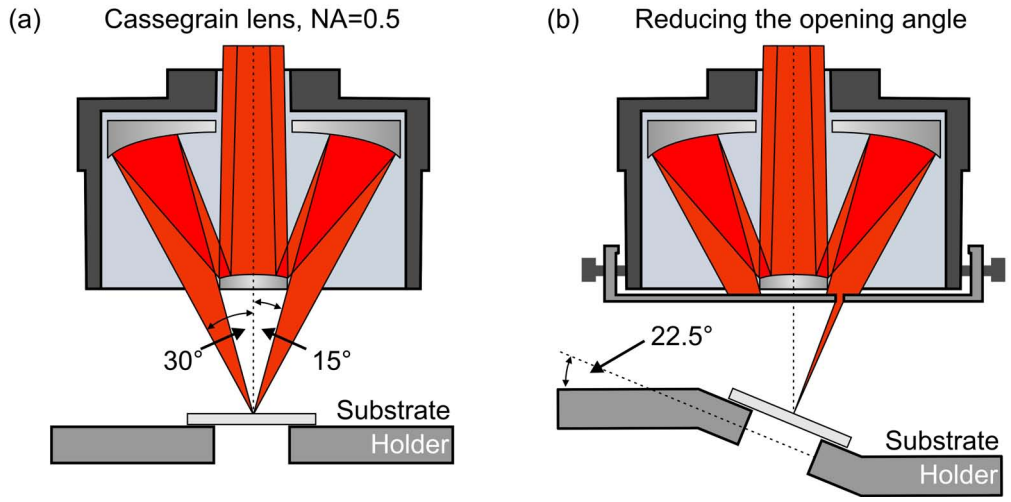


Figure 5.2: (a) Scheme of the Cassegrain lens, which allows for mid-infrared spectroscopy but conceptionally demands oblique incidence of light. (b) Nominally normal incidence with a full-opening angle of about 5° can be achieved by using a pinhole and a special substrate holder.

An additional pair of super-achromatic quarter-wave plate and polarizer may serve as analyzing optics to determine the polarization state of the transmitted light. Normalization of all spectra was carried out with respect to the transmittance of the bare glass substrate. This setup was used for the linear-optical measurements in chapters 6.1, 6.2, and 6.3.

### 5.1.2. Setup for measurements in the mid-infrared spectral range

The second setup for linear-optical spectroscopy in the mid-infrared spectral range is a commercial FT microscope-spectrometer (Bruker Tensor 27 with Hyperion 1000 microscope). The nitrogen-cooled Mercury-cadmium-telluride (MCT) detector is sensitive in a range of 1–12.8 µm. The imaging optics of the microscope provide enough signal to measure footprints on the order of 10 µm over this rather huge spectral bandwidth. However, the used Cassegrain objectives (NA = 0.5, 36x) come with a major drawback: A cone of light with an opening angle between 15°–30° is focused onto the sample (compare Fig. 5.2 where a slice through the cone is shown). To overcome this drawback, we modified the reflective Cassegrain optics by introducing a diaphragm (diameter of 1.5 mm) to reduce the full-opening angle of the incident light. By tilting the sample by 22.5°, the opening angle was reduced to about 5° with nominal normal incidence (shown in Fig. 5.2(b)). The reduced signal is still strong enough for fast and reliable measurements.

Importantly, we custom modified this commercial instrument by constructing polarization optics that could be inserted and that allow broadband transmittance spec-

troscopy to be carried out with incident circular polarization of light. The heart of this add-on is a high-extinction wire-grid polarizer (Bruker) and a super-achromatic quarter-wave plate consisting of 7 single $MgF_2$ plates (cement-free custom optic from Bernhard Halle Nachfolger GmbH) granting the broadband retardation of $\lambda/4 \pm 14\%$ in the spectral regime of 2.5–7.0 µm wavelength (orientation of the optical axis $\pm 6°$). Normalization of all spectra was again carried out with respect to the transmittance of the bare glass substrate. This setup was used for the linear-optical measurements in chapters 6.4 and 7.

## 5.2. Numerical methods

Polarization-resolved spectroscopy allows for the experimental characterization of chiral photonic crystals in the visible to near-infrared spectral region (600–2200 nm) and mid-infrared spectral region (2700–7000 nm). To further investigate the optical properties and to rule out experimental artifacts, one performs numerical calculations.

A typical question in the context of photonic crystals is whether the structure has a complete photonic bandgap. To answer this question, we usually employ the MIT Photonic-Bands (MPB) package [57] already explained in section 2.3.1. When it comes to a transmittance experiment with finite photonic crystals, interfaces are always present. Interfaces give rise to refraction, diffraction, and to surface waves. The symmetry of the Bloch modes determines if a wave can couple into the crystal or not. Therefore, calculating the band structure alone is not sufficient for the comparison with experiments, and we have to find another method.

In this thesis, the well-established scattering-matrix approach has been used, capable of calculating transmittance spectra of finite-size structures and allowing for direct comparison with measured spectra [119, 120]. Moreover, the method has been employed to design new photonic-crystal architectures. This theoretical tool is the last piece for a complete characterization of our chiral nanostructures. Basic principles of the scattering-matrix approach are discussed next (for a more comprehensive introduction of this approach and of our program code,[1] we refer the reader to references [119, 120] and [61], respectively).

### 5.2.1. Scattering-matrix approach

By using this numerical simulation software, we can calculate the transmittance and reflectance spectra of finite-size photonic-crystal structures taking into account the angle of incidence and the polarization state of light.

Let us first discuss the typical experimental situation (shown in Figs. 5.2 and 5.3): The photonic-crystal structure is written on a glass substrate, has a finite number of

[1] The program code was originally implemented in *Matlab* by Dr. Stefan Linden.

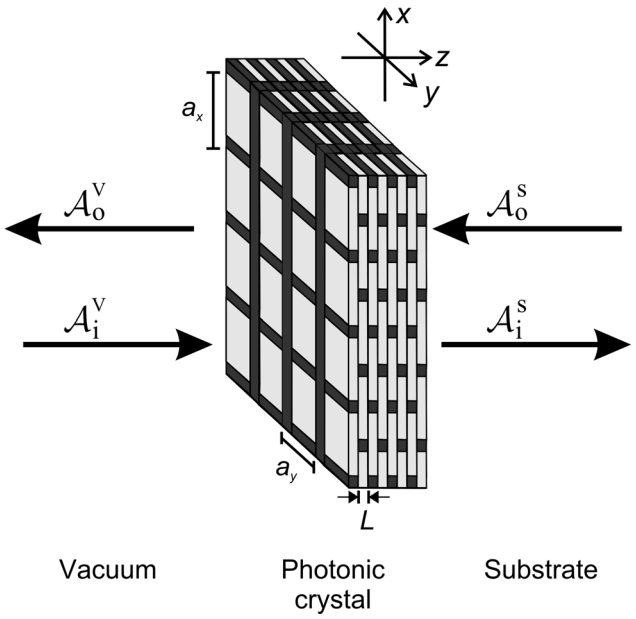


Figure 5.3: Scheme of a typical experimental configuration which is simulated by the scattering-matrix approach. A light wave impinges on the periodic crystal from the left (vacuum-)side leading to a transmitted and reflected wave. The wave $\mathcal{A}_o^S$ which hits the crystal from the substrate-side is set to zero (corresponding to the experiment).

axial and lateral periods, and is mounted on the rotation stage of the experimental setup. The electromagnetic light wave with frequency $\omega$ and amplitude $\mathcal{A}_i^V$ impinges on the interface between vacuum half-space (refractive index $n_V$) and photonic-crystal structure. Then, we define the reflected wave amplitude $\mathcal{A}_o^V$, the transmitted wave amplitude $\mathcal{A}_i^S$ propagating into the substrate half-space (refractive index $n_S$), and the wave amplitude impinging on the photonic crystal from the substrate half-space $\mathcal{A}_o^S$ (usually equals zero in our experiments). Such a configuration of a periodic optical system is usually written mathematically using a matrix formalism. For example, the waves of vacuum and substrate half-space can be connected with the well-known transfer-matrix formalism [121]:

$$\begin{pmatrix} \mathcal{A}_i^S \\ \mathcal{A}_o^S \end{pmatrix} = \hat{\mathbb{T}}_{V,S} \begin{pmatrix} \mathcal{A}_i^V \\ \mathcal{A}_o^V \end{pmatrix} = \begin{pmatrix} \mathcal{T}_{11} & \mathcal{T}_{12} \\ \mathcal{T}_{21} & \mathcal{T}_{22} \end{pmatrix} \begin{pmatrix} \mathcal{A}_i^V \\ \mathcal{A}_o^V \end{pmatrix} . \tag{5.1}$$

To reduce the complexity of the problem, we decompose the photonic crystal into layers, which are periodic in $xy$-direction and homogeneous in $z$-direction (shown in Fig. 5.3). Effectively, we can now solve the lateral problem (2D eigenmodes) and the resulting fields can be coupled with the fields of the next cell in $z$-direction via a interlayer matrix $\hat{\mathbb{T}}_{Z_n,Z_{n-1}}$. Multiplication of all matrices of the optical system leads to the transfer matrix $\hat{\mathbb{T}}_{V,S}$ with the matrix elements $\mathcal{T}_{ij}$. Indeed, the reflected and

transmitted fields of the finite photonic crystal can be calculated according to equation (5.1).

However, Ko *et al.* showed that the transfer-matrix formalism is unstable in their simulations of resonant tunneling in semiconductor multilayer heterostructures [122]. The reason for the instabilities is the existence of evanescent waves occurring at the interface between two semiconductor materials. Since the $\hat{\mathbb{T}}$-matrix deals with exponentially decaying and growing waves, numerical instabilities are inescapable at first sight. Nevertheless, Ko *et al.* found a solution to the problem by introducing the scattering-matrix approach leading to converging results [122]. In the publications of Whittaker [119] and Tikhodeev [120] this approach has been applied to simulate finite periodic structures for photonics.[2]

The scattering-matrix formalism (5.2) resembles the transfer matrix (5.1) with an important difference: While the $\hat{\mathbb{T}}$-matrix connects the amplitudes of the substrate and the amplitudes of vacuum, the $\hat{\mathbb{S}}$-matrix connects the waves, which are incident (on the photonic crystal) and the outgoing waves:

$$\begin{pmatrix} \mathcal{A}_{\mathrm{i}}^{\mathrm{S}} \\ \mathcal{A}_{\mathrm{o}}^{\mathrm{V}} \end{pmatrix} = \hat{\mathbb{S}}_{\mathrm{V,S}} \begin{pmatrix} \mathcal{A}_{\mathrm{i}}^{\mathrm{V}} \\ \mathcal{A}_{\mathrm{o}}^{\mathrm{S}} \end{pmatrix} = \begin{pmatrix} \mathrm{S}_{11} & \mathrm{S}_{12} \\ \mathrm{S}_{21} & \mathrm{S}_{22} \end{pmatrix} \begin{pmatrix} \mathcal{A}_{\mathrm{i}}^{\mathrm{V}} \\ \mathcal{A}_{\mathrm{o}}^{\mathrm{S}} \end{pmatrix} . \tag{5.2}$$

Similar to the transfer matrix (mind the change of indices), we deal with layers which are periodic in $xy$-direction and homogeneous in $z$-direction (as shown in Fig. 5.3). Before actual calculating the scattering matrix, we first employ transfer matrices again. The transfer matrix within the continuous $n$th of $N$ cells is denoted as $\hat{\mathbb{T}}_{\mathrm{Z}_n}$. Adjacent layers are coupled via an interlayer transfer matrix denoted as $\hat{\mathbb{T}}_{\mathrm{Z}_n,\mathrm{Z}_{n-1}}$. The last missing transfer matrices are the ones which couple the substrate to the $N$th layer, $\hat{\mathbb{T}}_{\mathrm{S},N}$, and the first layer to the vacuum half-space ,$\hat{\mathbb{T}}_{1,\mathrm{V}}$, respectively. Consequently, the complete transfer matrix $\hat{\mathbb{T}}_{\mathrm{V,S}}$ reads

$$\hat{\mathbb{T}}_{\mathrm{V,S}} = \hat{\mathbb{T}}_{\mathrm{S},N} \hat{\mathbb{T}}_{\mathrm{Z}_N} \hat{\mathbb{T}}_{\mathrm{Z}_N,\mathrm{Z}_{N-1}} ... \hat{\mathbb{T}}_{\mathrm{Z}_1} \hat{\mathbb{T}}_{1,\mathrm{V}} . \tag{5.3}$$

The scattering matrix for $M$ layers $\hat{\mathbb{S}}_M$ can be calculated with the scattering matrix for $M$-1 layers and one *inverse* transfer matrix for the missing layer. Since an inverse transfer matrix does not lead to numerical problems, we have found a stable possibility to iterate the scattering matrix $\hat{\mathbb{S}}_M$ beginning with the initial condition, that is, $\hat{\mathbb{S}}_{\mathrm{V,V}} = \hat{\mathbb{I}}$. The scattering matrix finally reads

$$\hat{\mathbb{S}}_M = \begin{pmatrix} \mathcal{D}\mathcal{S}_{11} & \mathcal{D}\mathcal{B} \\ \mathcal{S}_{2\,1} + \mathcal{S}_{22}\mathcal{T}_{21}\mathcal{D}\mathcal{S}_{11} & \mathcal{S}_{22}\mathcal{T}_{22} + \mathcal{S}_{22}\mathcal{T}_{21}\mathcal{D}\mathcal{B} \end{pmatrix} , \tag{5.4}$$

where $\mathcal{B} = \mathcal{S}_{12}\mathcal{T}_{22} - \mathcal{T}_{12}$, $\mathcal{D} = (\mathcal{T}_{11} - \mathcal{S}_{12}\mathcal{T}_{21})^{-1}$, and $\mathcal{S}_{ij}$ and $\mathcal{T}_{ij}$ are the matrix elements of $\hat{\mathbb{S}}_{M-1}$ and $\hat{\mathbb{T}}$, respectively.

[2] Our program code is based on these publications. Notably, other theory groups have also published on the scattering-matrix approach, e.g. [123].

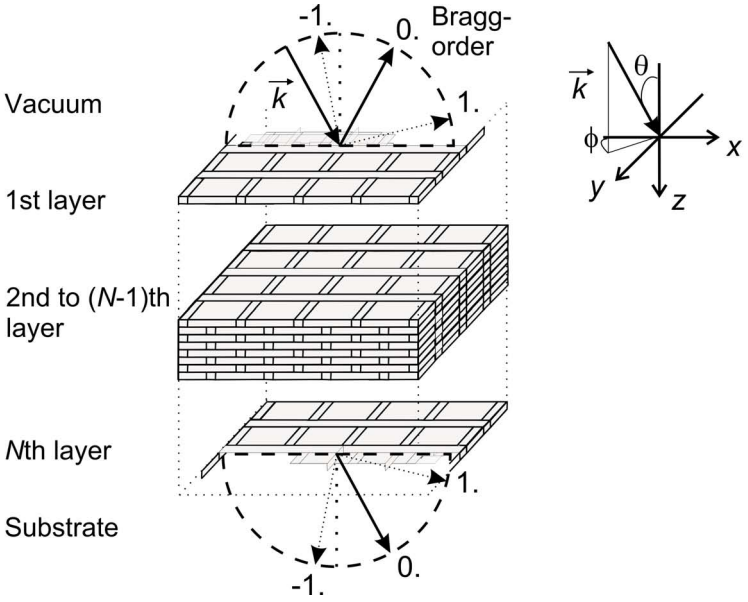


Figure 5.4: Decomposition of the photonic crystal in $xy$-periodic layers. Bragg orders of the transmitted and reflected waves are observed (only the first orders are shown here).

The discussion of all necessary equations [61, 119, 120] is beyond the scope of this chapter, however, we want to discuss the influences of the periodicity of the photonic crystals. From Fig. 5.4, one can easily imagine the periodic surface to be a highly diffractive interface and one observes different Bragg orders.[3] As a consequence, the electromagnetic field can be expressed as superposition of partial waves with wave vectors parallel to the surface, $\vec{k}_{\parallel,m}$, and wave vectors perpendicular to the surface, $q_{z,m}$. An integer number of reciprocal lattice vectors can always be added to the parallel wave vector $\vec{k}_{\parallel,m}$ leading to equation (5.5):

$$\vec{k}_{\parallel,m} = \vec{k}_{\parallel,0} + \vec{G}\,, \tag{5.5}$$

where $\vec{G} = 2\pi\,(m_x/a_x, m_y/a_y)$ is the reciprocal lattice vector depending on $m_i \in \mathbb{Z}$. The absolute value of the $z$-component of $\vec{k}$ (perpendicular to the surface) can be expressed as

$$q_{z,m} = \pm\sqrt{\left(\frac{w}{c}\right)^2 - (\vec{k}_{\parallel,0} + \vec{G})^2}\,. \tag{5.6}$$

These solutions are the wave vectors for the $m$th Bragg order. In Fig. 5.4, we show the transmitted and reflected waves of the first Bragg orders as illustration. Real solutions for $q_{z,m}$ are propagating waves, imaginary solutions are evanescent waves. Latter solutions are hard to handle because they lead to growing fields in the numerics and, hence, are the reason for using the scattering-matrix approach. Notably, we cannot account for an infinite number of reciprocal lattice vectors due to limited computer

[3] Please compare the theoretical description of photonic crystals given in section 2.3.1.

resources. Therefore, a cut-off for the maximal Bragg order $g_{\max}$ is defined. Hence, the numerics only deal with a total number of $N_g = (2g_{\max} + 1)^2$ reciprocal lattice vectors.

The implementation of the matrices in equation (5.4) allows for the calculation of the complex fields via (5.2). In particular, we are interested in the transmittance and reflectance spectra of our photonic crystals which can be expressed by the $z$-component of the Poynting vector $S_z$ (for the (0,0) Bragg order, i.e., $\vec{G} = 0$):

$$R = \frac{-S_z^{\mathrm{ref}}}{S_z^{\mathrm{in}}} = \frac{\mathrm{Re}\left\{\tilde{E}^{\mathrm{o}}_{y,0,\mathrm{V}} H^{\mathrm{o}}_{x,0,\mathrm{V}} - \tilde{E}^{\mathrm{o}}_{x,0,\mathrm{V}} H^{\mathrm{o}}_{y,0,\mathrm{V}}\right\}}{\mathrm{Re}\left\{\tilde{E}^{\mathrm{i}}_{x,0,\mathrm{V}} H^{\mathrm{i}}_{y,0,\mathrm{V}} - \tilde{E}^{\mathrm{i}}_{y,0,\mathrm{V}} H^{\mathrm{i}}_{x,0,\mathrm{V}}\right\}}, \tag{5.7}$$

$$T = \frac{S_z^{\mathrm{trans}}}{S_z^{\mathrm{in}}} = \frac{\mathrm{Re}\left\{\tilde{E}^{\mathrm{i}}_{x,0,S} H^{\mathrm{i}}_{y,0,S} - \tilde{E}^{\mathrm{i}}_{y,0,S} H^{\mathrm{i}}_{x,0,S}\right\}}{\mathrm{Re}\left\{\tilde{E}^{\mathrm{i}}_{x,0,\mathrm{V}} H^{\mathrm{i}}_{y,0,\mathrm{V}} - \tilde{E}^{\mathrm{i}}_{y,0,\mathrm{V}} H^{\mathrm{i}}_{x,0,\mathrm{V}}\right\}}. \tag{5.8}$$

A tilde indicates the complex conjugated field. The input amplitudes are often linearly polarized. While for s-polarization the electric field vector is perpendicular to the plane of incidence, the electric field vector is parallel in case of p-polarization. The corresponding equations are given by

$$\mathcal{A}_{\mathrm{i}}^{\mathrm{V,s-pol.}} = (\cos(\phi)\cos(\theta),0,\ldots,\sin(\phi)\cos(\theta),0,\ldots)^{\mathrm{T}}, \tag{5.9}$$

$$\mathcal{A}_{\mathrm{i}}^{\mathrm{V,p-pol.}} = (-\sin(\phi),0,\ldots,\cos(\phi),0,\ldots)^{\mathrm{T}}, \tag{5.10}$$

where $\phi$ corresponds to the azimuth and $\theta$ to the elevation angle.

For chiral photonic crystals, a circular expansion basis is necessary. By superimposing the linear combinations, circular polarization can easily be implemented in the program code:

$$\mathcal{A}_{\mathrm{i}}^{\mathrm{V,RCP}} = \mathcal{A}_{\mathrm{i}}^{\mathrm{V,s-pol.}} - \mathrm{i}\cdot\mathcal{A}_{\mathrm{i}}^{\mathrm{V,p-pol.}}, \tag{5.11}$$

$$\mathcal{A}_{\mathrm{i}}^{\mathrm{V,LCP}} = \mathcal{A}_{\mathrm{i}}^{\mathrm{V,s-pol.}} + \mathrm{i}\cdot\mathcal{A}_{\mathrm{i}}^{\mathrm{V,p-pol.}}. \tag{5.12}$$

The imaginary unit i is distinct from the index i of the amplitudes. There is no need for normalization at this point because these factors cancel out anyhow in equation (5.8).

Importantly, we can also analyze the phase differences between the components, i.e., the polarization state of the transmitted and reflected amplitudes. The phase difference between the $x$- and $y$-component of the electric field can be calculated via

$$\phi = \arctan\left(\frac{\mathrm{Im}(E_x)}{\mathrm{Re}(E_x)}\right) - \arctan\left(\frac{\mathrm{Im}(E_y)}{\mathrm{Re}(E_y)}\right) \tag{5.13}$$

For example, in the case of circular polarization propagating in vacuum, the initial phase difference is conserved, i.e., we calculate $\phi = 90°$ or $\phi = -90°$.

### Calculation of the field distribution

Interpretation of the interaction of light and matter highly benefits from the calculation of the field distribution. For example, the graphical presentation of the electric energy density has been of great importance to understand the underlying physics of the structures presented in chapter 6.2.

To calculate the field distribution of a finite photonic-crystal structure, we have to know the field distribution of each layer. As a result of the iterative calculation of the scattering matrix, this task is not straightforward. Fig. 5.5 illustrates this configuration:

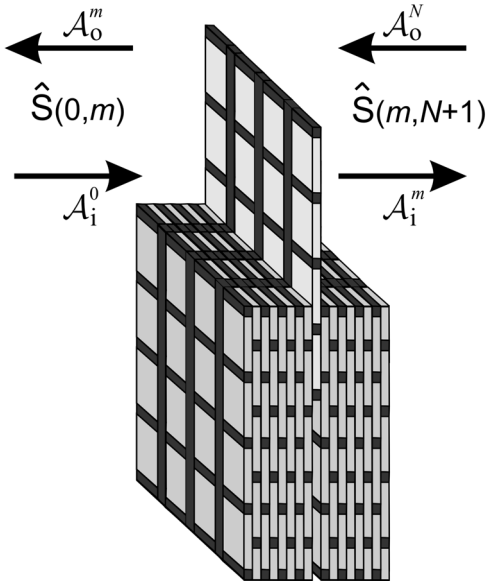


Figure 5.5: Calculation of the field distribution demands the knowledge of two scattering matrices for each layer $m$ of the photonic crystal.

Again, we decompose the crystal into $N$ layers and choose as 0th layer the vacuum half-space, layers 1 to $N$ is the crystal, and the $(N+1)$th layer corresponds to the substrate. To calculate the field of the $m$th layer, we use the matrices $\hat{\mathbb{S}}(0,m)$ and $\hat{\mathbb{S}}(m,N+1)$ that connect the amplitudes in the usual manner:

$$\begin{pmatrix} \mathcal{A}_{\mathrm{i}}^{m} \\ \mathcal{A}_{\mathrm{o}}^{0} \end{pmatrix} = \hat{\mathbb{S}}(0,m) \begin{pmatrix} \mathcal{A}_{\mathrm{i}}^{0} \\ \mathcal{A}_{\mathrm{o}}^{m} \end{pmatrix} = \begin{pmatrix} \mathrm{S}_{11} & \mathrm{S}_{12} \\ \mathrm{S}_{21} & \mathrm{S}_{22} \end{pmatrix} \begin{pmatrix} \mathcal{A}_{\mathrm{i}}^{0} \\ \mathcal{A}_{\mathrm{o}}^{m} \end{pmatrix}, \tag{5.14}$$

$$\begin{pmatrix} \mathcal{A}_{\mathrm{i}}^{(N+1)} \\ \mathcal{A}_{\mathrm{o}}^{m} \end{pmatrix} = \hat{\mathbb{S}}(m,N+1) \begin{pmatrix} \mathcal{A}_{\mathrm{i}}^{m} \\ \mathcal{A}_{\mathrm{o}}^{(N+1)} \end{pmatrix} = \begin{pmatrix} \hat{\mathrm{S}}_{11} & \hat{\mathrm{S}}_{12} \\ \hat{\mathrm{S}}_{21} & \hat{\mathrm{S}}_{22} \end{pmatrix} \begin{pmatrix} \mathcal{A}_{\mathrm{i}}^{m} \\ \mathcal{A}_{\mathrm{o}}^{(N+1)} \end{pmatrix}. \tag{5.15}$$

We solve these equations for the amplitudes $\mathcal{A}_{\mathrm{o}}^{m}$ and $\mathcal{A}_{\mathrm{i}}^{m}$ with the initial conditions, that is, $\mathcal{A}_{\mathrm{i}}^{0}$ is known and $\mathcal{A}_{\mathrm{o}}^{(N+1)} = 0$:

$$\mathcal{A}_{\mathrm{i}}^{m} = \left(1 - \mathrm{S}_{12}\hat{\mathrm{S}}_{21}\right)^{-1} \mathrm{S}_{11}\mathcal{A}_{\mathrm{i}}^{0} \tag{5.16}$$

$$\mathcal{A}_{\mathrm{o}}^{m} = \left(1 - \hat{\mathrm{S}}_{21}\mathrm{S}_{12}\right)^{-1} \hat{\mathrm{S}}_{21}\mathrm{S}_{11}\mathcal{A}_{\mathrm{i}}^{0}\,. \tag{5.17}$$

These calculations are repeated for each layer. Moreover, we also have to use the interface matrices which have already been calculated for the transmittance and reflectance spectra. Nevertheless, the calculation of two scattering matrices per layer is time-consuming. Hence, the calculations of field distributions are usually restricted to selected wavelengths.

### Achieving convergence

In the following chapters, we will always compare our experimental data with scattering-matrix simulations. All designs of chiral photonic crystals are first evaluated and optimized with numerics rather than with an experiment. Therefore, one needs to be sure that results have converged, i.e., the numerics approach a definite value.

Here, we exemplary show the convergence tests for a helical structure later discussed in chapter 6.4. The geometry is shown in Fig. 5.6(a). We choose normally incident circular polarization of light, a polymer refractive index of $n = 1.57$, and a refractive index of the semi-infinite glass substrate of $n = 1.518$. The lateral and axial discretization of each unit cell is set to $a/128 = 25.4\,\mathrm{nm}$.

Normal-incidence intensity transmittance refers to the (0,0) diffraction order. The differences of the calculated transmittance spectra with a certain Bragg order $g_i$ and the reference $g = 10$ is shown in Fig. 5.6(b) (for selected wavelengths). Obviously, these differences become smaller with higher Bragg order $g_i$ indicating converging results.

To further investigate the convergence, one wavelength is selected and the transmittance differences are plotted versus the Bragg order. The data points can be fitted by an exponential decay showing that results converge fast (Fig. 5.6(c)). When using $g = 7$ orders corresponding to $(2g + 1)^2 = 225$ reciprocal lattice vectors, the transmittance differences between $g = 7$ and $g = 8$ are within the linewidth of the curves later shown in the results chapters. For experimentalists, this is a convincing result rendering the scattering-matrix code as a robust and powerful tool to characterize low-index photonic crystals.[4]

[4] Notably, high-index materials and dispersive metal structures are known to be more complicated in numerical calculations. Nevertheless, theory groups (e.g., Prof. Busch's group in Karlsruhe) have scattering-matrix implementations with algorithms capable of handling high-index materials or even metals [123].

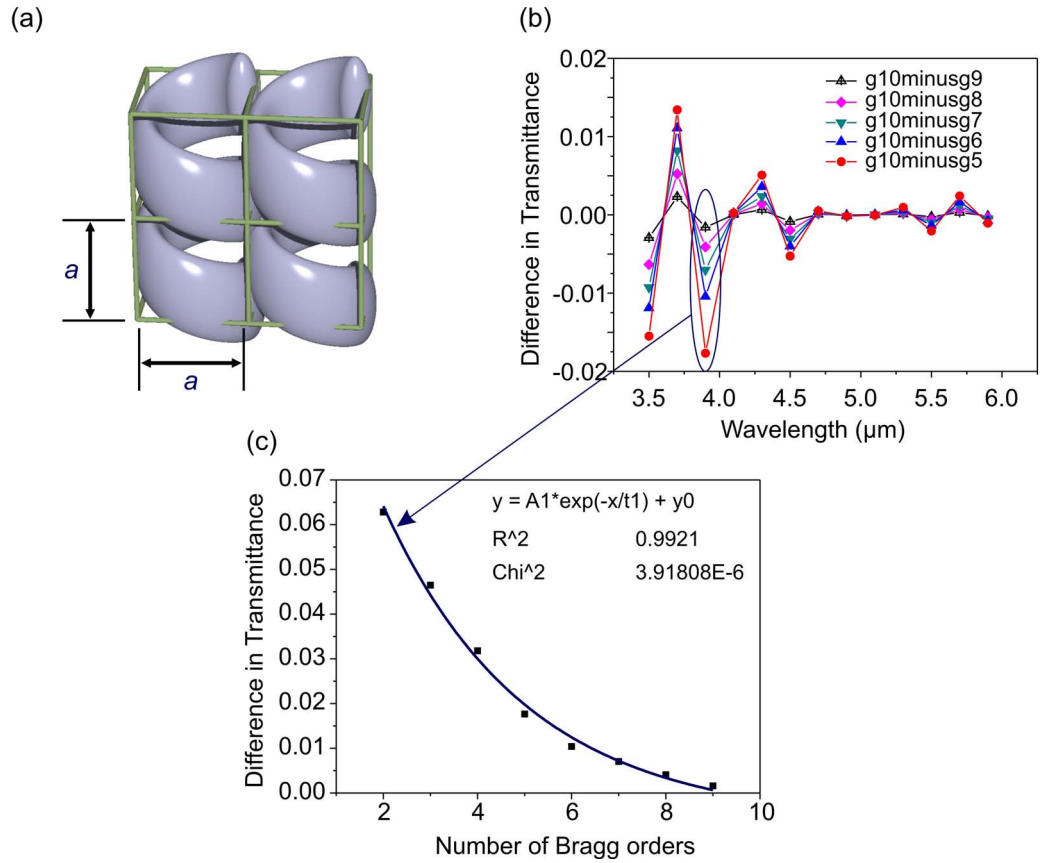


Figure 5.6: (a) The investigated structure is a uniaxial helical crystal with slightly overlapping spirals ($a = 3.25\,\mu m$). The lateral and axial discretization of each unit cell is set to $a/128 = 25.4\,nm$. (b) Calculation of normal-incidence intensity transmittance which refers to the (0,0) diffraction order. The differences of the transmittance spectra with a certain Bragg order $g_i$ and the reference $g = 10$ are plotted at selected wavelengths. (c) The differences in transmittance are plotted versus the number of Bragg orders for one selected wavelength. An exponential decay can be fitted to the data indicating converging results (fit values: A1 = 0.13664, y0 = -0.00624, and t1 = 3.01568).

## Conclusions

In summary, the scattering matrix approach is a stable and convergent numerical method for calculating optical spectra and field distributions for low-index chiral photonic structures. The easy implementation of different polymeric photonic-crystal designs allows for the characterization of their optical properties and direct comparison with the experimental results. In the following chapters, we make use of this approach for each fabricated photonic-crystal design.

# 6. Uniaxial three-dimensional chiral photonic crystals

Recently, an increasing number of researchers has designed, fabricated, and studied dielectric and metallic artificial chiral materials [14–21, 40–44]. This flourishing and dynamic field is driven by the opportunity to achieve giant chiral-optical effects by giving light yet another twist with man-made nanostructures.

The next chapters are devoted to our contributions to the emerging field of artificial chiral materials [19,20,110–112,124,125]. In the following sections, we present systematic investigations of several chiral photonic crystals, i.e, we explain the underlying physics, present a specific design, fabricate the structures by using direct laser writing (DLW), and compare experimental measurements with calculations. By giving summarizing remarks at the end of each section, we connect the related topics and explain why we decided to investigate the next particular design.

In the first sections, two basic blueprints of chiral photonic crystals with *one* helical axis are described: *Layer-by-layer* and *circular-spiral* chiral three-dimensional (3D) photonic crystals. In section 6.3, we present "thin-film" devices based on circular-spiral photonic crystals. Polarizers, "poor-man's" optical isolators, and optical diodes are proposed and explained. The last section is focused on chiral photonic superlattices, which give additional insight in the physics of the circular-spiral building block.

## 6.1. Layer-by-layer chiral photonic crystals

The first investigated chiral building block is a log pile of anisotropic layers, which are twisted along the stacking direction. Layer-by-layer approaches such as the well-known woodpile structure [55] have proven to be accessible by a large variety of different techniques (e.g., see [61]). In our experiments on *chiral* log piles, we obtain very strong circular dichroism from so-called polarization stop bands. Moreover, telecommunication wavelengths are easily accessible with the layer-by-layer approach using DLW as fabrication method. We start by presenting a simple analytical approach in order to understand the underlying physics of these systems.

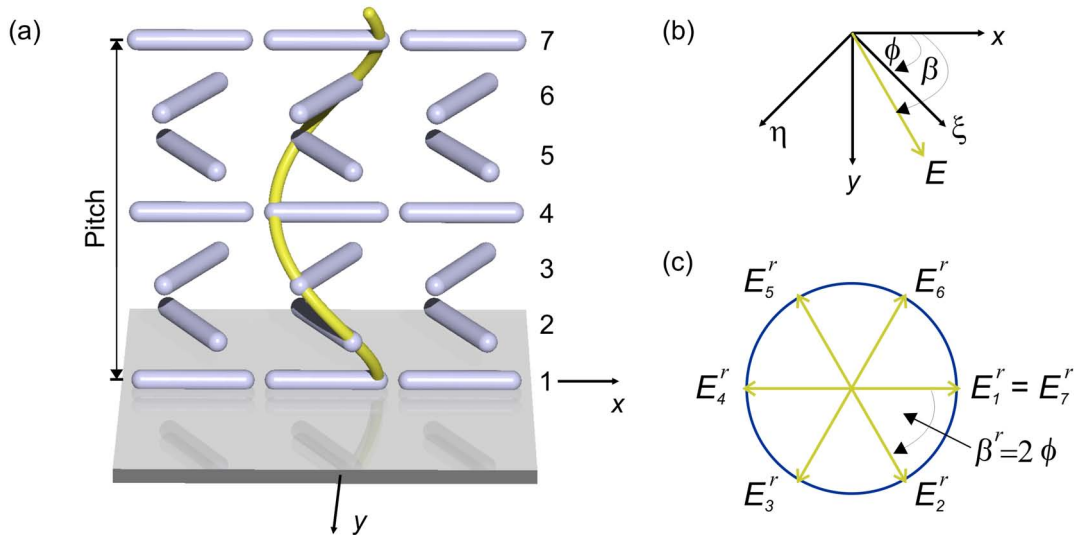


Figure 6.1: (a) Model system of a left-twisted log-pile photonic crystal. Each layer is linearly birefringent, i.e., the refractive index is different parallel to the rods compared to the perpendicular direction. In this illustration, we assume that $N = 6$ layers are stacked to a chiral lattice constant, the so-called pitch $p$ (indicated by the yellow helix with left-handedness). (b) The coordinate system $\xi - \eta$ and the angles $\alpha$ and $\beta$ are used for the derivation of the optical properties of the system. (c) The tip of the electric field of the reflected wave twists by an angle of $\beta^r$ for each successive layer.

### Physics of twisted log piles

The optical properties of log-pile photonic crystals composed of twisted anisotropic layers can be discussed analytically. A log pile with uniaxial left-handedness is depicted in Fig. 6.1 and resembles models for cholesteric liquid crystals [126]. As an example, if adjacent layers are twisted by an angle of 60°, $N = 360°/60° = 6$ layers will be necessary for a complete helical lattice constant called *pitch*. After $N$ layers, this left-handed structure obviously repeats itself.

Each layer is anisotropic because the distribution of dielectric material leads to birefringence depending on the orientation of the dielectric rods.[1] For the first layer, we denote a refractive index $n_1$ in $x$-direction and $n_2$ in $y$-direction. For the second layer, we introduce the coordinate system $\xi - \eta$ twisted by an angle of $\phi$ (as shown in Fig. 6.1(b)). The angle $\beta$ describes the in-plane orientation of the electric field vector $\vec{E}$. Neither the angle $\phi$ nor $\beta$ in Fig. 6.1(b) are yet set to a value.

What will happen if linearly polarized light impinges onto the chiral layer-by-layer photonic crystal?

[1] Please also compare section 2.2.2.

To answer this question, we examine a linearly polarized wave, which is propagating strictly in $z$-direction and impinges onto the interface between layer 1 and 2. The incident wave is written as

$$\vec{E} = \begin{pmatrix} e_x \exp(2\pi\mathrm{i}(t/T - n_1 z/\lambda)) \\ e_y \exp(2\pi\mathrm{i}(t/T - n_2 z/\lambda)) \end{pmatrix}, \tag{6.1}$$

where $e_x$ and $e_y$ are the $x$- and $y$-components of the complex electric field amplitude $\vec{e}$, and it holds $e_x = |\vec{e}|\cos(\beta)$ (compare Fig. 6.1(b)). i denotes the imaginary unit, and $\lambda$ is the wavelength of light in vacuum.

The electric field of the reflected wave reads

$$\vec{E}^r = \begin{pmatrix} e_x^r \exp(2\pi\mathrm{i}(t/T + n_1 z/\lambda)) \\ e_y^r \exp(2\pi\mathrm{i}(t/T + n_2 z/\lambda)) \end{pmatrix}, \tag{6.2}$$

and the field of the transmitted wave reads

$$\vec{E}^t = \begin{pmatrix} e_x^t \exp(2\pi\mathrm{i}(t/T - n_1 z/\lambda)) \\ e_y^t \exp(2\pi\mathrm{i}(t/T - n_2 z/\lambda)) \end{pmatrix}. \tag{6.3}$$

Here, $e_x^t = (e_\xi \cos(\phi) - e_\eta \sin(\phi))$ and $e_y^t = (e_\xi \sin(\phi) + e_\eta \cos(\phi))$ are the equations of the transmitted amplitudes taking the twist of adjacent layers into account by a rotation matrix. Then, we express the magnetic field $\vec{H}$ by the electric field:

$$\frac{\partial H_y}{\partial t} \sim -\frac{\partial E_x}{\partial z} \quad , \quad \frac{\partial H_x}{\partial t} \sim +\frac{\partial E_y}{\partial z}. \tag{6.4}$$

As usual, we employ the boundary conditions that the tangential component of the electric field and the magnetic field are continuous, and we can derive the system of equations (6.5):

$$\begin{aligned} &\text{For } E_x: && e_x + e_x^r = e_\xi \cos(\phi) - e_\eta \sin(\phi), \\ &\text{For } E_y: && e_y + e_y^r = e_\xi \sin(\phi) + e_\eta \cos(\phi), \\ &\text{For } H_x: && n_2 e_y - n_2 e_y^r = n_1 e_\xi \sin(\phi) + n_2 e_\eta \cos(\phi), \\ &\text{For } H_y: && n_1 e_x - n_1 e_x^r = n_1 e_\xi \cos(\phi) - n_2 e_\eta \sin(\phi). \end{aligned} \tag{6.5}$$

Solving this system allows for calculating a simplified relation for the amplitude of the reflected wave:

$$\vec{e}^r = \begin{pmatrix} e_x^r \\ e_y^r \end{pmatrix} = \begin{pmatrix} e\,\sin(\beta - \phi)\frac{n_1 - n_2}{n_1 + n_2}\sin(\phi) \\ e\,\cos(\beta - \phi)\frac{n_1 - n_2}{n_1 + n_2}\sin(\phi) \end{pmatrix}, \tag{6.6}$$

Here, $e = (e_x^2 + e_y^2)^{1/2}$ and the vector $\vec{e}^r$ has the length $|\vec{e}^r| = e[(n_1 - n_2)/(n_1 + n_2)]\sin(\phi)$.

Importantly, the reflected wave is obviously twisted by the angle $\beta^r = 90 - \beta + \phi$ with respect to the $x$-axis. Since the coordinate system is rotated by $\phi$ at each layer, the angle $\beta$ discretely decreases by $\phi$ for the successive layer. Accordingly, the angle of the reflected wave $\beta^r = 90 - (-\phi) + \phi$ grows by $2\phi$ at each subsequent boundary (depicted in Fig. 6.1(c) for $\phi = 30°$). Furthermore, the phase difference of two sequenced partial waves is $2nd$, where $n$ is the effective index of refraction $n = (n_1 + n_2)/2$ and $d$ the layer thickness.

The entire layer-by-layer log-pile structure (as shown in Fig. 6.1(a)) reflects at each interface one partial wave (multiple reflections are neglected). From Fig. 6.1(c), it becomes immediately clear that the reflection will be maximal if the partial wave $E_1$ is in phase with $E_7$, $E_2$ with $E_8$ etc.; hence, the relationship $2\pi/(2\phi) = \lambda/(2nd)$ holds.[2] Since the thickness of a pitch is $p = (2\pi/\phi)\, d$, we can formulate the condition of maximal reflection:

$$p = \lambda_{\text{medium}} \,, \tag{6.7}$$

where $\lambda_{\text{medium}} = \lambda/n$ is the wavelength of light in the medium.

In a gedankenexperiment, we can follow the partial waves to determine the polarization state of the reflected light. Imagine that we could detect the tip of the electric field vector of the reflected partial waves. It is rather obvious that we would detect the wave reflected from layer 1 first, the one from layer 2 second etc. Hence, the tip of the electric field vector will always move on a circle if $\phi \neq 90°$ holds. If linear polarization impinges on a left-handed twisted structure, one expects the detector to measure a signal on a counterclockwise circle, i.e., the reflected light is left-circularly polarized (compare section 2.2.1). For a right-handed structure, one detects right-circularly reflected light.[3] Notably, Fresnel reflection from a mirror changes the handedness of circular polarization.

Before we deal with the transmitted light, we first want to generalize the result for a continuous rotation of the layers (or the coordinate system $\xi - \eta$). Note that the chiral resonance is determined by the pitch $p$ and the layer thickness cancels out. Therefore, it is interesting to discuss the same situation as described above but for a continuous rotation [126]. The electric field can be written into the form

$$\vec{E} = \begin{pmatrix} e_\xi \, \cos(2\pi z/p)) - e_\eta \sin(2\pi z/p)) \\ e_\xi \, \sin(2\pi z/p)) + e_\eta \cos(2\pi z/p)) \end{pmatrix} , \tag{6.8}$$

and the following ansatz

$$\begin{pmatrix} e_\xi \\ e_\eta \end{pmatrix} = \begin{pmatrix} A \;\; \exp(2\pi \mathrm{i}(t/T - mz/\lambda)) \\ \mathrm{i}B \;\; \exp(2\pi \mathrm{i}(t/T - mz/\lambda)) \end{pmatrix} \tag{6.9}$$

[2] In the case of a pitch with 6 layers, the next possible resonance is clearly $7\lambda$.

[3] For an achiral woodpile structure (as introduced in chapter 4.2), it holds $\phi = 90°$. Therefore, this crystal does reflect linear polarization.

fulfills the wave equation (2.1), which has been discussed in chapter 2.2.

Finally, the dispersion relation of a screw-like layer-by-layer structure [126] reads

$$m^4 - m^2(\epsilon_1 + \epsilon_2 + 2\lambda^2/p^2) + (\epsilon_1 - \lambda^2/p^2)(\epsilon_2 - \lambda^2/p^2) = 0\,. \tag{6.10}$$

Here, $m$ is a unitless number taking over the role of the refractive index, and $\epsilon_{1,2}$ are the dielectric constants for the directions perpendicular and parallel to the rods, respectively. In the following, $\epsilon$ denotes the effective dielectric contrast. As an implication of equation (6.10), the inequation (6.11) defines the frequency region

$$1 - \left(\frac{\epsilon_2 - \epsilon_1}{\epsilon_1 + \epsilon_2}\right) < \frac{\lambda^2}{p^2\epsilon} < 1 + \left(\frac{\epsilon_2 - \epsilon_1}{\epsilon_1 + \epsilon_2}\right)\,, \tag{6.11}$$

where there is one real and one imaginary solution for $m$. The imaginary solution corresponds to the reflected circular polarization. The real solution propagates.

To determine the polarization state of this transmitted wave, we remind ourselves that circular polarization can be superimposed by two orthogonal linear polarizations. As discussed above, linearly polarized light is reflected circularly by the chiral layer-by-layer structure. If the structure is left-handed (right-handed), the reflection will be left-handed (right-handed). As a result, if the impinging circular polarization has the same handedness as the structure, the two circular waves (originating from the linear components of the incoming wave) are reflected in phase and with the same handedness as the incoming wave. If the impinging circular polarization has the opposite handedness as the structure, the two reflected circular waves just cancel out and the light will be transmitted.

This frequency region in which circular polarization is reflected is called ***polarization stop band***. The unmatching (matching) circular polarization is completely transmitted (reflected) in the ideal case.

An alternative explanation of the above discussion can be given by the argument that our chiral systems lack parity but not time-reversal symmetry. Importantly, left-handed (right-handed) light and left-handed (right-handed) structures keep their handedness in the time-reversed process, i.e.: If a left-handed (right-handed) structure reflects linearly polarized light with the result of left-handed (right-handed) light, this will automatically mean that left-handed (right-handed) light is reflected *selectively*. Alas, this argumentation leads to identical results.

In chapter 3, we have discussed structural color in nature showing very similar helical structures, e.g., in beetles which shine in a brilliant green. We have also pointed out that chiral reflectors have a high potential for applications. Therefore, our specific design for the layer-by-layer chiral photonic crystal, which can be viewed as an engineered complement of these biological systems, is presented next.

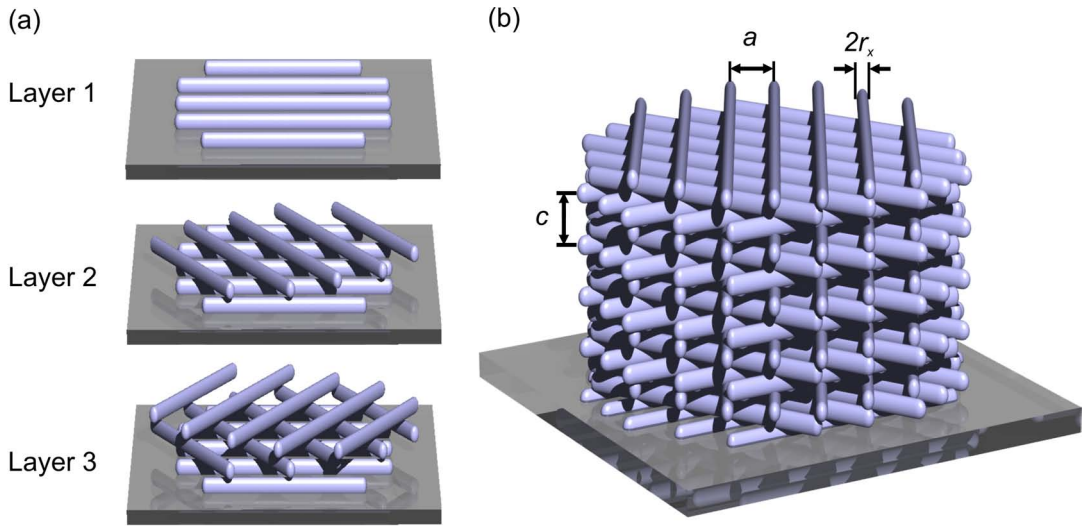


Figure 6.2: (a) Scheme of the chiral layer-by-layer photonic-crystal structure for $N=3$. Adjacent layers are twisted by 120°, i.e., 3 layers are a helical pitch. (b) Side view of the complete structure. The geometrical parameters are: $a=1.2\,\mu$m, $c=1.32\,\mu$m, $2r_x=300\,$nm, and 15 layers (5 lattice constants).

### Design

The optimized design of polymeric 3D layer-by-layer chiral photonic crystals is depicted in Fig. 6.2(a). A first layer (in air) consists of a periodic arrangement of parallel dielectric rods or bars with refractive index $n$ separated by the spacing $a$. A second identical layer is rotated by an angle of $360°/N$ and placed on top of the first layer. After an integer $N$ number of layers, the structure repeats itself, leading to the lattice constant $c$. The integers $N=1,2$, and 4 do not lead to chiral structures, whereas the choices like $N=3,5,6,7$ do. Depending on whether the stacking process is performed clockwise or counter-clockwise with respect to the substrate, one can either obtain left-handed or right-handed chiral structures. Simply speaking, the resulting 3D photonic crystal can be viewed as a "twisted woodpile" [124, 127].

The underlying physics of such chiral structures has been discussed in the previous section. We have introduced the intuitive reasoning that a polarization stop band can occur if the pitch of the dielectric chiral structure matches the pitch of the circularly polarized light, i.e., if the lattice constant $c$ matches the material wavelength of light. This means that, for a fixed operation wavelength, the fabrication requires finer features with increasing $N$. Thus, small values of $N$ are highly desirable. Furthermore, it is important to determine what refractive index $n$ is necessary for good performance. Reference [127] discussed theoretically a high-index-contrast material with refractive index $n=2.98$. In our design, we deal with a low polymeric refractive index $n=1.57$ in order to directly fabricate the photonic crystals without the need of conversion into high-index dielectrics. Also, the present "twisted woodpile" is mechanically very

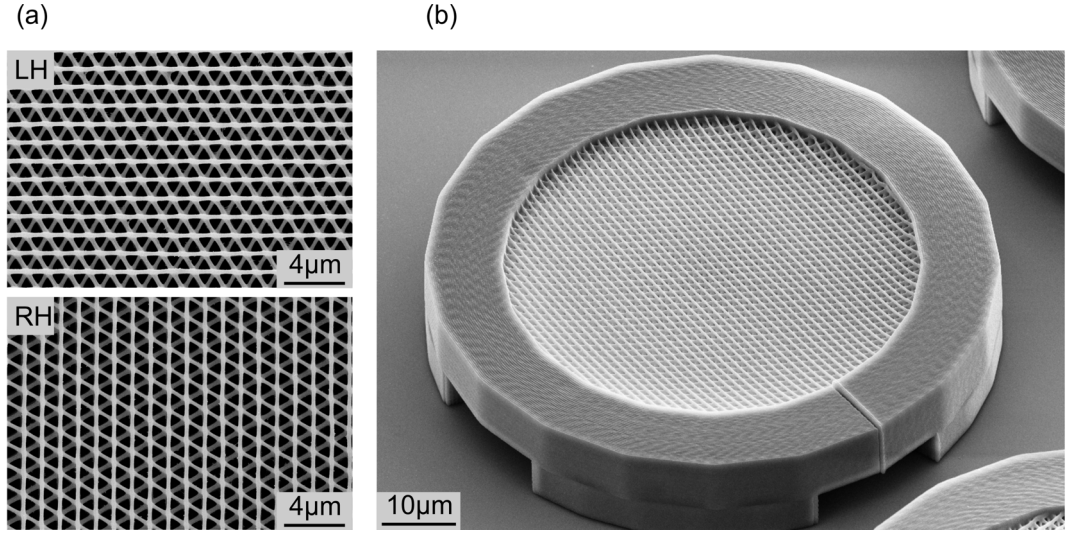


Figure 6.3: Electron micrographs of fabricated structures with the parameters given in Fig. 6.2, but with 24 layers. (a) shows top-view magnifications of left-handed (LH) and right-handed (RH) structures, respectively. (b) Oblique-view of a complete structure with an open aperture of 60 μm diameter.

robust. Therefore, for the given resolution of the DLW process, short wavelength polarization stop bands can be achieved in "twisted woodpiles"; telecommunication wavelengths are easily accessible with the layer-by-layer approach.

### Fabrication

We have fabricated our specific design (with the parameters given in Fig. 6.2, but with 24 layers) by means of DLW in the commercially available photoresist SU-8 (details are given in chapter 4.3). Electron micrographs are depicted in Fig. 6.3. The top-view magnifications of left-handed (LH) and right-handed (RH) structures reveal the handedness and the high quality. Fig. 6.3(b) is an oblique-view of a complete structure with an open aperture of 60 μm diameter showing the high homogeneity of the overall structure.[4] The structures are stabilized by a surrounding thick wall, which is intentionally written higher than the top of the photonic crystal.

### Characterization

Our numerical calculations show that excellent performance can be achieved with low refractive indices of photopolymers like SU-8 and optimized structural parameters.

[4] We emphasize, however, that this demonstration should be interpreted as a proof-of-principle. Much larger-area structures could be fabricated by repeated micro-contact printing, by hot embossing, or by other inexpensive mass-fabrication approaches.

For the calculation of transmittance spectra of finite-size structures, we employ the established scattering-matrix approach (compare chapter 5.2), and choose $n = 1.57$ and $N = 3$. Next, we search for optimum performance regarding circular dichroism by varying the $c/a$ ratio and the volume filling fraction, $f$, of the dielectric. We find that rods with circular cross section (rather than elliptical) are best. The choice is illustrated in Fig. 6.2 and corresponds to a very small ellipticity (about 1.7 aspect ratio) so that we were able to realize the structure experimentally by using two trajectories side by side for each rod. Further parameters are the ratio $c/a = 1.1$ and filling fraction $f = 23.1\,\%$.

Fig. 6.4 reveals calculated transmittance spectra for circularly polarized incident light impinging under normal incidence for the parameters of Fig. 6.2 and for 24 layers (i.e., 8 lattice constants). Pronounced polarization stop bands, centered around 1.55 µm wavelength, are clearly visible: The transmittance is about 91 % for right-handed circular incident polarization (RCP) impinging on a left-handed (LH) structure and about 2 % for left-handed circular incident polarization (LCP) and the same structure. As expected for ideal structures without unintentional linear birefringence, LCP and RCP interchange for a right-handed (RH) structure.[5]

Corresponding optical characterization[6] for $N = 3$ is shown in the right column of Fig. 6.4 which is represented as the left column to allow for a direct comparison with the theory of a perfect structure. Obviously, the overall qualitative agreement between theory and experiment is good. Specifically, the agreement in the region of the polarization stop band (gray area) is almost quantitative. On the short-wavelength side (i.e., for the higher-order bands), deviations arise which are likely due to two aspects: First, the incident light in the experiment has a finite opening angle of 5°, whereas the calculations are for strictly normal incidence affecting the spectral shape. Second, the imperfections of the fabricated samples are expected to influence the higher-order bands more strongly.

### Summary/Next steps

We have presented low-index-contrast 3D layer-by-layer chiral photonic crystals that show giant circular dichroism at telecommunication wavelengths. The underlying physics resembles models for natural occurring systems and have been discussed analytically. The proposed "twisted woodpile" can be viewed as a man-made solid mimicking biological systems acting as highly selective polarization filters. The excellent performance of the polymeric structures with only 8 pitches can directly be attributed to the high-quality fabrication via DLW. In appendix A, we (theoretically) investigate

[5] Notably, the next chiral resonance occurs at about twice the wavelength, i.e., for $\lambda = 2c$. That is because the pitch of the structure can also be interpreted as a log pile with $N = 6$ rather than $N = 3$ layers. For $N = 6$, the handedness of the structure also flips.

[6] The measurement setup for the near-infrared spectral range has been explained in chapter 5.1.

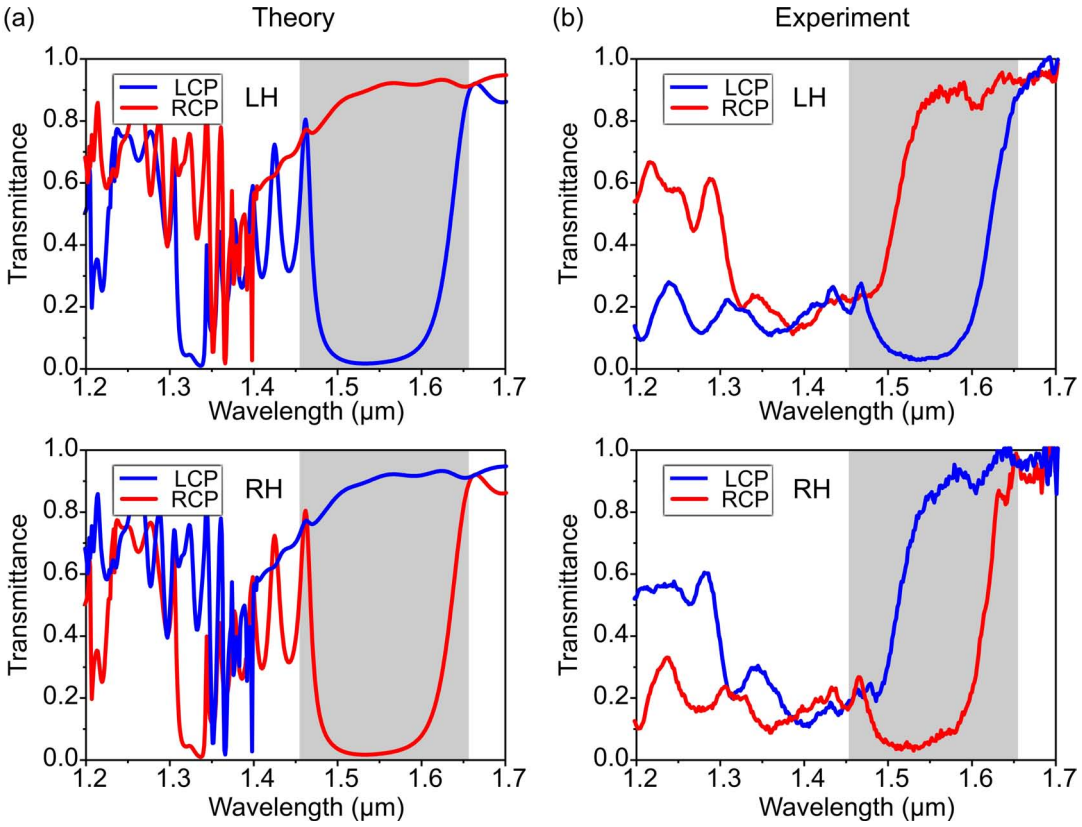


Figure 6.4: (a) Calculated normal-incidence linear-optical transmittance spectra for circular incident polarization of left-handed (LH) and right-handed (RH) structures with the parameters given in Fig. 6.2, but with 24 layers (i.e., 8 lattice constants), for left-handed circularly polarized (LCP) incident light (blue) and right-handed circularly polarized (RCP) incident light (red). (b) Measured normal-incidence transmittance spectra for circular incident polarization, represented as the corresponding calculated spectra shown in the left column.

chiral twist defects in layer-by-layer photonic crystals which may potentially serve as low threshold lasers, low loss waveguides, and narrow band filters [42].

Layer-by-layer approaches are often favorable because of a large variety of possible fabrication methods. However, we want to go further and to take advantage of the possibilities given by DLW allowing for the fabrication of arbitrary 3D nanostructures. The second blueprint discussed in the next section is only accessible with a genuine 3D microfabrication method.

## 6.2. Circular-spiral chiral photonic crystals

Chiral three-dimensional photonic crystals composed of spirals (strictly helices) are an interesting subclass of 3D photonic crystals. For example, Prof. Noda's group has predicted that large complete photonic band gaps exist for high-index-contrast silicon circular-spiral structures [41]. Corresponding 3D low-index polymeric chiral nanostructures have been fabricated by interference lithography [16] or direct laser writing [17].

However, there's another twist on these chiral structures of considerable complexity: Their handedness. Recently, in addition to complete gaps, theory also predicts polarization stop bands in circular-spiral photonic crystals [18].

In this section, we review our work on the role of chirality in circular-spiral chiral photonic crystals arranged in cubic unit cells [19, 128] because they serve as second building block for following chiral architectures. Again, we start with the explanation of the underlying physics.

### Physics of circular-spiral photonic crystals

For what conditions do we expect strong circular dichroism? For circular polarization of light, the tip of the electric-field vector simply follows a spiral. The pitch of this spiral is just the material wavelength $\lambda$. Thus, intuitively, we expect a chiral resonance from spiral photonic crystals if the pitch of circularly polarized light matches the pitch of the dielectric spirals, i.e., the lattice constant $a_z$. This condition, $\lambda/a_z = 1$, corresponds to the edge of the second Brillouin zone, i.e., to a wave number $k_z = 2\pi/\lambda = 2\pi/a_z$. Recall that the edge of the first Brillouin zone is at $k_z = \pi/a_z$. Thus, one does not anticipate a strong chiral response around and below the fundamental stop band (or band gap) but rather at higher frequencies. Theory for high-index silicon-based structures confirms this intuitive reasoning [18].[7] We have repeated similar calculations for low-index contrast polymeric structures, revealing essentially the same trends. The parameters of the 3D spiral photonic crystals to be discussed below are the result of an optimization with respect to circular dichroism.

To further investigate if this intuitive expectation is correct, we try to answer the question where the light propagates inside the structure. Fig. 6.5 shows the underlying dielectric structure together with calculated iso-intensity[8] surfaces for several relevant characteristic spectral positions (1–4, also indicated in Fig. 6.5) for both, left-handed circular polarization and right-handed circular polarization of the incident light (impinging under normal incidence with respect to the substrate). If the pitch of the light spiral inside the structure (= material wavelength) roughly matches the pitch of the dielectric spiral (= lattice constant $a_z$), the light field peaks inside the

[7] Deviations from this simple model are discussed in a following section 6.4.
[8] Details of this calculation are given in section 5.2.1.

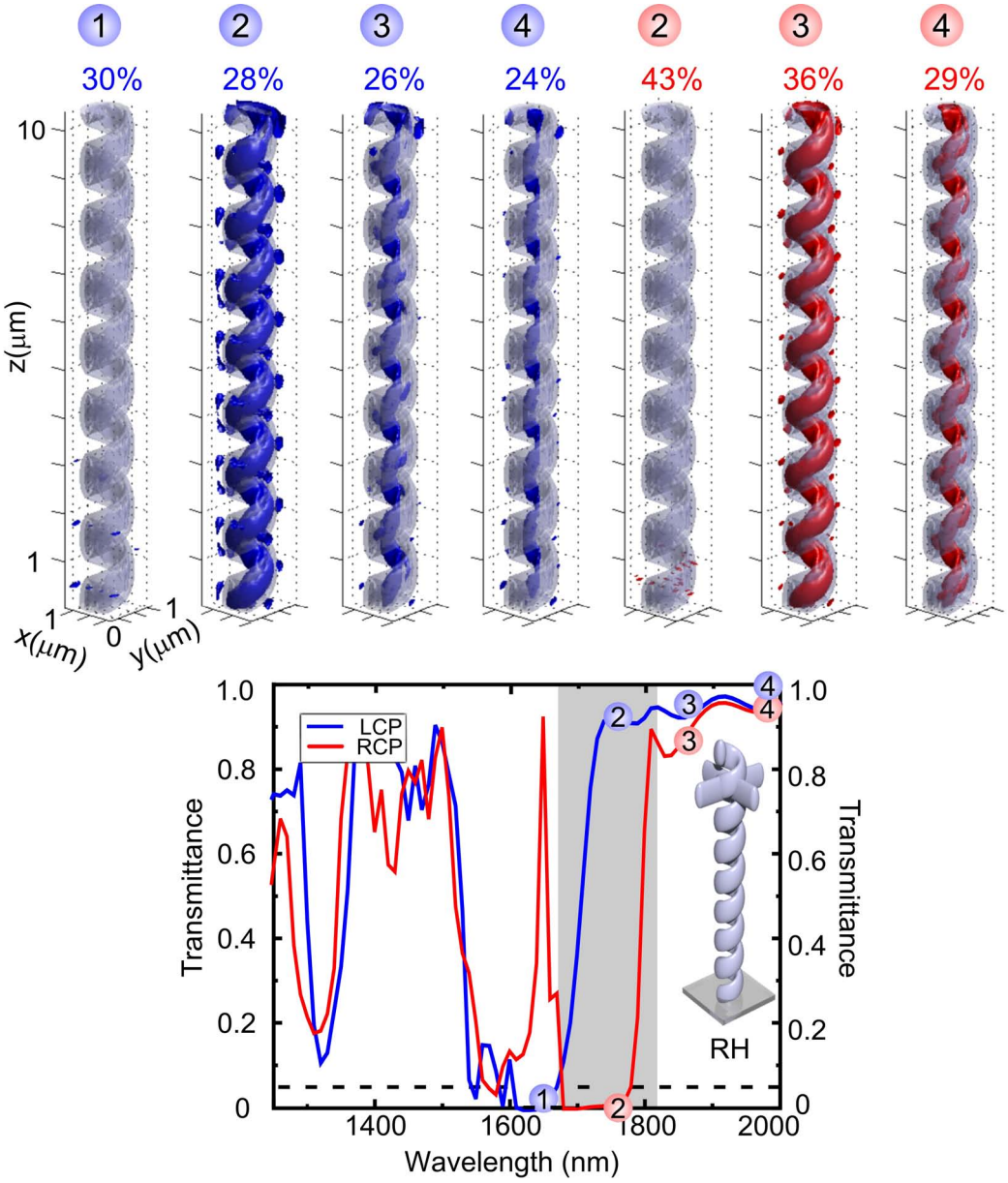


Figure 6.5: Illustration of the underlying physics. In each case, a right-handed dielectric spiral is depicted in gray. The colors used for the iso-intensity surfaces (all for 1.3 times the incident intensity of light) mark the sense of rotation of the light, i.e., red corresponds to RCP and blue to LCP. The numbers in the red and blue dots mark the spectral positions indicated in the calculated transmittance spectra of right-handed (RH) 3D chiral photonic crystals shown below. The percentages quoted on the top are the fractions of the corresponding electric energy density inside the dielectric.

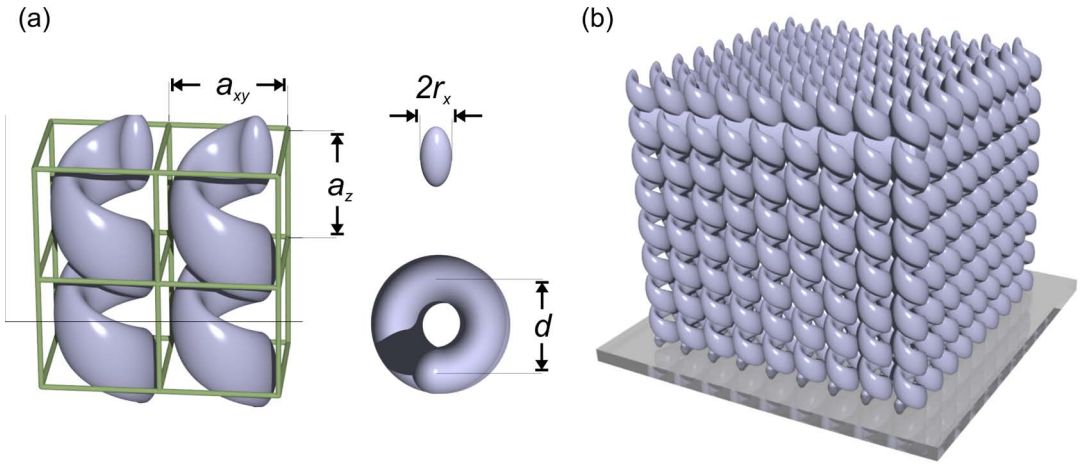


Figure 6.6: (a) Scheme of chiral circular-spiral photonic-crystal structure. The cubic unit cell is illustrated and all characteristic parameters are denoted. (b) Side view of the complete structure. The geometrical parameters are: $a_{xy} = 1.3\,\mu\text{m}$, $a_z = 1.3\,\mu\text{m}$, $2r_x = 300\,\text{nm}$, $d = 0.6a_z$, and 8 axial lattice constants.

dielectric spiral for both senses of rotation, and no immediately obvious qualitative difference arises (compare, e.g., Fig. 6.5 case 1, blue with case 2, red; case 2, blue with case 3, red etc.). Quantitatively, however, for the matching sense of rotation (red cases in Fig. 6.5), the light field is stronger confined to the dielectric as apparent from the fractions of the corresponding electric energy density inside the dielectric, indicated above the spirals in Fig. 6.5. This effect increases the corresponding effective refractive index, hence increasing the corresponding vacuum wavelength of the polarization stop band. Clearly, within the polarization stop band, the light intensity decays exponentially along the propagation direction (case 1, blue and case 2, red). Consequently, one gets a polarization stop band for each of the two circular polarizations. The short-wavelength polarization stop band is obviously not attractive for applications because the transmittance in the opposite circular polarization does not come close to unity (only a narrow peak is observed that is strongly depend on the angle of incidence). The results for left-handed dielectric spirals are analogous with the role of LCP exchanged by RCP and vice versa (not shown).

### Design

The scheme of our design of polymeric circular-spiral chiral photonic crystals is shown in Fig. 6.6. The spirals are arranged in cubic unit cells, i.e., $a_{xy} = a_z$. Sample parameters are: in-plane lattice constant $a_{xy} = 1.3\,\mu\text{m}$, pitch $a_z = 1.3\,\mu\text{m}$, spiral diameter $d = 0.78\,\mu\text{m}$, 34.7 % volume filling fraction, lateral diameter of the spiral arms $2r_x = 380\,\text{nm}$, ratio between axial and lateral diameter = 2.7, and $N = 8$ lattice constants along the $z$-direction (see Fig. 6.6(a) for the denotation). These parameters are

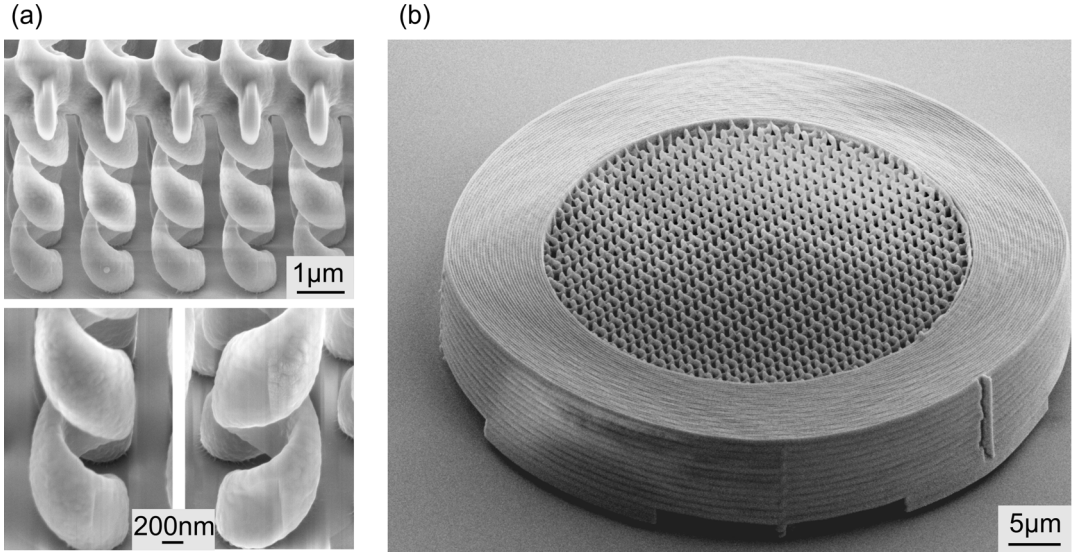


Figure 6.7: Gallery of fabricated 3D spiral photonic crystals. (a) Close-up of the inside of a left-handed structure with $a_{xy} = a_z = 1.5\,\mu\text{m}$, $d = 0.6a_z$, and $N = 4$, made accessible by focused-ion-beam cutting. Below, zoom-in onto one of the left-handed spirals and onto a similar, but right-handed spiral (with equal parameters), respectively. (b) Oblique-incidence overview of a sample with $N = 8$ lattice constants in $z$-direction used for the measurements in Fig. 6.8. All the sample parameters are given in Fig. 6.6.

optimized for strong circular dichroism taking into account the resolution of DLW. Depicted in Fig. 6.6(b) is a side view of the complete structure we want to fabricate.

### Fabrication

After optimization of the design, we have fabricated the structures by means of DLW in the commercially available photoresist SU-8. A small gallery of selected electron micrographs is depicted in Fig. 6.7, which gives first evidence that the sample quality is very good. To demonstrate the versatility of our approach, Fig. 6.7(a) exhibits a cut of a structure with $a_{xy} = 1.5\,\mu\text{m}$, $a_z = 1.5\,\mu\text{m}$, and $\text{N} = 4$. As the focused-ion-beam cut was stopped in between two rows of spirals, a stabilizing network is revealed. Our structures are mechanically supported by this two-dimensional network of bars at or close to the top of the 3D crystal. As the spirals are not mechanically connected to their neighbors, very unstable low-quality structures result without this grid. Furthermore, Fig. 6.7(a) also shows close-ups of a single left-handed spiral and a single right-handed spiral from a sample fabricated with identical parameters but opposite handedness. All structures for optical experiments have the parameters given in the caption of Fig. 6.6 and are surrounded by a thick massive wall, which aims at reducing the effects of strain on the two-dimensional grid due to photoresist shrinkage

during development. Again, we use a round wall in order to evenly distribute strain inside the wall. We have confirmed by numerical calculations (see below) that the two-dimensional network marginally distorts the optical properties. In particular, it does not introduce any chirality. Fig. 6.7(b) gives an overview of one of the samples to be optically characterized next.

### Characterization

The left column of Fig. 6.8 shows measured transmittance spectra of 3D circular-spiral photonic crystals with identical parameters as the one shown in Fig. 6.6(b), for both left-handed and right-handed dielectric circular spirals and for both left-handed and right-handed incident circular polarization of light. As expected from the symmetry, the transmittance spectra are nearly the same if both the sense of rotation of the dielectric spirals and that of the incident light field are changed simultaneously. Around 1.8 μm wavelength, the transmittance in the "low state" is around 5 % compared to about 95 % in the "high state", corresponding to a ratio approaching twenty.

The right column of Fig. 6.8 exhibits the calculated transmittance spectra corresponding to the experiment. The geometrical parameters are the same as in the experiment. In particular, we account for the ellipsoidal shape of the voxels in the DLW fabrication. The refractive indices used for SU-8 and the glass substrate are $n_{\mathrm{SU-8}} = 1.57$ and $n_{\mathrm{glass}} = 1.52$, respectively. To mimic the finite opening angle of the focused incident light in the experiments, the calculated transmittance spectra are averaged over an angle of 7° with respect to the normal. Notably, the overall agreement between experiment and theory is good. In particular, the relative handedness of light and structure, the spectral position of the polarization stop band, and the depth of the transmittance minima are reproduced very well. Quantitative deviations between experiment and theory arise at wavelengths below the polarization stop band, where many different photonic bands contribute. Moreover, one should be aware that the angle-averaging also influences the detailed shape of the spectra. For example, for the strict normal-incidence case (i.e., without any angle-averaging at all) the calculated transmittance minimum in the polarization stop band is as low as 0.1 % for the identical $N = 8$ structure (see Fig. 6.5).

### Summary/Next steps

In conclusion, we have reviewed our work on the second chiral building block: circular spirals [19, 128]. The obtained giant circular dichroism from polarization stop bands is comparable to that of polymeric 3D layer-by-layer chiral photonic crystals demonstrated in section 6.1. Additional information and characterization of chiral circular-spiral photonic crystals are given in appendix B and reference [128], including measurements of the angle dependence of the polarization stop band.

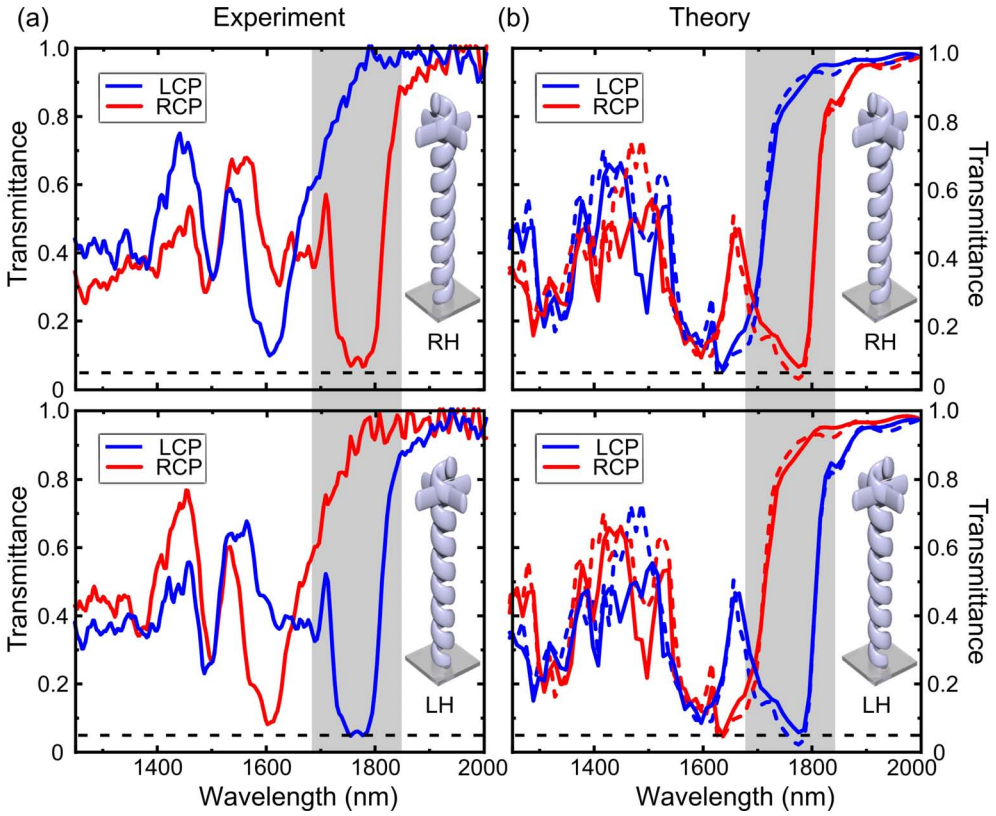


Figure 6.8: (a) Measured transmittance spectra of 3D chiral photonic crystals with right-handed (RH) and left-handed (LH) dielectric spirals. Transmittance spectrum for right-handed RCP (left-handed LCP) circular polarization of the incident light is shown in red (blue). The dashed horizontal lines correspond to a level of 5 % transmittance. (b) Calculated transmittance spectra of 3D spiral photonic crystals. Parameters and representation correspond to the experiment. The dashed colored curves are calculations without the stabilizing grid near the top.

Although both approaches have shown excellent experimental results, we focus on the circular-spiral building block in our further studies. Our next aim is to find potential future applications of chiral photonic crystals. While striking experimental demonstrations based on cholesteric liquid crystals have been published recently [4], corresponding experimental work on artificial dielectric solid structures could offer much more freedom in tailoring the optical properties. Therefore, we present some interesting optical devices based on tailored man-made solid crystals in the next section.

## 6.3. Thin-film optical devices based on chiral photonic-crystal heterostructures

The above experimental demonstration of polarization stop bands in three-dimensional dielectric circular-spiral photonic crystals is extended in two ways [20]. First, the combination with a one-dimensional set of lamellae on one side allows for "poor-man's" optical isolators or for thin-film polarizers — depending on from which side light impinges onto the device. Secondly, a chiral three-dimensional photonic crystal sandwiched between two one-dimensional sets of lamellae acts as a thin-film polarizer from both sides.

### Underlying idea

Polarization stop bands can be used as "poor-man's" optical isolators for circularly polarized incident light: If, for example, right-handed polarized light from a laser impinges onto the structure, it is transmitted for a spiral photonic crystal composed of left-handed dielectric spirals. Upon back-reflection from a mirror behind the spiral photonic crystal, the backward propagating light has left-handed circular polarization. As the spirals keep their handedness when looked at from the other side, the light is not transmitted, hence, blocked from propagating back into the laser source. This device is only a "poor man's" isolator because it will fail to isolate if the polarization state of light is changed behind the device — which is in sharp contrast to non-reciprocal optical isolators based on the Faraday effect.

Furthermore, the combination of a chiral photonic crystal and a quarter-wave plate clearly acts as a polarizer. In contrast to commercially available thin-film polarizers based on one-dimensional dielectric stacks and Brewster's angle [129], such heterostructure can work for normal incidence of light. If the device is used in the opposite direction, i.e., if linearly polarized incident light (oriented 45° with respect to the principal axes of the quarter-wave plate) first hits the quarter-waveplate and subsequently the chiral photonic crystal, the overall structure acts as a poor man's optical isolator for linear incident polarization of light. Furthermore, a chiral photonic crystal sandwiched between two crossed quarter-wave plates can act as a linear polarizer from both sides.

### Design

To obtain compact and monolithic devices, it is desirable to integrate the chiral photonic crystal with one (or two) quarter-wave plates. The physics of the chiral building block — circular-spiral photonic crystals — have been described in section 6.2. The quarter-wave plates are one-dimensional (1D) periodic sets of lamellae, leading to form birefringence in the long-wavelength limit. A plot of the calculated phase retardation versus lamellae height $h$ and wavelength is depicted in Fig. 6.9(c). The lattice con-

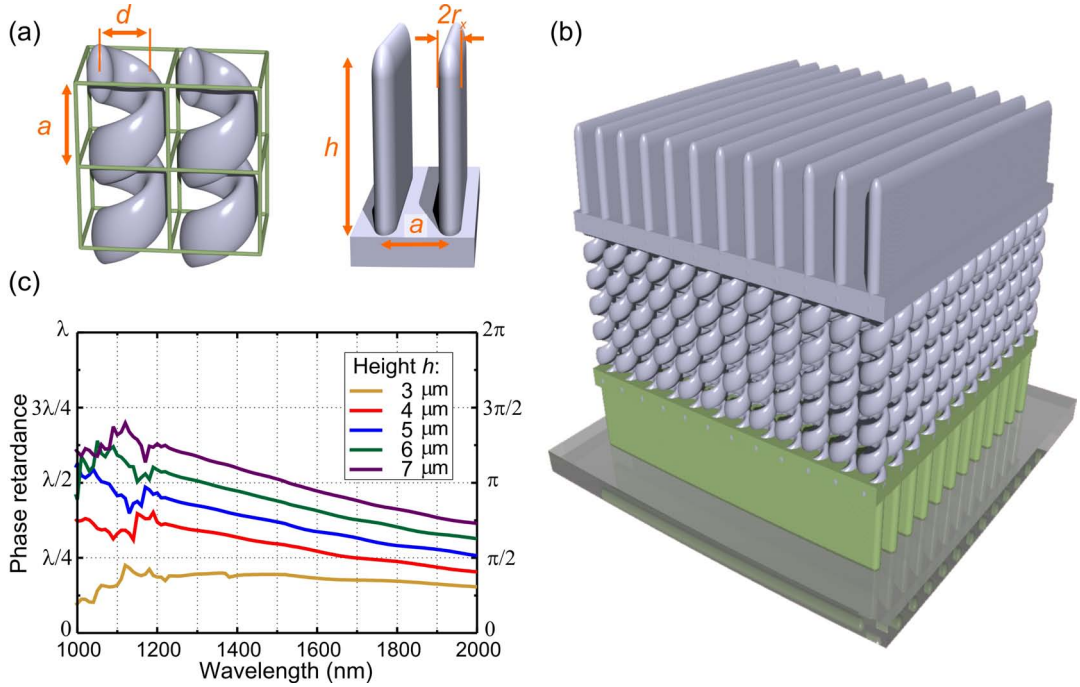


Figure 6.9: (a) Top: Definition of parameters of the structure on the right-hand side. Bottom: The phase retardation is plotted as a function of wavelength and lamellae height. (b) Proposed 1D-3D (blue) and 1D-3D-1D (blue and green) photonic-crystal heterostructure composed of a three-dimensional right-handed (RH) spiral photonic crystal with $N = 6$ pitches and one or two one-dimensional sets of lamellae, respectively.

stants of the 3D and the 1D structures, respectively, do not need to be identical but choosing the same lattice constant is possible and eases the theoretical calculations, hence the detailed design. Fig. 6.9 shows the two types of heterostructures discussed above. In what follows, we emphasize the 1D-3D-1D heterostructure, the 1D-3D heterostructure yields very similar spectra. Parameters are: $a = 1.3\,\mu\text{m}$, $d = 0.78\,\mu\text{m}$, $h = 3.7\,\mu\text{m}$, $2r_x = 0.44\,\mu\text{m}$, and $N = 6$. The volume filling fraction of the spirals in the cubic unit cell is 32.1 %. Again, these parameters result from an optimization acknowledging the fabrication restrictions of DLW. The thickness of each of the two plates (introduced for mechanical stability) between the spiral crystal and the sets of lamellae is 0.93 µm. The complete 1D-3D-1D heterostructure has a height of only 17 µm.

### Fabrication

To validate our discussion, we have fabricated the 1D-3D as well as the 1D-3D-1D structure again using our DLW setup and the thick-film photoresist SU-8. The design and geometrical parameters are denoted in Fig. 6.9. The following discussion of the

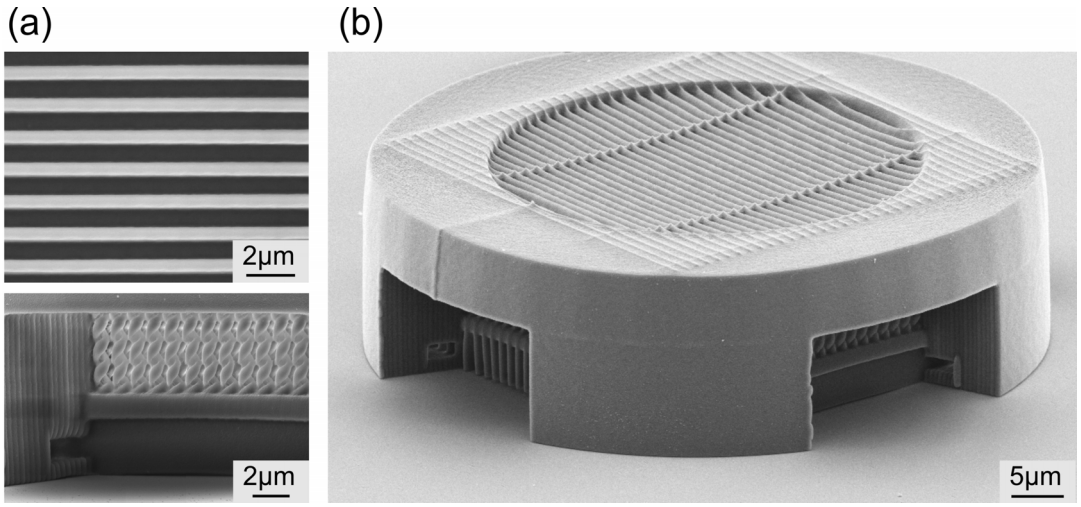


Figure 6.10: Electron micrographs of the fabricated heterostructure. (a) Top: Normal-incidence close-up view onto the top set of lamellae. Bottom: Close-up revealing parts of the 3D spiral crystal (RH), one of the stabilizing plates, the bottom lamellae, and the surrounding wall with one of the drains (left bottom) allowing for developer circulation. (b) Glancing-angle incidence view of the entire structure.

optical properties focuses on the more complex 1D-3D-1D case, electron micrographs of which are shown in Fig. 6.10. Note the high quality of the set of lamellae and the spirals, respectively.

### Characterization

The calculated optical response of a 1D-3D-1D heterostructure is depicted in Fig. 6.11(a). This calculation refers to normal incidence onto the structure illustrated in Fig. 6.9(b) and assumes a refractive index $n = 1.57$ for the polymer. The structure is located on a glass substrate with refractive index $n = 1.518$. Linear optical (intensity) transmittance spectra are shown for the two incident linear polarizations including +45° and -45° with respect to the lamellae, respectively. Here, +45° leads to left-handed circular polarization (blue), -45° to right-handed circular polarization (red). Obviously, the transmittances are different by about a factor of 50. The polarization state emerging from the device is very close to linear and parallel to the incident linear polarization. This becomes evident from the top part of Fig. 6.11(a) where we analyze the emerging polarization state at the operation wavelength of 1.72 µm indicated by the blue dot. The performance of the 1D-3D heterostructure is quite similar, except that circular polarization is emerging from the device (not shown).

Optical characterization for incident linearly polarized light is also shown in Fig. 6.11 For linear incident polarization oriented +45° with respect to the lamellae, a trans-

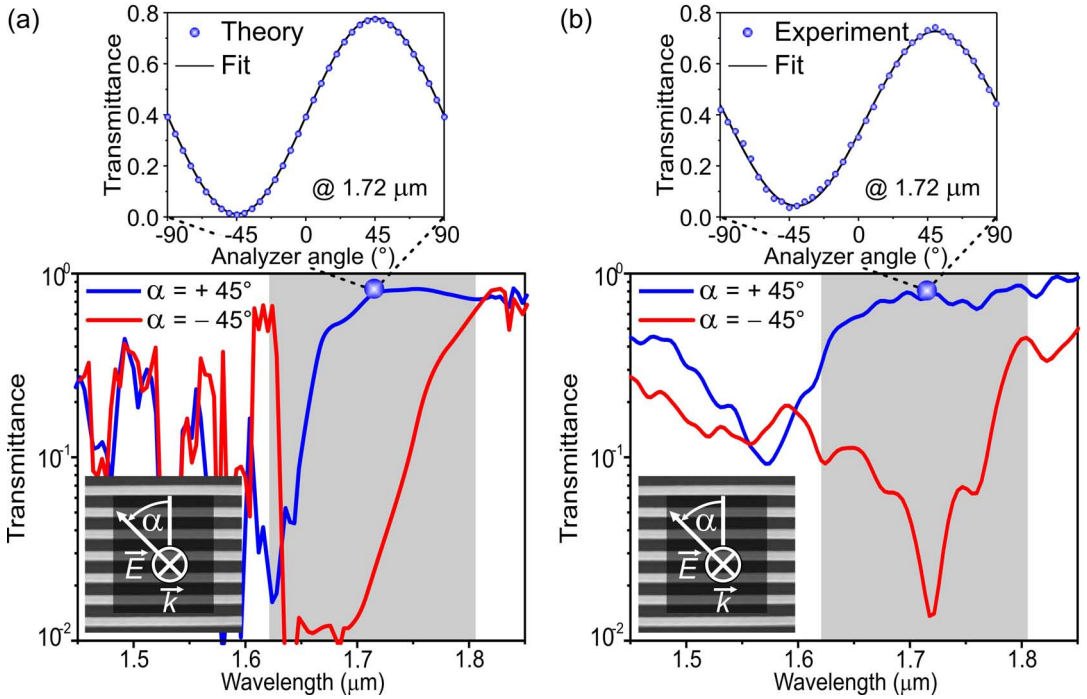


Figure 6.11: (a) Calculated normal-incidence transmittance spectra (logarithmic scale) of the 1D-3D-1D heterostructure (shown in Fig. 6.9(b)). The linear incident polarization is oriented $\alpha = +45°$ (blue) and $\alpha = -45°$ (red) with respect to the lamellae, respectively (see inset). Pronounced differences occur in the region of the polarization stop band (gray area). The corresponding transmittance ratio at 1.72 µm wavelength is about 50. The emerging polarization of light at this wavelength is analyzed in the upper part. (b) Measured transmittance spectra. Experimental data obtained from the structure shown in Fig. 6.10, represented in the same format as the theory.

mittance close to 78 % is observed at 1.72 µm wavelength, whereas the transmittance is around 1.5 % for -45° polarization. Thus, the suppression factor is 52 (17.2 dB). Furthermore, the polarization state of the light emerging from our thin-film optical isolator is very close to linear as determined by rotating a Glan-Thomson polarizer behind the sample (see top of Fig. 6.11(b)). The fit (solid) to the data reveals a dependence of the transmittance $T$ according to $T = 0.044 + 0.683 \cdot \cos^2(\varphi)$, where $\varphi$ is the analyzer angle. The overall measured behavior is in good agreement with the numerically calculated response. In particular, the spectral position as well as the depth of the polarization stop bands (gray areas) agree well. Regarding deviations with respect to the spectral shape, one should be aware again that the experiment introduces a certain angle averaging. In contrast, the theory refers to strictly normal incidence. Deviations from perfect linear polarization of the emerging light are likely due to sample imperfections. Nevertheless, we can conclude that the quality of the fabricated structure is very high and that the concept is valid.

### Asymmetric transmission in chiral thin films versus Faraday isolators

As pointed out, the 1D-3D-1D heterostructure acts as a polarizer. Furthermore, it also acts as an optical diode in the following sense: Light impinging with a linear polarization oriented $\alpha = +45°$ with respect to the lamellae is transmitted for the geometry discussed above. If we now turn around the device by 180° such that the new incident linear polarization corresponds to $\alpha = $-45° with respect to the lamellae on the new front side, the light is *not* transmitted.

The system described by the Jones formalism[9] reads

$$\vec{J}_2 = \begin{pmatrix} T_{11} & T_{12} \\ T_{21} & T_{22} \end{pmatrix} \vec{J}_1 \,. \tag{6.12}$$

For the 1D-3D-1D heterostructure, the corresponding $T$-matrix is $T = T_1 \cdot T_2 \cdot T_3$, i.e., we obtain for the case where linear incident polarization is oriented $\alpha = +45°$ with respect to the lamellae (blue curve of the spectra shown in Fig. 6.11):

$$\vec{J}_2 = \frac{1}{c} \begin{pmatrix} 1+i & 0 \\ 0 & 1-i \end{pmatrix} \begin{pmatrix} 1 & -i \\ i & 1 \end{pmatrix} \cdot \begin{pmatrix} 1-i & 0 \\ 0 & 1+i \end{pmatrix} \cdot \begin{pmatrix} 1 \\ 1 \end{pmatrix} = \frac{1}{\sqrt{2}} \begin{pmatrix} 1 \\ 1 \end{pmatrix} ,$$

where $T_3$ corresponds to a quarter-wave plate with the fast axis in $x$-direction, $T_2$ to the right-handed circular-spiral photonic crystal, and $T_1$ to a quarter-wave plate in $y$-direction, and $c$ is a constant securing normalization of the resulting Jones vector. As suspected, the emerging polarization is linear again (compare upper part of the calculated and measured transmittance spectra in Fig. 6.11).

In the corresponding calculation for the device turned by 180° such that the new incident linear polarization corresponds to $\alpha = $-45° with respect to the lamellae on the new front side (red curve of the spectra shown in Fig. 6.11) the sequence of Jones matrices is changed to:

$$\vec{J}_2 = \frac{1}{c} \begin{pmatrix} 1-i & 0 \\ 0 & 1+i \end{pmatrix} \begin{pmatrix} 1 & -i \\ i & 1 \end{pmatrix} \cdot \begin{pmatrix} 1+i & 0 \\ 0 & 1-i \end{pmatrix} \cdot \begin{pmatrix} 1 \\ 1 \end{pmatrix} = \begin{pmatrix} 0 \\ 0 \end{pmatrix} .$$

Obviously, light is not transmitted anymore and the heterostructure acts as an optical diode. Note that the Jones matrix of the helix does not change because the handedness does not change either. Moreover, the devices does not act as an optical diode for all orientations of the optical axis of the quarter-wave plates relative to the optical table, on which the optic is mounted. However, the concept of an optical diode for circular polarization based on cholesteric liquid crystals is presented in reference [4]. These devices are based on chiral reflectors and half-wave plates. They do not depend on the optical axis of the device and can also be fabricated along the lines presented above.

[9] Compare chapter 2.2.1.

Unfortunately, this behavior of "asymmetric transmission" of an optical diode is *not* equivalent to that of an optical isolator (compare section 3.3.1). This would require that light transmitted by the device and back-reflected from a mirror behind the device does not propagate back into the laser source. To the best of our knowledge, neither dielectric nor metallic chiral nanostructures act as "bulletproof" optical isolators in linear optics and without the help of an external magnetic field.

#### Summary/Next steps

In conclusion, we have proposed, fabricated, and characterized photonic heterostructures composed of chiral circular-spiral photonic crystals and 1D sets of lamellae acting as quarter-wave plates. These heterostructures can serve as thin-film polarizers, "poor-man's" optical isolators, and as optical diodes in the sense defined above. More applications based on similar ideas have been theoretically proposed in literature, e.g., a color-separating system for optical projectors [130].

The circular-spiral building block has turned out to be a very interesting candidate for applications. Therefore, we decided to have a closer look at this important building block. In particular, we want to study the importance of the arrangements of the spirals in the photonic-crystal lattice.

## 6.4. Three-dimensional chiral photonic superlattices

To obtain deeper insight in the physics of our second building block, we investigate three-dimensional photonic superlattices composed of polymeric helices in various spatial checkerboard-like arrangements. Depending on the relative phase shift and handedness of the chiral building blocks, different circular-dichroism resonances appear or are suppressed. Samples corresponding to four different configurations are fabricated and characterized.

#### Underlying idea

The resonances in chiral dielectric structures have been interpreted following the lines of cholesteric liquid crystals: A resonance occurs if the helical pitch equals the effective material wavelength. In this simple intuitive picture, which is essentially based on individual spirals, the interaction between adjacent spirals is completely neglected. Therefore, we aim at investigating these lateral interactions in photonic superlattices. To allow for an unambiguous interpretation, we only change the relative phase of neighboring spirals or their handedness.

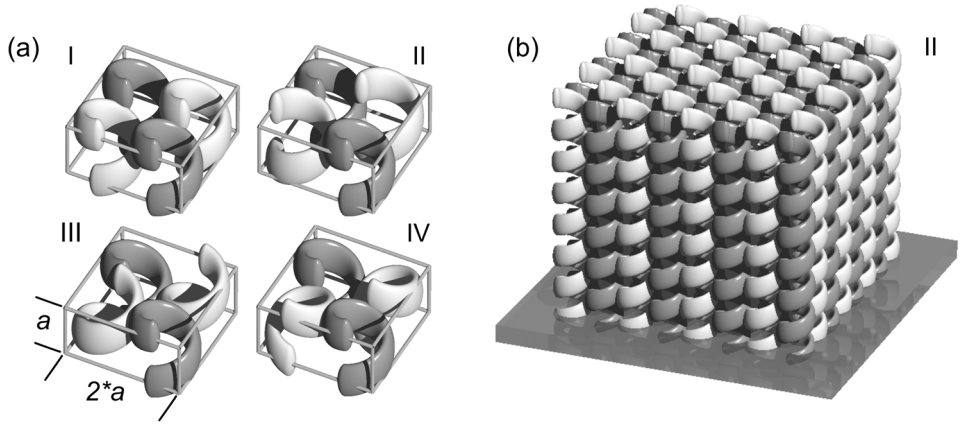


Figure 6.12: (a) Four configurations of chiral photonic crystals: Spirals with same handedness are in phase (I), 90° out of phase (II), and 180° out of phase (III). Configuration IV is a racemic mixture of helices. Each spiral is situated in a cubic unit cell with lattice constant $a$. (b) Oblique view on a chiral photonic superlattice of configuration II with $N = 7$ axial periods.

### Design

The geometry of our model system is illustrated in Fig. 6.12. All extended unit cells are composed of four spirals with the same structural parameters but varying phase or handedness in a checkerboard-like manner. While four spirals with the same handedness are laterally arranged in case I, they are phase-shifted by 90° in case II, and by 180° in case III. These cases are enantiopure configurations. In case IV, the handedness alternates, resulting in a racemic mixture of chiral helices. The distance between adjacent spirals $a$ and the spiral diameter $L = 0.9a$ are fixed. $2a$ is the in-plane lattice constant. These extended unit cells are stacked to a 3D photonic crystal with $N = 7$ axial lattice constants. As an example, the resulting structure of case II is shown in Fig. 6.12(b).

### Fabrication

To fabricate such complex photonic superlattices, we again expose the negative-tone photoresist SU-8. The parameters are $a = 3.25\,\mu\text{m}$, $L = 2.925\,\mu\text{m}$, and a volume filling fraction of 36.5 %. All fabricated structures have a footprint of $65\,\mu\text{m} \times 65\,\mu\text{m}$ and have been fabricated under identical conditions on the same glass slide. Top-view electron micrographs of each superlattice are depicted in 6.13(a). The four different configurations correspond to those shown in 6.12. To demonstrate the high quality and homogeneity, an oblique view of a circular-spiral photonic crystal of case II is shown in Fig. 6.13(b).

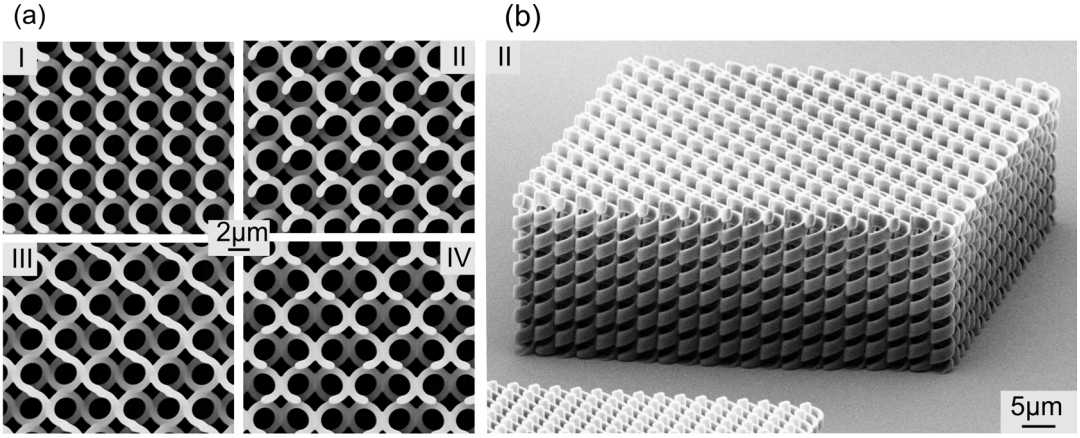


Figure 6.13: (a) Top-view electron micrographs of fabricated circular-spiral photonic crystals in the same order as shown in Fig. 1. (b) Oblique-view electron micrograph of a polymer structure of configuration II fabricated by DLW. The cubic lattice constant of all structures is $a = 3.25\,\mu m$, their footprint is $65\,\mu m \times 65\,\mu m$, and they contain seven lattice constants normal to the glass substrate plane. Each spiral diameter is $L = 0.9a$.

### Characterization

The optical properties of the chiral photonic crystals of case I have been discussed in detail in section 6.2. The resulting polarization stop bands have been interpreted intuitively following the above simple picture. In this picture, the optical properties of cases I-III should be identical. In contrast, the chiral effects are expected to disappear in case IV.

Measured optical transmittance spectra of the sample shown in Fig. 6.13 are shown in Fig. 6.14 (left column). All spectra are taken by using a Fourier-transform microscope-spectrometer (compare chapter 5.1).

Case I reveals the previously discussed polarization stop band for circular polarization centered around 4.3 µm. The details are different because the adjacent spirals slightly overlap in this section, whereas they have been well separated previously. Here, we have chosen overlapping spirals in order to ensure mechanical stability without the need for additional stabilization (grids and wall, see section 6.2). In contrast to case I, the optical properties of cases II and III considerably differ from the expectations from the simple picture. In particular, in both cases, a second additional set of longer wavelength resonances appears. Again, the stop band depends on the circular polarization leading to circular dichroism. Furthermore, in case III, the original polarization stop band has been strongly suppressed, whereas it is still visible in case II. Alas, the above simple picture taken from cholesteric liquid crystals is not sufficient to describe the observed behavior, especially the additional longer-wavelength resonance. Interestingly, this additional stop band occurs at a wavelength that is about a factor $\sqrt{2}$

larger than that of the original polarization stop band. This factor correlates with the in-plane distance between adjacent equivalent spirals which is $a$ in case I and $\sqrt{2}a$ in cases II and III. Finally, the racemic mixture (case IV) hardly shows any chiral response. Nevertheless, the longer-wavelength stop band also seen in cases II and III is still present.

To further investigate the optical properties and to rule out experimental artifacts, we perform numerical calculations. We choose normally incident circular polarization of light (blue for left-circular and red for right-circular), a polymer refractive index of $n = 1.57$, a refractive index of the semi-infinite glass substrate of $n = 1.518$, and the geometrical structure parameters of the fabricated structures shown in Fig. 6.13. In particular, we also account for the elongated point-spread function of DLW (aspect ratio of 2.7).

Since the extended unit cells might potentially lead to a slow convergence rate in the numerics, we investigate this aspect here in more detail. The lateral and axial discretization of each unit cell is set to $a/128 = 25.4\,\text{nm}$. We use $g = 7$ orders corresponding to $(2g + 1)^2 = 225$ reciprocal lattice vectors. Normal-incidence intensity transmittance refers to the (0,0) diffraction order. The transmittance differences between $g = 7$ and $g = 8$ are within the linewidth of the shown curves (smaller than 0.015), indicating that the numerical results converge.[10] The results are shown in the right column of Fig. 6.14, allowing for a direct comparison with experiment in the other column.

The overall agreement between theory and experiment is good. Specifically, the spectral positions of the stop bands and the depth of the transmittance minima are reproduced quite well. Remaining deviations likely arise from slight imperfections of the fabricated structures and/or from the finite opening angle of the measurement apparatus.

### Summary/Next steps

In conclusion, we have presented 3D chiral photonic superlattices composed of different checkerboard-like arrangements of polymer spirals. The chiral-optical properties strongly depend on the in-plane arrangement of the spirals rather than solely on the spiral parameters. This observation highlights the differences in the physics of cholesteric liquid crystals and helical photonic crystals.

Furthermore, this opens new design options for tailoring the optical properties of these artificial chiral structures. In our case, the question arose if one could arrange the circular spirals even more complicated to achieve chirality along each spatial direction. This novel concept of triaxial 3D chiral photonic crystals is investigated in the next chapter.

[10] As we find the evaluation of the numerical convergence important, this aspect has also been discussed in section 5.2.1.

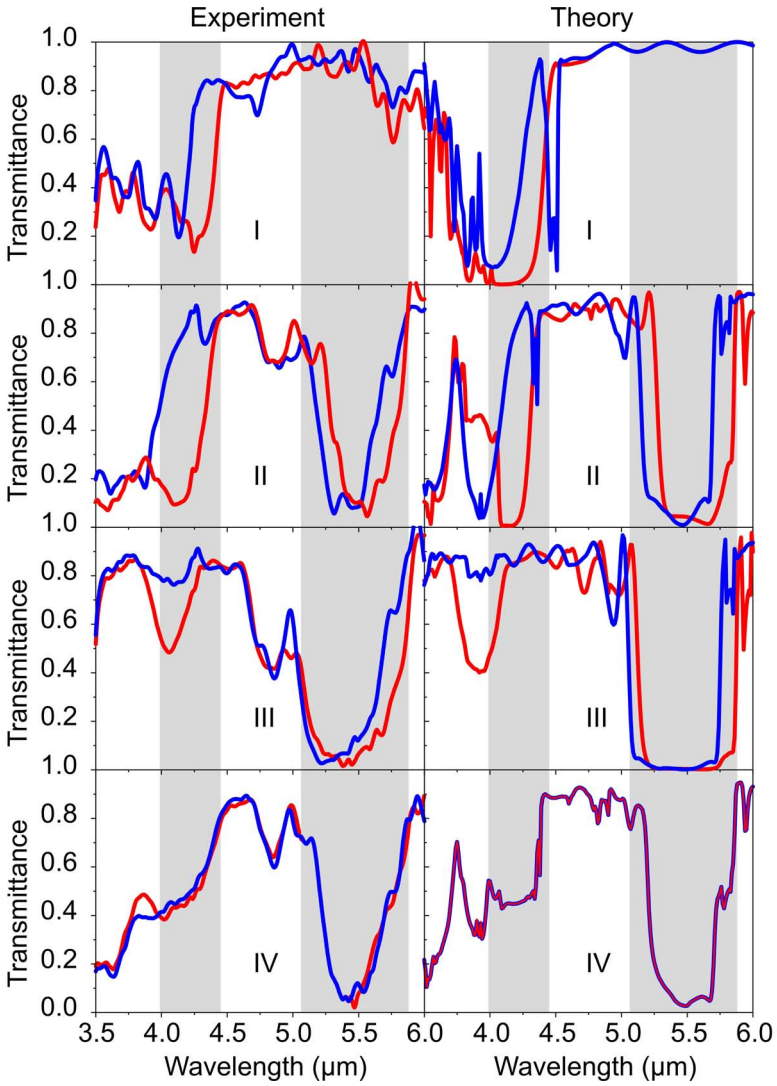


Figure 6.14: Transmittance spectra of the samples shown in Fig. 6.13 taken/calculated under normal incidence for circular polarization of the incident light. Left-handed circular polarization (blue) and right-handed circular polarization (red) of the incident light are shown for all four different configurations (I-IV). The gray areas highlight stop bands for circular polarization or polarization-independent stop band.

# 7. Triaxial three-dimensional chiral photonic crystals

Up to now, all investigated chiral photonic crystals were uniaxial, i.e., they possessed *one* helical axis. Likewise, the vast majority of publications have only discussed uniaxial artificial chiral structures.[1] This low symmetry introduces a pronounced directional dependence of the chiral-optical properties which can be undesired for certain applications.

In this chapter, we combine the achievements of the last chapters and introduce triaxial chiral photonic crystals. We aim at boosting chiral effects in these tailored man-made crystalline materials, while avoiding uniaxial structures and maintaining isotropy as far as possible.

## 7.1. Three-dimensional bi-chiral photonic crystals

The architectures that we propose and realize are inspired by so-called blue phase of cholesteric liquid crystals [75–78], which come fairly close to our aim (compare section 3.2). Our structures consist of left- or right-handed circular dielectric spirals that are arranged along the three orthogonal spatial axes of a cubic lattice with left- or right-handed so-called corners. Because of the two types of chirality, we refer to these structures as being "bi-chiral". Out of altogether four possible bi-chiral structures, nature only provides those with opposite handedness, that is, left-handed motifs on right-handed corners and vice versa.

Our structures, unlike blue-phase liquid crystals, can in principle be tuned to any desired operation wavelength. More importantly, our approach to fabricate artificial chiral photonic crystals by using DLW give access to all four possible bi-chiral combinations.

[1] A notable exception is a 3D arrangement of pieces of metal spirals with random orientation in three dimensions that has been demonstrated at microwave frequencies [131]. The random orientation, however, leads to some degree of inherent scattering which can be avoided in periodic structures ("crystals").

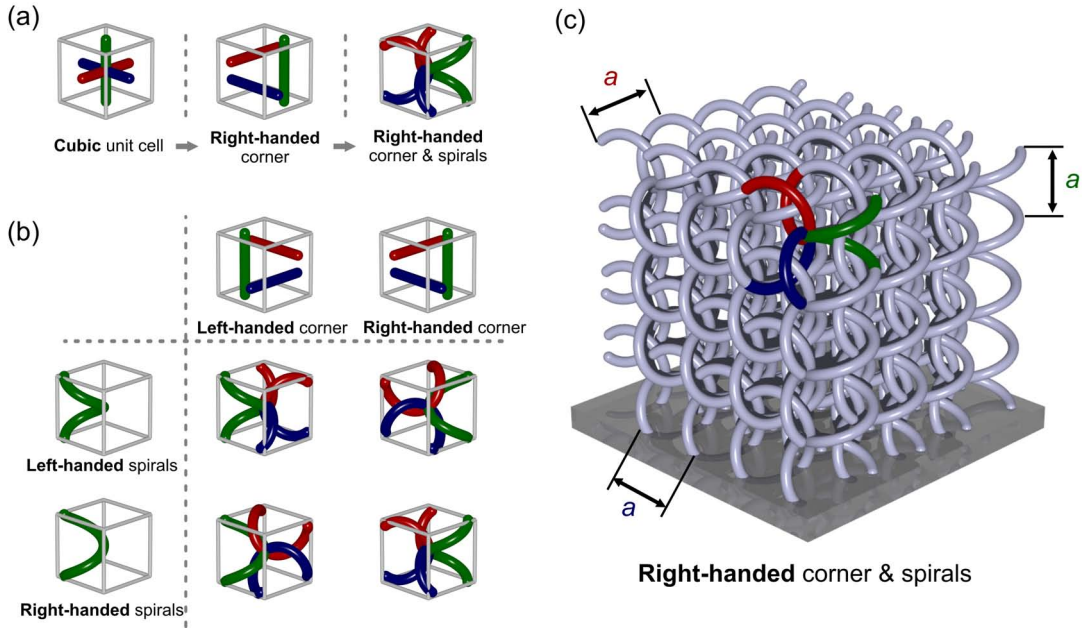


Figure 7.1: Our "bi-chiral" structures simultaneously exhibit two distinct types of chirality. The first type stems from the handedness of the circular spirals that are arranged on a simple cubic 3D lattice. (a) Displacing the central spiral axes by half the spiral diameter enforces a mechanical connection point of the three spirals in the center of the unit cell. The orientation of these three fictitious spiral axes (the "corner") introduces a second type of chirality. (b) Combined with the chirality of the spirals, four distinct types of bi-chiral photonic crystals result, namely, left/left, right/right, left/right, and right/left-handed structures. (c) Complete structure. The color coding is the same as in (a) and (b) and serves as a guide to the eye.

## Design

The construction principle of our blueprint is illustrated in Fig. 7.1. We have started from a 2D square array of left- or right-handed circular dielectric spirals, the optical properties of which have been discussed in the previous chapter. A very large resonant enhancement of the chiral properties occurs if the dielectric spiral pitch matches the pitch of the light spiral, i.e., the effective wavelength. As a result, light with the same handedness as the dielectric spirals is reflected for frequencies around the resonance, whereas light with the opposite handedness is transmitted. An obvious first extension of such a uniaxial structure is to arrange three sets of spirals along the three orthogonal directions in space (Fig. 7.1(a)). In general, however, this will not lead to mechanically connected structures, rendering the result essentially useless. By displacing the axes of the spirals by their radius as shown on the right-hand side of Fig. 7.1(a), a connection point of the three spirals in the center of each cubic cell can be enforced. After displacing two of the three axes, one is left with two non-equivalent options for positioning the third axis. This choice introduces a second type of chirality

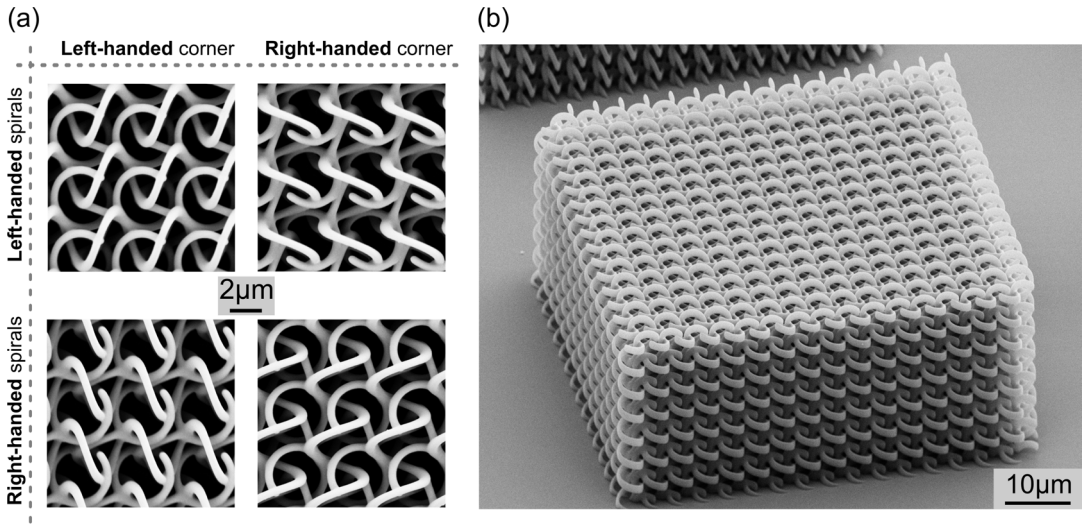


Figure 7.2: Electron microscopy images of fabricated bi-chiral photonic crystals. (a) Top views on left/left, right/left, left/right, and right/right-handed photonic crystals. (b) Oblique view on a right/left-handed polymer structure made by DLW. The cubic lattice constant of all structures is $a = 4\,\mu\text{m}$, their footprint is $60\,\mu\text{m} \times 60\,\mu\text{m}$, and they contain seven lattice constants normal to the glass substrate plane. The diameter of every spiral is $L = 0.9a$.

to the overall structure that is distinct from the chirality of the spirals. It is clear from this construction that the chiral-optical properties will be identical for propagation of light along the three cubic axes — in sharp contrast to uniaxial structures.

### Fabrication

To test our concept of bi-chiral photonic crystals, we have fabricated corresponding structures by means of DLW. A selection of electron microscopy images of fabricated structures is shown in Fig. 7.2 (further images are shown in the appendix D to demonstrate the reproducibility). Fig. 7.2(a) depicts top-view images of all four bi-chiral combinations; Fig. 7.2 shows an oblique view of a structure with right-handed corner and left-handed spirals ("right/left"). The mechanical stability and structural quality turned out to be very good which is clearly due to the fact that all three spirals of a unit cells are connected.

### Characterization

We have characterized these structures by normal-incidence optical transmittance spectroscopy using the Fourier-transform microscope-spectrometer. The experimental results are shown in the left-hand column of Fig. 7.3. For an ideal structure, we

expect that, for instance, the transmittance of a right/right-handed structure for left-handed circularly polarized incident light (LCP) is identical to that of a left/left-handed structure and right-handed circularly polarized light (RCP). Our experimental results closely follow that expectation, indicating excellent reproducibility as well as sample quality. More importantly, it becomes evident that the differences between LCP and RCP are much more pronounced for the right/right and the left/left-handed photonic-crystal structures as compared to the mixed cases, i.e., the right/left and the left/right-handed structures. The gray areas in Fig. 7.3 highlight this aspect. As pointed out in the introduction, only the mixed cases are thermodynamically stable for the blue phase of cholesteric liquid crystals found in nature. Thus, our work on artificial materials allows us to access interesting and relevant structures that are simply not available in nature.

To further support our claims, we calculate the optical properties, assuming a plane wave impinging under normal incidence. The refractive index of the polymer is taken as $n = 1.57$, that of the glass substrate as 1.52. The structure follows our above blueprint and the ellipticity of the voxels in DLW is explicitly accounted for (aspect ratio of 2.7). The volume-filling fraction is 27.6%. The theoretical results shown in the right-hand column of Fig. 7.3 agree well with the experimental values (Fig. 7.3, left-hand side). In particular, much more pronounced effects are found for the two cases where motif and corner have the same handedness as compared to the two mixed cases. The remaining small quantitative discrepancies between experiment and theory are likely due to the finite opening angle of light in the optical measurements and/or due to small structural imperfections.

### Summary

In conclusion, we have introduced, fabricated, and characterized bi-chiral dielectric photonic crystals. In these structures, one type of handedness stems from the motif (the spirals in our case) and the other one from the corner, i.e., from the fictitious skeleton onto which the motif is arranged. We have found much more pronounced chiral effects if motif and corner have the same handedness as compared to the mixed cases. In nature, only the mixed cases are realized due to thermodynamical restrictions.

Our concept of bi-chiral dielectric photonic crystals with cubic symmetry avoids the strong directional dependence[2] of previous uniaxial structures while maintaining strong circular dichroism via pronounced polarization stop bands.

[2] Our first studies on the angle dependency of finite bi-chiral photonic crystals can be found in appendix C.

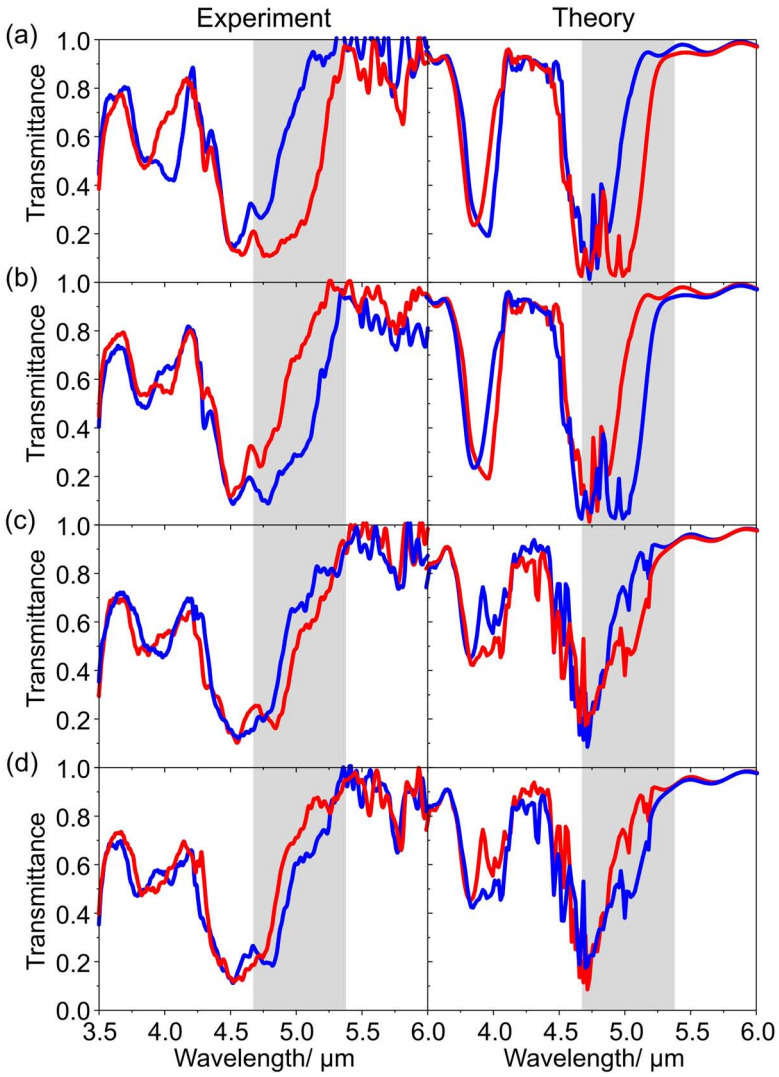


Figure 7.3: Transmittance spectra of the samples shown in Fig. 7.2 taken/calculated under normal incidence for circular polarization of the incident light. Left-handed circular polarization (blue) and right-handed circular polarization of the incident light (red) are shown for all four different bi-chiral structures. (a) Right-handed corner/right-handed spirals (right/ right), (b) left/left, (c) left/right, and (d) right/left. Note that much larger circular dichroism is observed (see highlighted gray areas) for the right/right and the left/left-handed structures compared to the mixed cases left/right and right/left.

# 8. Conclusions and outlook

Artificial photonic nanostructures enable far-reaching control of light propagation and light-matter interaction. They are classified as chiral photonic crystals if their periodically arranged building blocks possess a helical twist — either right-handed or left-handed — on approximately the scale of the wavelength of the interacting light. These two versions are mirror images of each other, so-called enantiomers. Geometrically, they cannot be brought into congruence by mere spatial rotation and translation, and optically, they promise to have a selective response to circularly polarized waves.

In this thesis, we have investigated the linear-optical properties of polymeric three-dimensional chiral photonic crystals in theory and experiment. The study of such artificial optical materials demands the ability (i) to structure dielectrics in all spatial directions on a sub-micron scale, (ii) to design blueprints for three-dimensional chiral building blocks, (iii) to numerically calculate the optical spectra, and (iv) to characterize the fabricated structures comprehensively.

To accomplish task (i), we have employed direct laser writing (DLW) allowing for the fabrication of arbitrary three-dimensional nanostructures with feature sizes smaller than 100 nm. This technique turned from a scientific curiosity into a standard for microfabrication for a variety of applications — from photonic nanostructures to scaffolds for biological systems. Broadly speaking, DLW can be considered as the 3D analogue of planar electron-beam lithography.

In the course of this thesis, we have considerably improved the DLW system technically and conceptionally. In cooperation with Carl Zeiss AG and Nanoscribe GmbH, an advanced and compact DLW system has been designed, and several experimental setups have been realized. A compact frequency-doubled erbium-doped fiber laser with sub-150 fs pulse duration is used as a robust laser source at 780 nm central wavelength replacing the more expensive Ti:sapphire laser system. The laser power is now controlled by an acousto-optical modulator and can be adjusted automatically. The laser beam is aligned to pass light-shielding cage systems and to couple into an inverted microscope, where the beam is focused tightly. A piezoelectric scanning stage provides the accuracy for the patterning of photosensitive resists with arbitrary trajectories in a volume of 300 µm×300 µm×300 µm. Another novelty is the motorized scanning stage allowing to move the sample laterally in an area of 10 cm×13 cm. All essential components are addressed by a control software.[1]

[1]The control software has been programmed by Dr. Georg von Freymann.

*The* key feature of the table-top system is the autofocus. The interface between the cover slip and the photoresist is found automatically and reproducibly leading to an unprecedented level of automatization of the DLW system.

For the experiments on chiral photonic crystals, the commercially available negative-tone photoresist *SU-8* has been found to be a good choice because of good resolution (linewidths $< 150\,\mathrm{nm}$) and high transparency from the visible to the near-infrared spectral range. Furthermore, the exposure leads to a very small change of the refractive index ($\Delta n < 10^{-3}$). Accordingly, the perturbation of the laser focus at intersection points with exposed areas is negligible.

The next step (ii) was to investigate two different blueprints composed of chiral building blocks: Chiral layer-by-layer systems (composed of parallel rods twisted along the stacking direction) and circular-spiral photonic crystals (composed of periodically arranged helices). These chiral materials may totally inhibit the propagation of *one* of the two circular polarizations in a certain frequency regime leading to a polarization filter. This *polarization stop band* can occur if the pitch of the dielectric chiral structure matches the material wavelength of light. The circular polarization with the same handedness as the structure is strongly reflected, whereas the non-matching circular polarization is transmitted. Astonishingly, in the matching case, only a few lattice constants along the propagation direction are needed to suppress the light intensity by several orders of magnitude. Moreover, excellent optical performance can even be obtained with the low refractive index of polymers.

Having these chiral blueprints at hand, we were able to design several tailored chiral photonic crystals. However, before actually fabricating these structures, we have always predicted their optical properties with numerical calculations. The established scattering-matrix approach (iii) allows for calculating transmittance and reflectance spectra of finite-size periodic nanostructures for photonics. Hence, all presented architectures have first been optimized using a scattering-matrix-approach computer program.[2]

Simulation techniques are employed for efficiency but also for comparison with the actual transmittance experiment. For that reason, we have presented the setups for spectroscopy in the near- and mid-infrared spectral range (covering wavelengths of 600–2200 nm and 2700–7000 nm, respectively). Analyzing the chiral-optical properties demands the control of the polarization of impinging light. Consequently, both setups are modified to be ready for broadband polarization-resolved spectroscopy. The characterization of the fabricated samples (iv) is completed with scanning electron micrographs of the fabricated structures.

Along these lines, we have investigated low-index-contrast three-dimensional layer-by-layer chiral photonic crystals showing giant circular dichroism from polarization stop bands centered around the telecom wavelength of 1.55 µm. The underlying physics of these polymeric crystals has been explained by an analytical model for chiral layer

[2]The original version of this software has been programmed by Dr. Stefan Linden.

systems. Each layer reflects a partial wave leading to a circularly polarized reflection with the same handedness as the crystal. As a result, if the impinging circular polarization has the same handedness as the structure, the waves will be reflected in phase and with the same handedness as the incoming wave. If the impinging circular polarization has the opposite handedness as the structure, the reflected waves will just cancel out and the light will be transmitted.

The obtained giant circular dichroism at 1.8 µm wavelength for the circular-spiral design is comparable to that of the layer-by-layer approach. The polarization stop bands observed in this second blueprint can be understood very intuitively by calculated field distributions. If the impinging circular polarization has the same handedness as the spiral structure, light is stronger confined within the dielectric structure compared to the non-matching case. This leads to a higher effective refractive index for the matching case and to a relative shift of the reflection bands occurring for both circular polarizations in the photonic crystal. Notably, the overall agreement between experiment and theory is good in both cases. In particular, the relative handedness of light and structure, the spectral position of the polarization stop band, and the depth of the transmittance minima are reproduced very well. However, although both approaches have shown excellent experimental results, we have focused on the circular-spiral building block in our search for possible applications.

One aim of the work in applied nanophotonics is to present functional devices. Our chiral photonic crystals show a high potential for future uses because they act as ultra-compact filters for circular polarization. Moreover, a chiral three-dimensional photonic crystal sandwiched between two crossed quarter-wave plates functions as a thin-film linear polarizer. Asymmetric combinations with only one quarter-wave plate on one side allow for thin-film linear polarizers or for "poor-man's" optical isolators (depending on from which side light impinges onto the device). A poor-man's chiral optical isolator is based on the change of the circular polarization upon Fresnel back-reflection from a mirror. Since the chiral photonic crystals keep their handedness (*in*dependent on from which side light impinges onto the device), the light is blocked from propagating back into, e.g., a laser source. This device is only a "poor man's" optical isolator because it will only isolate one particular circular polarization — which is in sharp contrast to isolators based on the non-reciprocal Faraday effect. The quarter-wave plates used for these experiments are one-dimensional periodic sets of lamellae, leading to form birefringence in the long-wavelength limit. Corresponding polymeric heterostructures have been fabricated by means of DLW and their functionality has been investigated with transmittance experiments.

In order to obtain deeper insight in the physics of the important circular-spiral building block, we have investigated three-dimensional photonic superlattices composed of polymeric spirals in various spatial checkerboard-like arrangements. Surprisingly, depending on the relative phase shift and handedness of the chiral building blocks, different dichroitic resonances appear or are suppressed. We have carried out corresponding experiments and have found that the chiral-optical properties strongly

depend on the in-plane arrangement of the spirals rather than solely on the spiral parameters. This discloses new design options for tailoring the optical properties of artificial chiral structures. Furthermore, this observation highlights the differences in the physics of cholesteric liquid crystals and helical photonic crystals. Moreover, the question arose whether we could find further interesting arrangements of the spirals.

So far, all discussed designs of chiral photonic crystals have uniaxial symmetry, i.e., *one* helical axis. To overcome this drawback we have proposed a new class of crystals: Bi-chiral photonic crystals. They are tailored man-made solids inspired by "blue-phase" cholesteric liquid crystals and possess two types of chirality leading to four different types of bi-chiral structures. One type of handedness stems from the motif (the spirals in our case) and the other one from the corner, i.e., from the fictitious skeleton onto which the motif is arranged. Our concept of bi-chiral dielectric photonic crystals with cubic symmetry avoids the strong directional dependence of previous uniaxial structures while maintaining strong circular dichroism via pronounced polarization stop bands. We have experimentally realized all four bi-chiral combinations. Notably, in naturally occurring blue-phase liquid crystals, only two of these are thermodynamically stable. Interestingly, we have found that the combinations not occurring in nature show the stronger circular dichroism.

In conclusion, we have investigated an exciting subclass of photonic nanostructures: Chiral three-dimensional photonic crystals. We have fabricated several high-quality structures by using DLW and have characterized them by transmission experiments and numerical calculations. This material class shows a high potential for applications because of their intense response to circularly polarized light.

The route for future research might lead to high-index-contrast chiral nanostructures. For example, we still have to answer the question if bi-chiral photonic crystals replicated in silicon can possess a complete photonic band gap for *one* of the circular polarizations. A complete polarization band gap could be an amazing extension to the original proposals [11, 12, 50]. Furthermore, artificial chiral metamaterials composed of subwavelength metallic building blocks are investigated by many research groups [44, 79] and show qualitative new effects due to their chirality, e.g., negative phase velocities at microwave frequencies [64, 65]. Observing these novel effects in the optical regime is one major task, but magneto- or nonlinear-optical effects of chiral materials might also bring surprises in the future.

The above notions assure that artificial chiral materials will continue to be an active and exciting research field of optics and photonics. We are looking forward to find even stronger effects in future chiral optical materials, new physics in chiral photonic crystals or metamaterials, and, possibly, innovative real-world applications for chiral nanostructures.

# A. Chiral twist defect in layer-by-layer photonic crystals

In this appendix, we study defective layer-by-layer chiral photonic crystals. Introducing a planar chiral twist defect creates a single circularly polarized localized mode. The narrow defect mode results in a peak in transmission for a circularly polarized wave with the same handedness as the structure. Our design is simple and robust leading to a quality factor $Q$ as high as 700 for low-index-contrast twisted woodpiles. We note that such defects have also been proposed and studied in cholesteric liquid crystals and chiral sculptured thin-films [42, 132].

## Design

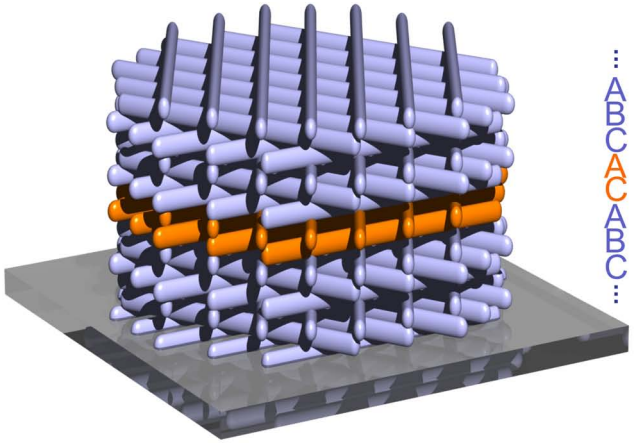


Figure A.1: Design of defective layer-by-layer chiral photonic crystal. The geometrical parameters of the twisted woodpile are the same as in chapter 6.1, but we stack 16 pitches and introduce a defective "AC" layer between pitch 8 and 10.

The defective chiral photonic crystal to be characterized is shown in Fig. A.1. We picked out one example of several possible designs to introduce defects based on stacking errors in layer-by-layer structures. Here, we study a twisted woodpile with $N = 3$, i.e., subsequent layers are twisted by 120° leading to a "ABC" sequence. The idea is to sandwich an "AC" defect layer in the middle of 16 unperturbed pitches. In the next section, we study how strong the influences on the intense circular reflection from the polarization stop band are.

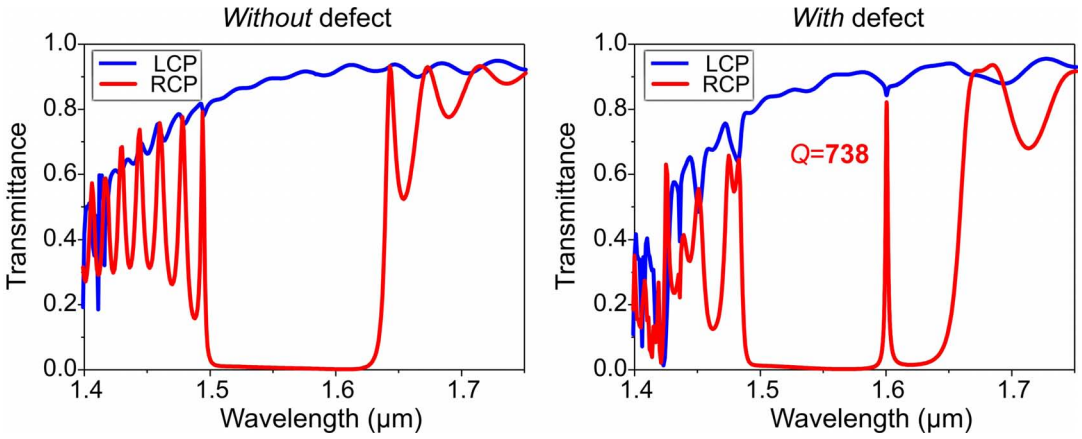


Figure A.2: Calculated transmittance spectra corresponding to the structure depicted in Fig. A.1. The geometrical parameters are the same as in chapter 6.1, but with 16 pitches.

## Characterization

Corresponding scattering-matrix calculations of the structure shown in Fig. A.1 and a reference structure without defect are depicted in Fig. A.2. Pronounced polarization stop bands centered around 1.55 μm wavelength are observed for both structures (geometrical parameters as in chapter 6.1, but with 16 pitches). However, for the defective layer-by-layer structure, a chiral defect mode pops up at about 1.6 μm wavelength. We calculate the quality factor of this resonance to be $Q = 1600.53\,\text{nm} / 2.17\,\text{nm} = 738$ for an assumed polymeric refractive index of $n = 1.57$. The transmittance of right circular polarization at the center-frequency of the defect reaches a value of more than 80%. The transmittance of left-circularly polarized light is hardly affected.

For this configuration, we also perform calculations for oblique incidence (0°–15°) on the structures (shown in Fig. A.3). The gray-scale plots of the calculated transmission versus angle of incidence and wavelength are shown for the twisted-woodpile structure with and without defect, respectively. The dotted ellipse on the right-hand-side graph mark the spectral features associated with the planar "AC" defect. As expected for layer-by-layer structures with planar defects, the position of the defect mode depends on the angle of incidence. The defect mode disappears for an angle of about 10°.

With a different choice of the phase defect, the optical properties of defective layer-by-layer chiral photonic crystals change dramatically — up to a point where RCP does not couple to the defect anymore; instead, LCP is suppressed within the polarization stop band.

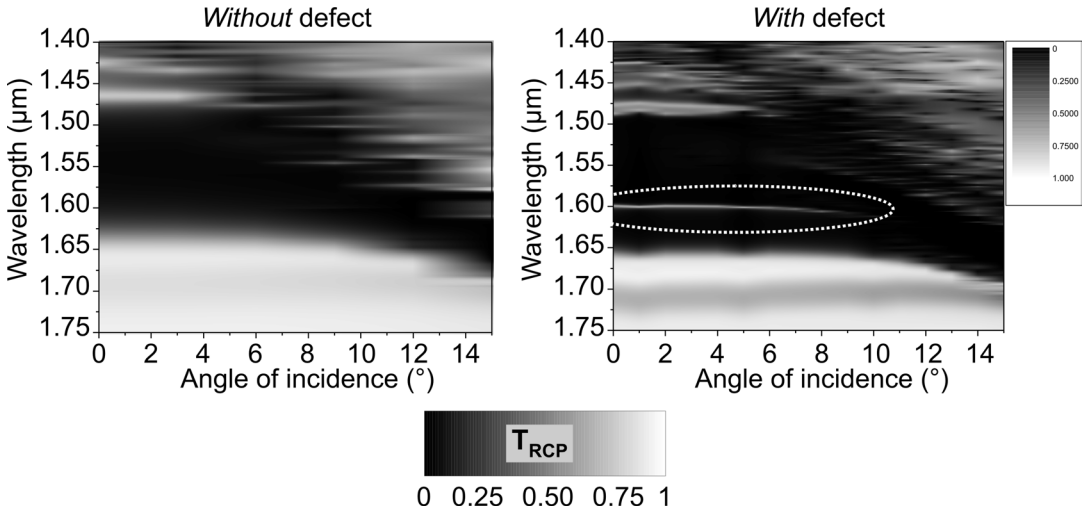


Figure A.3: Gray-scale plots of the calculated transmission versus angle of incidence and wavelength shown for the twisted-woodpile structure with and without defect, respectively. The black regions centered about 1.55 μm correspond to the polarization stop bands. The dotted ellipse on the right-hand-side graph mark the spectral feature associated with the planar "AC" defect.

## Summary

In summary, we have performed scattering-matrix calculations for a specific design of defective layer-by-layer chiral photonic crystals. Introducing a planar chiral twist defect creates a single circularly polarized localized mode. For polymeric twisted woodpile, we have calculated a $Q$ factor of 738 for only 16 pitches. Theory even predicts $Q$ factors of more than 30,000 for other cases with low anisotropy [132]. The influence of the angle of incidence on the spectral position of the defect mode has also been investigated.[1] These localized modes may serve as low threshold lasers, low loss waveguides, and narrow band filters [42].

[1] A more comprehensive study of twist defects can be found in reference [42].

# B. Supplementary data of chiral circular-spiral photonic crystals

In this section, additional information about chiral circular-spiral photonic crystals is given (see also reference [128]).

At first, we calculate the minimum transmittance of right circular light within the polarization stop band under strict normal incidence on a right-handed spiral with $N$ pitches. In Fig. B.1, this value is plotted over the number of pitches $N$. As expected, right circular light decreases exponentially within the polarization stop band.

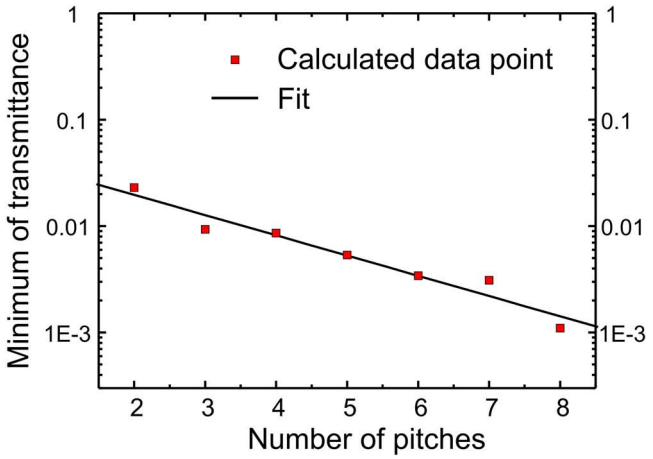


Figure B.1: Logarithmic plot of the calculated minimum transmittance of right circular light in the polarization-stop-band region for a right-handed spiral structure under strict normal incidence and in dependency of the number of axial lattice constants. As expected, right circular light decreases exponential within the polarization stop band.

Next, we want to present some control measurements that served as sanity tests. Fig. B.1 depicts measured transmittance spectra of the sample characterized in chapter 6.2. To check the reciprocal behavior, the influence of the substrate, and of the stabilizing grid, we perform two measurements: In the first take, light impinges on the surface of the photonic crystal. In the second take, we turn the sample by 180° while leaving the measurement setup as is (compare Figs. B.1(a) and (b)). Obviously,

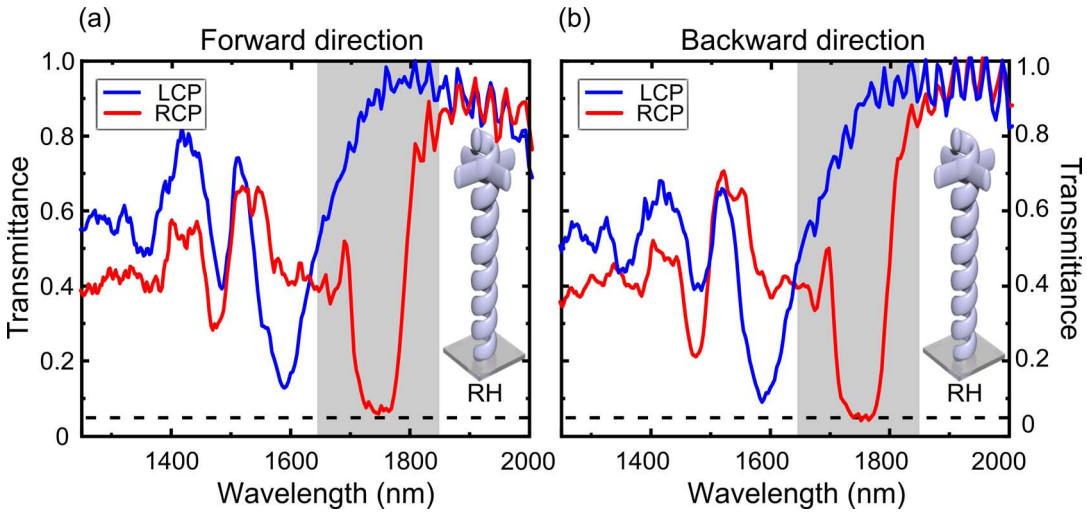


Figure B.2: (a) Measured transmittance spectra of the sample characterized in chapter 6.2, but taken on a different day. (b) We checked the reciprocal behavior, the influence of the substrate, and of the stabilizing grid by turning the sample by 180° while leaving the measurement setup as is.

these influences are very small since the measurements reveal nearly identical spectra. Moreover, the transmission is reciprocal (i.e., the colors do not interchange; as expected).

Furthermore, we measure transmittance spectra of the same sample as in Fig. B.2(a), but with an additional quarter-wave plate and analyzer (shown in Fig. B.3(a)). This allows for measuring the polarization conversion of the sample that has been found to be very low in the polarization-stop-band region — even in the experiment with a finite opening angle. Note that we have referenced the cross terms on the glass substrate and with non-crossed polarizer and analyzer. The small conversion at the lower-wavelength side of the polarization stop band is not yet understood.

Finally, we show angle-resolved transmittance difference measurements of the same sample in Fig. B.3(b). We plot $T_{RCP}$-$T_{LCP}$ which is the difference of the transmittance measured by using circular polarization. We choose an angle of incidence of 0°, 5°, 10°, and 15° and reference on the glass substrate. Surprisingly, for an angle of 15°, we still have a transmittance difference of 60%. However, we observe a shift of the center wavelength of the polarization to higher wavelengths.

### Summary/Next steps

We have performed additional calculations/experiments on circular-spiral photonic crystals. The exponential decay within the polarization stop band is affirmed theoret-

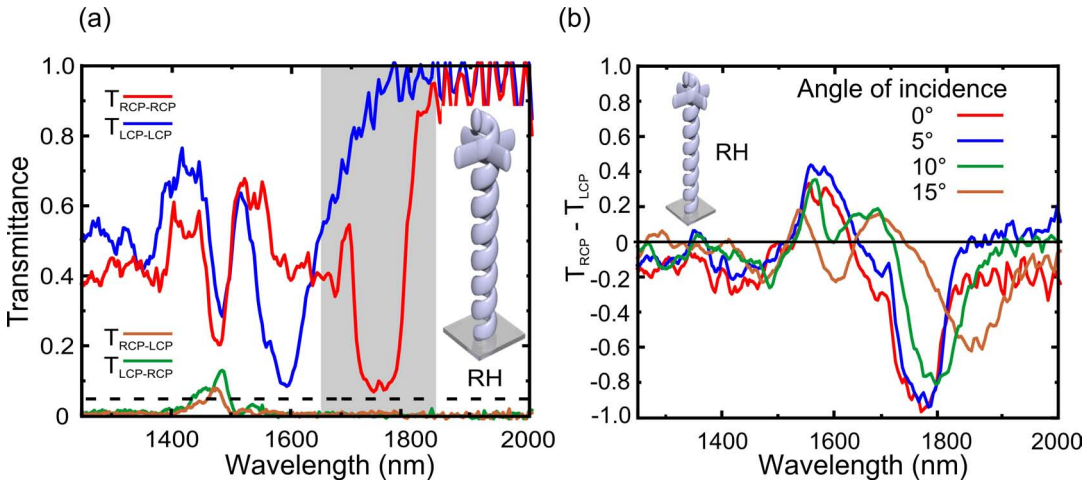


Figure B.3: (a) Measured transmittance spectra of the same sample as in Fig. B.2(a), but with an additional quarter-wave plate and analyzer. $T_{RCP-RCP}$ corresponds to the transmittance of RCP when RCP is incident, $T_{LCP-LCP}$ to the transmittance of LCP when LCP is incident, $T_{RCP-LCP}$ to the transmittance of RCP when LCP is incident, and $T_{LCP-RCP}$ to the transmittance of LCP when RCP is incident. (b) Angle-resolved transmittance difference measurements of the same sample as in Fig. B.2(a). Accordingly, $T_{RCP}$-$T_{LCP}$ denotes the difference of the transmittance measured with circular polarization.

ically. Sanity measurements on spirals have proven the reciprocal behavior and ruled out a strong influence of the stabilization grid and the substrate.

Angle-resolved transmittance measurements give insight in the optical properties of the spirals that are not axial excited. This last experiment has been the motivation to achieve more isotropy of the optical properties by using bi-chiral photonic crystals (see chapter 7 and also the next appendix C).

# C. First studies of angle dependence of bi-chiral photonic crystals

From our discussion in chapter 6, it is clear that a single spiral will show strong circular dichroism for light propagating along the spiral's axis. Nevertheless, a true chiral object shows chirality regardless from which direction it is looked at. Hence, a right-handed spiral should interact differently with left- or right-circularly polarized light even under propagation perpendicular to its obvious axis. This behavior is demonstrated in the numerical calculations shown in Fig. C.1.

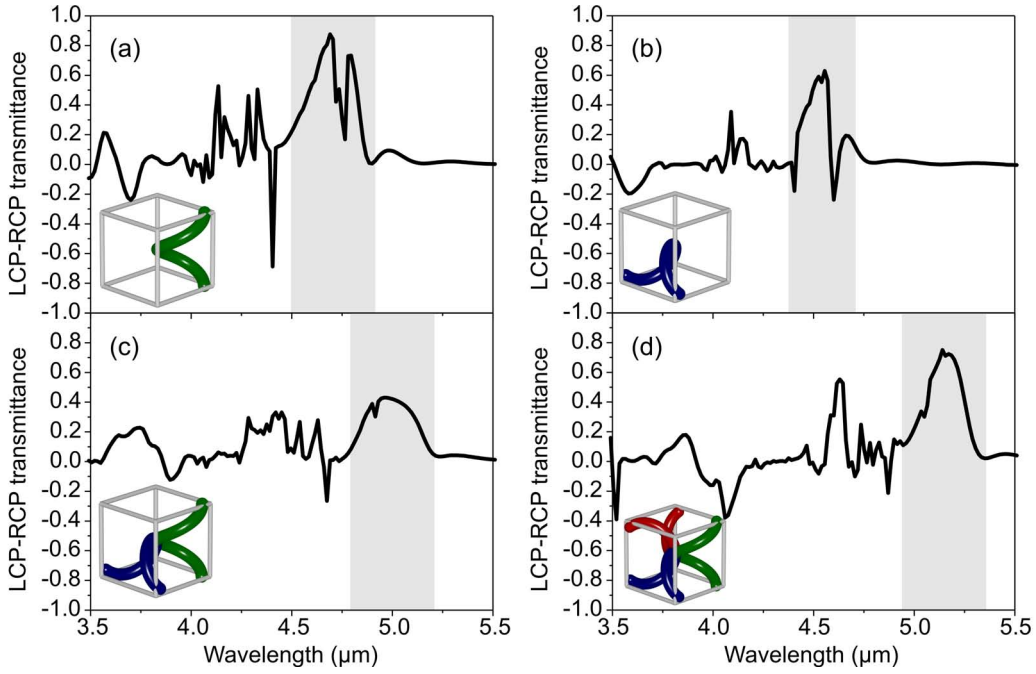


Figure C.1: Numerical calculations: "LCP-RCP" transmittance of structures, which are eight unit cells high and infinitely extended in the $xy$-plane. The corresponding unit cell is shown as an inset in (a)–(d). Geometrical parameters are the same as in chapter 7.

Here, we plot the difference in transmittance between left- and right-circular polarized light (LCP and RCP, respectively). A difference "LCP-RCP" of +1 in this plot means that only LCP light is transmitted, zero corresponds to equal transmittance of LCP

and RCP light and -1 difference indicates 100% transmittance of the RCP light and 0% for LCP. The insets in all parts of the Figs. display the configuration under study; the light is impinging along the $z$-axis. In Fig. C.1(a), the usual case of axial excited circular spirals is shown. We find a polarization stop band around 4.75 µm wavelength — RCP light is reflected back from the right-handed spiral and LCP light is mainly transmitted. The parameters of each spiral are as follows: Elliptical cross-section as in the experiment, a lattice constant and pitch of 4 µm, a spiral diameter of $L = 0.9a$ and the index of refraction of SU-8 ($n = 1.57$).

If we now calculate the response for the same spiral under perpendicular incidence towards its axis, we will still keep strong circular dichroism, although slightly shifted to shorter wavelengths (see Fig. C.1(b)). Here, neither the "matching" nor the "non-matching" circular polarization can actually follow the spiral, nevertheless, the electric field of RCP light is still more confined to the dielectric structure, resulting in the observed circular dichroism. Combining two spirals as shown in Fig. C.1(c) increases the overall filling fraction of the structure and, hence, the effective refractive index. As a result, the polarization stop band shifts towards longer wavelengths. The final combination of all three spirals finally results into a very pronounced stop band around 5.1 µm wavelength (see Fig. C.1(d)). This computed behavior is also found experimentally in chapter 7. So far, the behavior under perpendicular incidence does not look too different from that of the uniaxial structures. However, the bi-chiral photonic crystal should provide a certain isotropy regarding its chiral properties as this structure shows essentially the same optical properties along each of the three principal axes.

To test this hypothesis, we have calculated angle-resolved transmittance spectra for a bi-chiral photonic crystal made from silicon. LCP (RCP) light is impinging under an oblique angle $\theta$ with respect to the $z$-axis and the azimuthal angle is rotated from 0° to 360°. The resulting LCP-RCP transmittance for $\theta = 0°$, $\theta = 35.7°$, and $\theta = 45°$ is shown in Fig. C.2. White (cyan) areas correspond to high transmittance of LCP (RCP) light. At around 2.5 µm wavelength an almost flat polarization stop band can be observed, hinting that we might have achieved a complete polarization gap — a frequency region without photonic states for all crystal directions and only for one of the two circular polarizations. However, the results seem to be not as isotropic as expected, due to the inherent difficulty to keep the conditions for the impinging light exactly equal for all angle of incidence. We calculate the optical response for a finite structure with real surfaces. Light impinging under an angle will be refracted at the photonic crystal interface. At this point, its polarization state generally changes.

### Summary

We cannot necessarily conclude that the dispersion observed in the numerical calculation is connected with real anisotropy or isotropy. It might also stem from the different coupling of the incoming light to the modes of the photonic crystals. There-

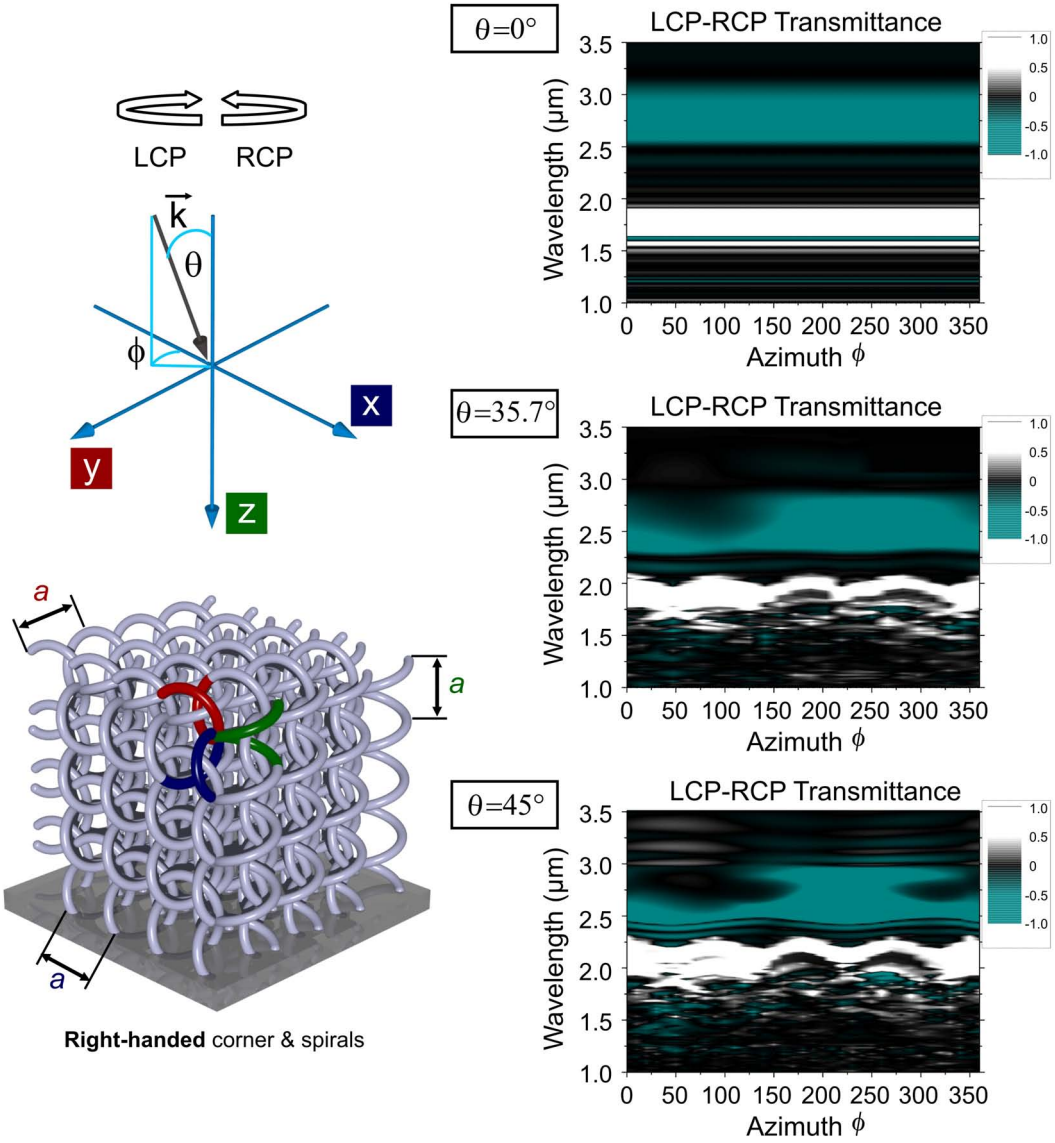


Figure C.2: Angular-resolved calculated LCP-RCP transmittance spectra of a silicon right/right bi-chiral photonic crystal. White (cyan) areas correspond to high transmittance of LCP (RCP) light. Light is impinging under 0°, 35.7°, and 45° of incidence with respect to the surface normal. Geometrical parameters: Lattice constant $a = 1\,\mu\text{m}$, linewidth $w = 0.14\text{a}$, line aspect ratio $\chi$=1, spiral diameter $L = 0.9a$, 8 periods in $z$-direction, and index of refraction $n = 3.5$.

fore, results are preliminary studies and have to be taken with a grain of salt. In the future, band structure calculations accounting for the polarization state might answer our hypothesis.

# D. Reproducibility of the fabricated samples

In chapters 6 and 7, we have shown selected spectra and scanning electron micrographs for all the results. In this appendix, evidence is given that our fabricated samples are indeed reproducible.

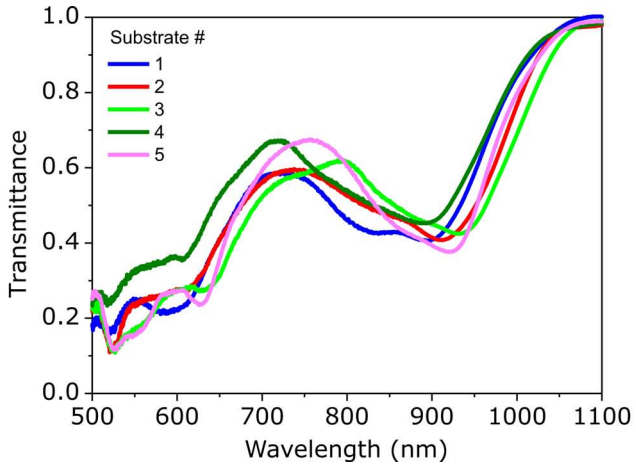


Figure D.1: (a) Measured transmittance spectra of five woodpiles ($a = 600\,\text{nm}$) written with the same nominal parameters but on different substrates.

Firstly, we present five measured spectra of woodpiles in a face-centered-cubic (fcc) geometry and a lateral lattice constant $a = 600\,\text{nm}$ depicted in Fig. D.1. A woodpile is a structure of considerable complexity and demands highest accuracy of the fabrication process. The presented spectra provide insight in the reproducibility because they are written with the same settings and in the same resist but on different substrates. The different substrates have been addressed automatically and have been developed instantaneously. The measured stop bands at about 920 nm match very well for all templates taking highest demands on the fabrication process into account. In particular, the shapes and spectral positions are well reproduced.

Secondly, measured spectra of woodpiles in an fcc geometry and a lateral lattice constant $a = 600\,\text{nm}$ are shown, written on the same substrate with an energy dose variation. As presented in Fig. D.2, the stop band of the woodpile moves spectrally to smaller wavelengths with decreasing deposited energy. This is because of the smaller effective refractive index resulting from smaller filling fractions, i.e., we are able to

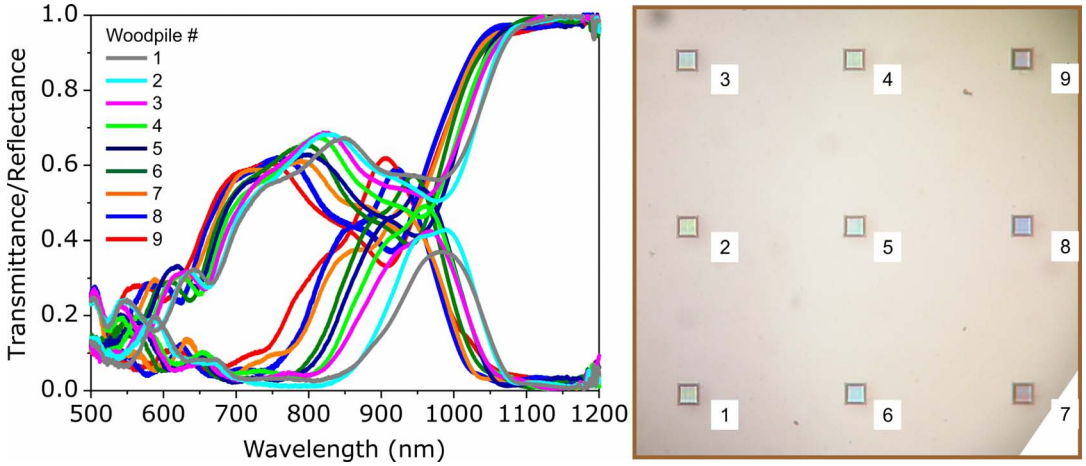


Figure D.2: (a) Measured transmittance/reflectance spectra of 600 nm woodpiles written with the same geometrical parameters on the same substrates. The power decreases from #1 (highest power to #9(lowest power). (b) Light microscope graph of the measured woodpiles. The numbers correspond to the legend of (a). Higher numbers mean lower energy.

smoothly vary the filling fraction of the woodpile — even for structures with these small dimensions and feature sizes.

Finally, scanning electron micrographs of the most complex structures of this thesis are presented: Bi-chiral photonic crystals. In Fig. D.3, we give an overview of the fabricated sample characterized in chapter 7. Of course, all possible combinations of bi-chiral photonic crystals have been written on one substrate. Moreover, we have written several of these sets in a row of several millimeters. Obviously, the quality of all structures is equally good. The interface finder worked well securing the same height for each structure.

### Summary

In summary, we want to stress the fact that results have been reproduced for *each* presented chiral design. In this appendix, we have given *exemplary* experimental data of (i) woodpiles with very small lattice constants and (ii) the most complicated chiral structures of this thesis, both of which are extremely demanding in terms of accuracy and stability of the fabrication process and could be reproduced very well.

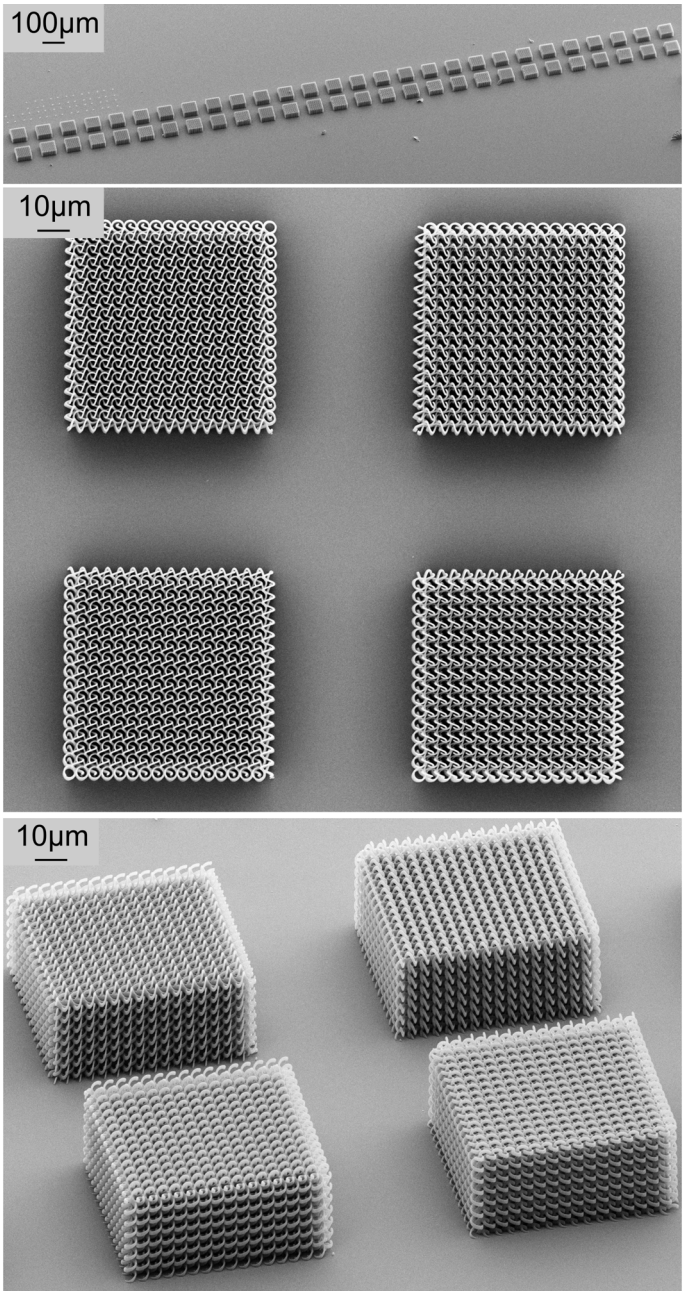


Figure D.3: Overview of the fabricated sample characterized in chapter 7.

# Bibliography


[1] D. B. Brewster, "*On the laws which regulate the polarization of light by reflection from transparent bodies*," Philos. Trans. R. Soc. Lond. **105**, 125 (1815).

[2] W. K. von Haidinger, "*Über das direkte Erkennen des polarisierten Lichts*," Pogg. Ann. **63**, 29 (1844).

[3] N. W. Roberts, T.-H. Chiou, N. J. Marshall, and C. T. W., "*A biological quarter-wave retarder with excellent achromaticity in the visible wavelength region*," Nature Photon. **3**, 641 (2009).

[4] J. Hwang, M. H. Song, B. Park, S. Nishimura, T. Toyooka, J. W. Wu, Y. Takanishi, K. Ishikawa, and H. Takezoe, "*Electro-tunable optical diode based on photonic bandgap liquid-crystal heterojunctions*," Nature Mater. **4**, 383 (2005).

[5] A. R. Parker and H. E. Townley, "*Biomimetics of photonic nanostructures*," Nature Nanotech. **2**, 347 (2007).

[6] L. Kelvin, "*Baltimore Lectures on Molecular Dynamics and the Wave Theory of Light*," Clay & Sons (1904).

[7] I. Kant, "*Prolegomena zu einer jeden künftigen Metaphysik, die als Wissenschaft wird auftreten können*," Johann Friedrich Hartknoch **4**, 52 (1783).

[8] L. Pasteur, "*Mémoire sur la relation qui peut exister entre la forme cristalline et la composition chimique, et sur la cause de la polarisation rotatoire*," Comp. Rend. Paris **26**, 535 (1848).

[9] J. C. Bose, "*On the Rotation of Plane of Polarisation of Electric Waves by a Twisted Structure*," Proc. Phys. Soc. London **63**, 146 (1898).

[10] M. Wegener and N. I. Zheludev, "*Artificial chiral materials*," J. Opt. A **11**, 070201 (2009).

[11] E. Yablonovitch, "*Inhibited Spontaneous Emission In Solid-state Physics and Electronics*," Phys. Rev. Lett. **58**, 2059 (1987).

[12] S. John, "*Strong Localization of Photons In Certain Disordered Dielectric Superlattices*," Phys. Rev. Lett. **58**, 2486 (1987).

[13] A. Chutinan and S. John, "*3+1 dimensional integrated optics with localized light in a photonic band gap*," Opt. Express **14**, 1266 (2006).

[14] O. Toader and S. John, "*Proposed square spiral microfabrication architecture for large three-dimensional photonic band gap crystals*," Science **292**, 1133 (2001).

[15] S. R. Kennedy, M. J. Brett, O. Toader, and S. John, "*Fabrication of tetragonal square spiral photonic crystals*," Nano Lett. **2**, 59 (2002).

[16] Y. K. Pang, J. C. W. Lee, H. F. Lee, W. Y. Tam, C. T. Chan, and P. Sheng, "*Chiral microstructures (spirals) fabrication by holographic lithography*," Opt. Express **13**, 7615 (2005).

[17] K. K. Seet, V. Mizeikis, S. Matsuo, S. Juodkazis, and H. Misawa, "*Three-dimensional spiral-architecture photonic crystals obtained by direct laser writing*," Adv. Mater. **17**, 541 (2005).

[18] J. C. W. Lee and C. T. Chan, "*Polarization gaps in spiral photonic crystals*," Opt. Express **13**, 8083 (2005).

[19] M. Thiel, M. Decker, M. Deubel, M. Wegener, S. Linden, and G. von Freymann, "*Polarization stop bands in chiral polymeric three-dimensional photonic crystals*," Adv. Mater. **19**, 207 (2007).

[20] M. Thiel, M. Hermatschweiler, M. Wegener, and G. von Freymann, "*Thin-film polarizer based on a one-dimensional-three-dimensional-one-dimensional photonic crystal heterostructure*," Appl. Phys. Lett. **91**, 123515 (2007).

[21] F. Zhang, J. Xu, A. Lakhtakia, T. Zhu, S. M. Pursel, and M. W. Horn, "*Circular polarization emission from an external cavity diode laser*," Appl. Phys. Lett. **92**, 111109 (2008).

[22] A. Lakhtakia, "*Sculptured thin films: accomplishments and emerging uses*," Mater. Sci. Eng. C **19**, 427 (2002).

[23] Wikipedia, http://en.wikipedia.org/wiki/Chirality (2009).

[24] L. D. Barron, "*On the definition of chirality*," Chem. Eur. J. **2**, 743 (1996).

[25] D. Avnir, O. Katzenelson, and H. Z. Hel-Or, "*On the definition of chirality - Reply*," Chem. Eur. J. **2**, 744 (1996).

[26] L. D. Barron, "*Compliments from Lord Kelvin*," Nature **446**, 505 (2007).

[27] Y. Helor, S. Peleg, and D. Avnir, "*Two-Dimensional Rotational Dynamic Chirality and a Chirality Scale*," Langmuir **6**, 1691 (1990).

[28] C. Z. Liang and K. Mislow, "*Classification of Topologically Chiral Molecules*," J. Math. Chem. **15**, 245 (1994).

[29] S. F. Mason, "*Origins of Biomolecular Handedness*," Nature **311**, 19 (1984).

[30] G. Ecker, "*Chiral perturbation theory*," Prog. Part. Nucl. Phys. **35**, 1 (1995).

[31] A. Findlater, "*Chambers's Encyclopedia*," Lippincott Company (1875).

[32] P. Cintas, "*Tracing the origins and evolution of chirality and handedness in chemical language*," Angew. Chem. Int. Ed. **46**, 4016 (2007).

[33] D. F. Arago, "*Sur une modification remarquable qu'étprouvent les rayons lumineux dans leur passage a travers certains corps diaphanes, et sur quelques autres nouveaux phenomenes d'optique*," Mém. Inst. France **1**, 93 (1811).

[34] J. Biot, "*Phénomènes de polarisation successive, observés dans des fluides homogènes*," Bull. Soc. Philomath. **1**, 190 (1815).

[35] M. Faraday, "*On the magnetization of light and the illumination of magnetic lines of force*," Philos. Trans. **136**, 1 (1846).

[36] L. D. Barron, "*Chirality, magnetism and light*," Nature **405**, 895 (2000).

[37] J. A. Le Bel, "*Sur le relation qui existant entre les formules atomiques des corps organiques, et le pouvoir rotatoire de leurs dissolutions*," Bull. Soc. Chim. Fr. **22**, 337 (1874).

[38] J. van't Hoff, "*Sur les formules de structure dans l'espace*," Arch. Neerd. Sci. Exact. Nat. **9**, 445 (1874).

[39] F. Reinitzer, "*Beiträge zur Kenntniss des Cholesterins*," Monatsh. Chem. **9**, 421 (1888).

[40] J. K. Gansel, M. Thiel, M. S. Rill, M. Decker, K. Bade, V. Saile, G. von Freymann, S. Linden, and M. Wegener, "*Gold Helix Photonic Metamaterial as Broadband Circular Polarizer*," Science **325**, 1513 (2009).

[41] A. Chutinan and S. Noda, "*Spiral three-dimensional photonic-band-gap structure*," Phys. Rev. B **57**, R2006 (1998).

[42] V. I. Kopp, Z. Q. Zhang, and A. Z. Genack, "*Lasing in chiral photonic structures*," Prog. Quantum Electron. **27**, 369 (2003).

[43] A. Chutinan and S. John, "*Diffractionless flow of light in two- and three-dimensional photonic band gap heterostructures: Theory, design rules, and simulations*," Phys. Rev. E **71**, 026605 (2005).

[44] J. B. Pendry, "*A chiral route to negative refraction*," Science **306**, 1353 (2004).

[45] E. Malus, "*Sur une propriété de la lumière réfléchie par les corps diaphanes*," Nouveau Bulletin des Sciences par la Société Philomatique **1**, 266 (1809).

[46] E. Hecht, "*Optik*," Oldenbourg (2001).

[47] W. Kaminsky, "*Beiträge zur Untersuchung chiraler Eigenschaften von Kristallen*," Habilitationsschrift (Universität Köln) (1997).

[48] B. E. A. Saleh and M. C. Teich, "*Fundamentals of Photonics*," John Wiley & Sons (2007).

[49] J. Weiner and P.-T. Ho, "*Light-Matter Interaction*," Wiley-VCH Verlag GmbH (2003).

[50] K. Busch, G. von Freymann, S. Linden, S. F. Mingaleev, L. Tkeshelashvili, and M. Wegener, "*Periodic nanostructures for photonics*," Phys. Rep. **444**, 101 (2007).

[51] K. Sakoda, "*Optical Properties of Photonic Crystals*," Springer-Verlag (2001).

[52] J. D. Joannopoulos, S. G. Johnson, J. N. Winn, and R. D. Meade, "*Photonic Crystals*," Princeton University Press (2008).

[53] L. Rayleigh, "*On the maintenance of vibrations by forces of double frequency, and on the propagation of waves through a medium endowed with a periodic structure*," Philos. Mag. **24**, 145 (1887).

[54] O. Toader and S. John, "*Proposed square spiral microfabrication architecture for large three-dimensional photonic band gap crystals*," Science **292**, 1133 (2001).

[55] K. M. Ho, C. T. Chan, C. M. Soukoulis, R. Biswas, and M. Sigalas, "*Photonic band gaps in three dimensions: New layer-by-layer periodic structures*," Solid State Commun. **89**, 413 (1994).

[56] M. Deubel, M. Wegener, S. Linden, G. von Freymann, and S. John, "*3D-2D-3D photonic crystal heterostructures fabricated by direct laser writing*," Opt. Lett. **31**, 805 (2006).

[57] S. G. Johnson and J. D. Joannopoulos, "*Block-iterative frequency-domain methods for Maxwell's equations in a planewave basis*," Opt. Express **8**, 173 (2001).

[58] A. Mekis, J. C. Chen, I. Kurland, S. Fan, P. R. Villeneuve, and J. D. Joannopoulos, "*High Transmission through Sharp Bends in Photonic Crystal Waveguides*," Phys. Rev. Lett. **77**, 3787 (1996).

[59] M. Karl, S. Li, T. Passow, W. Löffler, H. Kalt, and M. Hetterich, "*Localized and delocalized modes in coupled optical micropillar cavities*," Opt. Express **15**, 8191 (2007).

[60] B. S. Song, S. Noda, T. Asano, and Y. Akahane, "*Ultra-high-Q photonic double-heterostructure nanocavity*," Nature Mater. **4**, 207 (2005).

[61] M. Deubel, "*Three-Dimensional Photonic Crystals via Direct Laser Writing: Fabrication and Characterization*," Doctoral thesis (Universität Karlsruhe) (2006).

[62] N. Tétreault, G. von Freymann, M. Deubel, M. Hermatschweiler, F. Perez-Willard, S. John, M. Wegener, and G. A. Ozin, "*New route to three-dimensional photonic bandgap materials: Silicon double inversion of polymer templates*," Adv. Mater. **18**, 457 (2006).

[63] P. Vukusic and J. R. Sambles, "*Photonic structures in biology*," Nature **424**, 852 (2003).

[64] S. Zhang, Y. S. Park, J. S. Li, X. C. Lu, W. L. Zhang, and X. Zhang, "*Negative Refractive Index in Chiral Metamaterials*," Phys. Rev. Lett. **102**, 023901 (2009).

[65] E. Plum, J. Zhou, J. Dong, V. A. Fedotov, T. Koschny, C. M. Soukoulis, and N. I. Zheludev, "*Metamaterial with negative index due to chirality*," Phys. Rev. B **79**, 035407 (2009).

[66] R. Hooke, "*Micrographia: Or Some Physiological Descriptions Of Minute Bodies Made By Magnifying Glasses With Observations And Inquiries Thereupon*," J. Martyn and J. Allestry (1665).

[67] A. C. Neville, "*Molecular and Mechanical Aspects of Helicoid Development In Plant-cell Walls*," Bioessays **3**, 4 (1985).

[68] A. R. Parker, "*515 million years of structural colour*," J. Opt. A **2**, 15 (2000).

[69] A. E. Seago, P. Brady, J. P. Vigneron, and T. D. Schultz, "*Gold bugs and beyond: a review of iridescence and structural colour mechanisms in beetles (Coleoptera)*," J. R. Soc. Interface **6**, 165 (2009).

[70] J. W. Galusha, M. R. Jorgensen, and M. H. Bartl, "*Diamond-Structured Titania Photonic-Bandgap Crystals from Biological Templates*," Adv. Mater., published online (2009).

[71] V. Sharma, M. Crne, J. O. Park, and M. Srinivasarao, "*Structural Origin of Circularly Polarized Iridescence in Jeweled Beetles*," Science **325**, 449 (2009).

[72] D. W. Lee, "*Ultrastructural Basis and Function of Iridescent Blue Color of Fruits In Elaeocarpus*," Nature **349**, 260 (1991).

[73] S. Caveney, "*Cuticle Reflectivity and Optical Activity In Scarab Beetles - Role of Uric Acid*," Proc. R. Soc. London, Ser. B **178**, 205 (1971).

[74] P. G. de Gennes and J. Prost, "*The Physics Of Liquid-Crystals*," Oxford Science Publications (1995).

[75] W. Y. Cao, A. Munoz, P. Palffy-Muhoray, and B. Taheri, "*Lasing in a three-dimensional photonic crystal of the liquid crystal blue phase II*," Nature Mater. **1**, 111 (2002).

[76] S. Meiboom, J. P. Sethna, P. W. Anderson, and W. F. Brinkman, "*Theory Of The Blue Phase Of Cholesteric Liquid-Crystals*," Phys. Rev. Lett. **46**, 1216 (1981).

[77] H. Kikuchi, M. Yokota, Y. Hisakado, H. Yang, and T. Kajiyama, "*Polymer-stabilized liquid crystal blue phases*," Nature Mater. **1**, 64 (2002).

[78] H. J. Coles and M. N. Pivnenko, "*Liquid crystal 'blue phases' with a wide temperature range*," Nature **436**, 997 (2005).

[79] V. M. Shalaev, "*Optical negative-index metamaterials*," Nature Photon. **1**, 41 (2007).

[80] L. R. Arnaut, "*Chirality in multi-dimensional space with application to electromagnetic characterisation of multi-dimensional chiral and semi-chiral media*," J. Electromagnet Waves **11**, 1459 (1997).

[81] A. S. Schwanecke, A. Krasavin, D. M. Bagnall, A. Potts, A. V. Zayats, and N. I. Zheludev, "*Broken time reversal of light interaction with planar chiral nanostructures*," Phys. Rev. Lett. **91**, 27404-1 (2003).

[82] R. J. Potton, "*Reciprocity in optics*," Rep. Prog. Phys. **67**, 717 (2004).

[83] P. S. Pershan, "*Magneto-Optical Effects*," J. Appl. Phys. **38**, 1482 (1967).

[84] S. I. Maslovski, D. K. Morits, and S. A. Tretyakov, "*Symmetry and reciprocity constraints on diffraction by gratings of quasi-planar particles*," J. Opt. A **11**, 074004 (2009).

[85] K. Konishi, T. Sugimoto, B. Bai, Y. Svirko, and M. Kuwata-Gonokami, "*Effect of surface plasmon resonance on the optical activity of chiral metal nanogratings*," Opt. Express **15**, 9575 (2007).

[86] A. Potts, W. Zhang, and D. M. Bagnall, "*Nonreciprocal diffraction through dielectric gratings with two-dimensional chirality*," Phys. Rev. A **77**, 043816-1 (2008).

[87] E. Plum, V. A. Fedotov, and N. I. Zheludev, "*Planar metamaterial with transmission and reflection that depend on the direction of incidence*," Appl. Phys. Lett. **94**, 131901 (2009).

[88] R. M. Ho, C. K. Chen, and Y. W. Chiang, "*Novel Nanostructures from Self-Assembly of Chiral Block Copolymers*," Macromol. Rapid Comm. **30**, 1439 (2009).

[89] V. I. Kopp, V. M. Churikov, J. Singer, N. Chao, D. Neugroschl, and A. Z. Genack, "*Chiral fiber gratings*," Science **305**, 74 (2004).

[90] K. Robbie, M. J. Brett, and A. Lakhtakia, "*Chiral sculptured thin films*," Nature **384**, 616 (1996).

[91] M. J. Brett and M. M. Hawkeye, "*Materials science - New materials at a glance*," Science **319**, 1192 (2008).

[92] E. R. Dedman, D. N. Sharp, A. J. Turberfield, C. F. Blanford, and R. G. Denning, "*Photonic crystals with a chiral basis by holographic lithography*," Photonics Nanostruct. Fundam. Appl. **3**, 79 (2005).

[93] N. Liu, H. C. Guo, L. W. Fu, S. Kaiser, H. Schweizer, and H. Giessen, "*Three-dimensional photonic metamaterials at optical frequencies*," Nature Mater. **7**, 31 (2008).

[94] M. Decker, M. Ruther, C. Kriegler, J. Zhou, C. Soukoulis, L. S., and M. Wegener, "*Strong optical activity from twisted-cross photonic metamaterials*," Opt. Lett. **34**, 2501 (2009).

[95] S. Maruo, O. Nakamura, and S. Kawata, "*Three-dimensional microfabrication with two-photon-absorbed photopolymerization*," Opt. Lett. **22**, 132 (1997).

[96] J. P. Vanderzi, P. S. Pershan, and L. D. Malmstro, "*Optically-Induced Magnetization Resulting From Inverse Faraday Effect*," Phys. Rev. Lett. **15**, 190 (1965).

[97] M. O'Neill and S. M. Kelly, "*Liquid crystals for charge transport, luminescence, and photonics*," Adv. Mater. **15**, 1135 (2003).

[98] C. N. LaFratta, J. T. Fourkas, T. Baldacchini, and R. A. Farrer, "*Multiphoton fabrication*," Angew. Chem. Int. Ed. **46**, 6238 (2007).

[99] S. Maruo and J. T. Fourkas, "*Recent progress in multiphoton microfabrication*," Laser Photonics Rev. **2**, 100 (2008).

[100] M. Göppert-Mayer, "*Über Elementarakte mit zwei Quantensprüngen*," Ann. Phys. **401**, 273 (1931).

[101] W. Kaiser and C. G. B. Garrett, "*Two-Photon Excitation in* $CaF_2$*:*$Eu^{2+}$," Phys. Rev. Lett. **7**, 229 (1961).

[102] W. Denk, J. H. Strickler, and W. W. Webb, "*Two-photon laser scanning fluorescence microscopy*," Science **248**, 73 (1990).

[103] D. A. Parthenopoulous and P. M. Rentzepis, "*Three-Dimensional Optical Storage Memory*," Science **245**, 843 (1989).

[104] J. H. Strickler and W. W. Webb, "*Three-Dimensional Optical-Data Storage In Refractive Media By 2-Photon Point Excitation*," Opt. Lett. **16**, 1780 (1991).

[105] S. H. Wong, M. Thiel, P. Brodersen, D. Fenske, G. A. Ozin, M. Wegener, and G. von Freymann, "*Highly selective wet etch for high-resolution three-dimensional nanostructures in arsenic sulfide all-inorganic photoresist*," Chem. Mater. **19**, 4213 (2007).

[106] S. Wong, O. Kiowski, M. Kappes, J. K. N. Lindner, N. Mandal, F. C. Peiris, G. A. Ozin, M. Thiel, M. Braun, M. Wegener, and G. von Freymann, "*Spatially Localized Photoluminescence at 1.5 Micrometers Wavelength in Direct Laser Written Optical Nanostructures*," Adv. Mater. **20**, 4097 (2008).

[107] M. S. Rill, C. Plet, M. Thiel, I. Staude, G. von Freymann, S. Linden, and M. Wegener, "*Photonic metamaterials by direct laser writing and silver chemical vapour deposition*," Nature Mater. **7**, 543 (2008).

[108] C. E. Kriegler, M. S. Rill, M. Thiel, E. Muller, S. Essig, A. Frolich, G. von Freymann, S. Linden, D. Gerthsen, H. Hahn, K. Busch, and M. Wegener, "*Transition*

*between corrugated metal films and split-ring-resonator arrays*," Appl.Phys. B **96**, 749 (2009).

[109] M. S. Rill, C. E. Kriegler, M. Thiel, G. von Freymann, S. Linden, and M. Wegener, "*Negative-index bianisotropic photonic metamaterial fabricated by direct laser writing and silver shadow evaporation*," Opt. Lett. **34**, 19 (2009).

[110] M. Thiel, M. S. Rill, G. von Freymann, and M. Wegener, "*Three-dimensional bi-chiral photonic crystals*," Adv. Mater. **46**, 4680 (2009).

[111] M. Thiel, H. Fischer, G. von Freymann, and M. Wegener, "*Three-dimensional chiral photonic superlattices*," Opt. Lett., accepted (2009).

[112] G. von Freymann, A. Ledermann, M. Thiel, I. Staube, S. Essig, K. Busch, and M. Wegener, "*Three-Dimensional Nanostructures for Photonics*," Adv. Funct. Mater., accepted (2009).

[113] I. Staude, M. Thiel, S. Essig, C. Wolff, K. Busch, G. von Freymann, and M. Wegener, "*Fabrication and characterization of silicon woodpile photonic crystals with a complete band gap at telecom-wavelenghts*," in preparation (2009).

[114] M. Deubel, G. Von Freymann, M. Wegener, S. Pereira, K. Busch, and C. M. Soukoulis, "*Direct laser writing of three-dimensional photonic-crystal templates for telecommunications*," Nature Mater. **3**, 444 (2004).

[115] A. Ovsianikov, S. Schlie, A. Ngezahayo, A. Haverich, and B. N. Chichkov, "*Two-photon polymerization technique for microfabrication of CAD-designed 3D scaffolds from commercially available photosensitive materials*," Journal Of Tissue Engineering And Regenerative Medicine **1**, 443 (2007).

[116] T. Woggon, T. Kleiner, M. Punke, and L. U., "*Nanostructuring of organic-inorganic hybrid materials for distributed fedback laser resonators by two photon polymerization*," Opt. Express **17**, 2500 (2009).

[117] S. Wong, M. Deubel, F. Perez-Willard, S. John, G. A. Ozin, M. Wegener, and G. von Freymann, "*Direct laser writing of three-dimensional photonic crystals with complete a photonic bandgap in chalcogenide glasses*," Adv. Mater. **18**, 265 (2006).

[118] S. Wong, "*Arsenic Trisulfide Inorganic Photoresist for Three-Dimensional Photolithography*," Doctoral thesis (Universität Karlsruhe) (2008).

[119] D. M. Whittaker and I. S. Culshaw, "*Scattering-matrix treatment of patterned multilayer photonic structures*," Phys. Rev. B **60**, 2610 (1999).

[120] S. G. Tikhodeev, A. L. Yablonskii, E. A. Muljarov, N. A. Gippius, and T. Ishihara, "*Quasiguided modes and optical properties of photonic crystal slabs*," Phys. Rev. B **66**, 045102 (2002).

[121] J. B. Pendry and A. Mackinnon, "*Calculation Of Photon Dispersion-Relations*," Phys. Rev. Lett. **69**, 2772 (1992).

[122] D. Y. K. Ko and J. C. Inkson, "*Matrix-Method For Tunneling In Heterostructures - Resonant Tunneling In Multilayer Systems*," Phys. Rev. B **38**, 9945 (1988).

[123] L. Li, "*Formulation and comparison of two recursive matrix algorithms for modeling layered diffraction gratings*," J. Opt. Soc. Am. A **13**, 1024 (1996).

[124] M. Thiel, G. von Freymann, and M. Wegener, "*Layer-by-layer three-dimensional chiral photonic crystals*," Opt. Lett. **32**, 2547 (2007).

[125] M. Thiel, M. Wegener, and G. von Freymann, "*Three-dimensional chiral photonic crystals by direct laser writing*," Proc. SPIE **6883**, K8830 (2008).

[126] H. deVries, "*Rotatory Power And Other Optical Properties Of Certain Liquid Crystals*," Acta Crystallogr. **4**, 219 (1951).

[127] J. C. W. Lee and C. T. Chan, "*Circularly polarized thermal radiation from layer-by-layer photonic crystal structures*," Appl. Phys. Lett. **90**, 051912 (2007).

[128] M. Thiel, "*Herstellung dreidimensionaler chiraler Photonischer Kristalle und deren Charakterisierung*," Diplomarbeit (Universität Karlsruhe) (2006).

[129] L. Li and J. A. Dobrowolski, "*Visible broadband, wide-angle, thin-film multilayer polarizing beam splitter*," Appl. Opt. **35**, 2221 (1996).

[130] J. Y. Chen and L. W. Chen, "*Color separating with integrated photonic band-gap optical diodes: a numerical study*," Optics Express **14**, 10733 (2006).

[131] F. Mariotte, S. A. Tretyakov, and B. Sauviac, "*Isotropic Chiral Composite Modeling - Comparison Between Analytical, Numerical, And Experimental Results*," Microwave And Optical Technology Letters **7**, 861 (1994).

[132] V. I. Kopp and A. Z. Genack, "*Twist defect in chiral photonic structures*," Phys. Rev. Lett. **89**, 033901 (2002).

# Acknowledgments

In 2005, I visited the National Institute of Standards and Technology in Boulder as a student guest researcher and was invited to a dinner party in a professor's house. He was from Brazil and we talked about being a Ph.D. student in his country. He said, "A Ph.D. thesis in any country is like falling from a surfboard. Strong turbulences in the water will give you a hard time to reach the top, but, after three years, you can breath again."

Three years after the beginning of my doctoral thesis at the institution now called Karlsruhe Institute of Technology (KIT), I take the first breath and thank all the people who helped me on my "surf trip" and have also contributed to the success of this thesis.

First and foremost, I would like to thank my doctoral adviser Prof. Dr. Martin Wegener for giving me the opportunity to work on such a fascinating topic. The research conditions in his group are simply perfect; he provides hot topics, well-equipped laboratories, and a creative atmosphere. This thesis has largely benefited from his profound knowledge, continuous interest, and numerous physical discussions. Moreover, I am grateful that he gave me the chance to be the youngest co-founder of the KIT spin-off Nanoscribe GmbH.

I thank Prof. Dr. Kurt Busch for kindly agreeing to co-referee this thesis. It is a blessing for an experimental group to have an excellent theory group sitting in the same building. The joint publications have highly benefited from his and his group members' profound theoretical knowledge in the field of nanophotonics.

The next huge "thank you" goes to Dr. Georg von Freymann. I owe him a lot because he has not only been my supervisor but also a *very* important help to build up the DLW systems, to solve *any* technical problem within a one-minute phone call, to discuss experimental and theoretical results, and I really like his positive attitude to deal with obstacles. Hopefully, he soon gets appointed professor.

Furthermore, I would like to thank the following co-investigators:

- Dr. Stefan Linden highly contributed to physical discussions and programmed the original scattering-matrix code. I thank him for giving me the opportunity to use the code and for helping with the calculation of the field distributions.
- Michael Rill gave valuable advice for all kinds of issues during the entire time of my thesis. Moreover, he organized the commissioning of the commercial FTIR, which was used for some of the measurements.

- I am grateful to my former colleague Dr. Sean Wong. Together, we developed a new photoresist for DLW that is already in use for new projects of our group.
- It is a pleasure to thank Jacques Hawecker from the CFN service team for his supreme electron micrographs.
- I am indebted to the proof readers of this thesis for their supporting comments and many hints, which improved the readability.

Thanks to all the other members of the Wegener group for many helpful discussions, the team spirit, and the comfortable atmosphere. Importantly, I really enjoyed the fruitful collaborations on other scientific topics (e.g., metallic metamaterials (M. Rill, C. Kriegler, and J. K. Gansel) and photonic crystals with defects (I. Staude)).

My thanks also goes to the different facilities of the Institute of Applied Physics. Renate Helfen, Monika Brenkmann, and Christa Weisenburger, our (former) secretaries, have helped me with all bureaucratic tasks and problems. The members of the electronic workshop, Heinz Hoffmann, Helmut Lay, and Werner Gilde are taking care of all computers and electronic problems. Thanks to them and also to the mechanical workshop around our technician Johann Westhauser and Thorsten Kuhn. We all miss Thorsten very much.

Furthermore, I would like to thank the DFG-Center for Functional Nanostructures (CFN), the Karlsruhe School of Optics & Photonics (KSOP), and the team at Nanoscribe (Martin Hermatschweiler, Steffen Holtwick, and Holger Fischer) for their support during my thesis.

My last words are devoted in gratitude toward my parents and friends: Love you guys.